Plasmonics: Numerical Methods and Device Applications

Thesis by

Luke A. Sweatlock

In Partial Fulfillment of the Requirements

for the Degree of

Doctor of Philosophy

California Institute of Technology

Pasadena, California

2008

(Defended May 23, 2008)

To my parents, John & Donna Noctor

Acknowledgements

It is my pleasure to acknowledge the many people who have supported me during my stay at Caltech.

First of all I would like to thank my advisor Harry Atwater, for providing the opportunity to study in an exciting field, and for being a constant source of research inspiration and of infectious enthusiasm. Thanks also to Albert Polman for making me feel welcome as a visitor, and for many years of insightful advice.

During my time in the Atwater group I was lucky to be surrounded by a great group of fellow students who always made the lab an enjoyable and enlightening environment. I owe a great debt of gratitude to all of my colleagues and collaborators. In particular, I want to thank my mentor Stefan Maier, and my regular co-authors Joan Penninkhof and Jennifer Dionne for their absolutely invaluable support.

I would also like to acknowledge the generous funding for this work, mainly provided by the Air Force Office of Scientific Research, and by the National Science Foundation via the Center for Science and Engineering of Materials at Caltech.

Finally, thanks to all my friends and family, and especially to Sarah, for making this journey possible.

Luke Sweatlock

May 2008

Pasadena, CA

Abstract

Plasmonics is a rapidly evolving subfield of nanophotonics that deals with the interaction of light with surface plasmons, which are the collective charge oscillations that occur at the interface between conductive and dielectric materials. Plasmonics meet a demand for optical interconnects which are small enough to coexist with nanoscale electronic circuits. Emerging technologies include very small, low-power active devices such as electrooptic or all-optical modulators. Passive plasmonic devices, or "optical antennas," are being used to enhance the performance of emitters and detectors, and to harvest sunlight for photovoltaics. This manuscript focuses on the process of developing novel plasmonic devices from concept to prototype, with specific emphasis on synthesizing data from numerical simulation and from empirical characterization into an accurate, predictive understanding of nanoscale optical phenomena.

The first part of the thesis outlines the development of numerical methods. In the case of resonant nanostructures such as small metal particles, the principal technique employed is impulse excitation ringdown spectroscopy. This method allows the critical advantage of generating broadband spectra from a single time-domain simulation. For analysis of plasmonic waveguides, Fourier-space analysis is used to reveal the dispersion properties of supported modes, and to perform filtering in the wavevector domain or "k-space". The remainder of the thesis deals with the design and characterization of plasmonic devices, with the broad and general goal of creating a significant impact in the fields of optoelectronics and photovoltaics.

Contents

List of Figures

List of Tables

List of Publications

Portions of this thesis have been drawn from the following sources:

Articles

"Optical cavity modes in gold shell colloids," J. J. Penninkhof, L. A. Sweatlock, H. A. Atwater, A. Moroz, A. van Blaaderen, and A. Polman. *Journal of Applied Physics*, (In press).

"Plasmonic Modes of Annular Nanoresonators Imaged by Spectrally-resolved Cathodoluminescence," C. E. Hofmann, E. J. Vesseur, L. A. Sweatlock, H. J. Lezec, F. J. Garcia de Abajo, A. Polman, and H. A. Atwater. *Nano Letters*, **7** 3612 (2007).

"Plasmon-enhanced photoluminescence of Si quantum dots: Simulation and experiment," J. S. Biteen, L. A. Sweatlock, H. Mertens, N. S. Lewis, H. A. Atwater, and A. Polman. *Journal of Physical Chemistry C*, **111** 13372-13377 (2007).

"Plasmon slot waveguides: Towards chip-scale propagation with subwavelength-scale localization," J. A. Dionne, and L. A. Sweatlock, H. A. Atwater, and A. Polman. *Physical Review B*, **73** 035407 (2006).

"Planar metal plasmon waveguides: frequency-dependent dispersion, propagation, localization, and loss beyond the free electron model," J. A. Dionne, and L. A. Sweatlock, H. A. Atwater, and A. Polman. *Physical Review B*, **72** 075405 (2005).

"Highly confined electromagnetic fields in arrays of strongly coupled Ag nanoparticles," L. A. Sweatlock, S. A. Maier, H. A. Atwater, J. J. Penninkhof, and A. Polman. *Physical Review B*, **71** 235408 (2005).

"Mega-electron-volt ion beam induced anisotropic plasmon resonance of silver nanocrystals in glass," J. J. Penninkhof, A. Polman, L. A. Sweatlock, S. A. Maier. *Applied Physics Letters*, **83** 4137-4139 (2003).

Proceedings, Books Chapters, and Manuscripts

"All-optical Plasmonic Modulators and Interconnects," D. Pacifici, H. J. Lezec, L. A. Sweatlock, C. de Ruiter, V. E. Ferry, and H. A. Atwater. In S. I. Bozhevolnyi, editor, *Plasmonic Nanoguides and Circuits* (In press).

"Universal optical transmission features in periodic and quasiperiodic hole arrays," D. Pacifici, H. J. Lezec, L. A. Sweatlock, R. J. Walters, and H. A. Atwater. (Submitted).

"PlasMOStor: a metal-oxide-silicon field effect plasmonic modulator," J. A. Dionne, K. A. Diest, L. A. Sweatlock, and H. A. Atwater. (Submitted).

"Subwavelength-scale Plasmon Waveguides," H. A. Atwater, J. A. Dionne, and L. A. Sweatlock. In M. L. Brongersma and P. G. Kik, editors, *Surface Plasmon Photonics*, pages 87–104. Dordrecht, NL: Springer.

"The new '*p-n* Junction': Plasmonics Enables Photonic Access to the Nanoworld," H. A. Atwater, S. Maier, A. Polman, J. A. Dionne, and L. A. Sweatlock. *Materials Research Society Bulletin*, **30**, 385 (2005).

"Microwave Analogue to a Subwavelength Plasmon Switch," L. A. Sweatlock, S. A. Maier, and H. A. Atwater. *Proceedings of Electronic Components & Technology Conference* (2003).

Chapter 1

Introduction

1.1 Motivation

Plasmonics is a rapidly evolving subfield of nanophotonics that deals with the interaction of light with surface plasmons, which are the collective charge oscillations that occur at the interface between conductive and dielectric materials. Resonators made from metal nanostructures can confine concentrated optical energy to tiny regions of space, much smaller than a wavelength of light in free space. Likewise many exotic effects can be achieved with metallic waveguides, such as guiding light at optical frequencies with a tiny, X-ray-like wavelength; or even with a negative effective optical index. The possible applications of plasmonics abound in any field which would benefit from enhanced control of photons; from beamsteering to single-molecule biodetection. Even such extraordinary technologies as micro-targeted infrared cancer therapy and "invisibility cloaks" are on the horizon.

Our work has focused on the development of applications for optoelectronics. In this area, plasmonics meet a demand for optical interconnects which are small enough to coexist with nanoscale electronic circuits. Emerging technologies include very small, low-power active devices such as electrooptic or all-optical modulators. Passive plasmonic devices, or "optical antennas," are being used to enhance the performance of emitters and detectors, and to harvest sunlight for photovoltaics. This thesis will focus on the process of developing novel plasmonic devices from concept to prototype, with specific emphasis on synthesizing data from numerical simulation and from empirical characterization into an accurate, predictive understanding of nanoscale optical phenomena.

The strong interaction between microscopic metal particles and light has been exploited for thousands of years, most recognizably in the art of creating brightly colored stained-glass window panels by annealing metallic salts in otherwise transparent glass. Many dozens of practical recipes for this ancient "nanofabrication" technique survive from as early as the 8th century A.D. (*The Book of the Hidden Pearl*, Jabir ibn Hayyan). Roman artisans also produced remarkable dichroic glass artworks, although only one piece survives intact, the "Lycurgus Cup" dated 4th century A.D. Viewed normally by reflected light the surface is opaque olive green, but when backlit the cup is a brilliant translucent red. This unusual effect is thematic to the depicted scene, which captures Lycurgus at the moment he is dragged below to the underworld by a vine. The microscopic origin of the optical dichroism is, in fact, the inclusion of gold and silver particles which are about 60 nm in diameter, and which strongly scatter green light but transmit red.

Quantitative studies of the unusual optical properties of metals emerge around the beginning of the 20th century. Near the turn of the century Lord Rayleigh explains the blue color of the sky in terms of a simple derivation of the scattering power of spheres small compared to the wavelength [116]. In 1904, J.C.M. Garnett first describes the bright colors of metal glass [83] employing the contemporary Drude model for the optical properties of free-electron metals [35]. Shortly thereafter, in 1908, Gustav Mie [89] presents a general formulation for the scattering of light from spherical surfaces, including the particular case of gold colloidal nanoparticles of varying size. The impact of this formative article on many disciplines, including atmospheric science, astrophysics, plasmonics, and even computer graphics, is difficult to overstate. As of April 2008, the manuscript's 100th anniversary, the work has been cited $3,771$ times as recorded by the SCI database. (The same database records $3,386$ citations, combined, for all four of Einstein's 1905 "*Annus Mirabilis*" papers, which also appeared in *Annalen der Physik*.)

Surface plasmons in thin films are first described in terms of electron energy loss spectroscopy in 1957, by Ritchie [117]. A major experimental milestone occured in 1968 when Otto [97], and Kretschmann and Raether [66] report methods for exciting surface plasmons on metal films optically. In 1974, the enhancement of Raman scattering from molecules influenced by the enhanced local fields at a rough metal surface was first observed by Fleischmann et al. [38]. Since that time, surface enhanced Raman spectroscopy (SERS) has become a well-established discipline. Commercial surface plasmon resonance biosensors arrived on the

market in the early 1990s, and single molecule Raman sensing on a rough silver surface was reported in 1997 [93].

Most recently, increased sophistication of electromagnetic simulation techniques and in computational power, and refinement of nanofabrication tools such as electron beam lithography and focused ion beam milling, have lead to a redoubling of interest in engineered metallic nanostructures. These developments, together with the increasing demand for information bandwidth which drives interest in chip-scale integration of optical components, have enabled the birth of *plasmonics* as a nanophotonic discipline [6, 19, 77, 99].

1.2 Optical Constants

The response of a material to incident light is expressed as the *complex refractive index* $N = n + \mathrm{i}k$, or as the *complex dielectric function*[1] $\varepsilon = \varepsilon' + i\varepsilon''$. Although these parameters are generally referred to as optical "constants," they are not fixed values; indeed, the various useful, beautiful, and sundry phenomena of light-matter interaction arise from their functional dependence on frequency (wavelength).

While (n,k) are most directly related to physical observation of the velocity and attenuation of waves, $(\varepsilon',\varepsilon'')$ are a more convenient form for connecting to Maxwell's equations. The two expressions are totally equivalent and are related to each other, and to the permittivity ϵ, by [14, 57]

$$\varepsilon' = \frac{\epsilon'}{\epsilon_0} = n^2 - k^2, \tag{1.1}$$

$$\varepsilon'' = \frac{\epsilon''}{\epsilon_0} = 2nk, \tag{1.2}$$

$$n = \sqrt{\frac{\sqrt{\varepsilon'^2 + \varepsilon''^2} + \varepsilon'}{2}}, \tag{1.3}$$

$$k = \sqrt{\frac{\sqrt{\varepsilon'^2 + \varepsilon''^2} - \varepsilon'}{2}}, \tag{1.4}$$

with ε_0 the permittivity of free space, and assuming that the material is not magnetic so that the permissivity $\mu = \mu_0$. For linear materials, the optical constants are related to phenomenological material *susceptibility* χ

[1] Alternative definitions include the opposite exponential sign convention $N = n - \mathrm{i}k$ and $\varepsilon = \varepsilon' - i\varepsilon''$, or the normalized imaginary part $N = n(1 \pm \mathrm{i}\kappa)$

by

$$\varepsilon = 1 + \chi, \tag{1.5}$$

and to Maxwell's equations by the constitutive relation for the material *polarization* $\mathbf{P}$

$$\mathbf{P} = \varepsilon_0 \chi \mathbf{E}. \tag{1.6}$$

The dielectric constant can be determined by observing the optical power reflected and transmitted from a sample, or perhaps most commonly, by measuring the change in a beam's polarization state upon reflection, i.e., by spectroscopic reflection ellipsometry.

The optical properties of many materials are approximately independent of frequency, at least over a given region of interest in the spectrum. For example, for a transparent dielectric such as glass, $\varepsilon_{SiO_2} \approx 2.5$ throughout the visible. Other "weakly dispersive" materials can be often be treated with an effectively constant dielectric but only over a narrow spectral range. Therefore we might say that, for the transparent conductor Indium Tin Oxide (ITO), $\varepsilon_{ITO} \approx 3.4$ @ $\lambda = 590$ nm. Values of ε for some transparent dielectrics appearing in this thesis are included in Table B.1. The distinction between "non-dispersive" and "weakly dispersive" materials is somewhat arbitrary and depends entirely on the frequency bandwidth of the user's analysis; only vacuum is a truly non-dispersive material.

By contrast, the dielectric properties of metals vary strongly as a function of optical frequency, which we will model explicitly. Of special interest for analysis is the process of converting measurements of $\varepsilon(\omega)$, which may come from ellipsometry or from a materials handbook, into a concise parametric model. There are a number of advantages if one performs this parameterization using a physically motivated (e.g., Lorentz-Drude multioscillator) rather than an arbitrary (e.g., polynomial fit) model [132]:

- Physical models correctly predict the qualitative shape of $\varepsilon(\omega)$, and therefore produce fits with a relatively high degree of accuracy with a small number of free parameters.
- Physical models inherently obey the Kramers-Kronig relations which constrain the relationship between ε' and ε''. An arbitrary fit which treats the real and imaginary parts of ε independently will lead

to violation of linearity and causality. Producing correctly causal, arbitrary fits may be computationally intensive.

- When working in the time domain, the time-domain susceptability $\chi(t)$ is obtained by Fourier transform of the frequency-domain quantity $\chi(\omega)$. Physical oscillator models produce analytic transforms.

1.2.1 Physical origin of the Lorentz model

The optical properties of matter can be understood in terms of classical physical models of the microscopic structure[2]. In plasmonics, the most important of these classical models proves to be the Lorentz-Drude (LD) multioscillator model, in which the charge carriers in a material are treated as damped harmonic oscillators, subject to driving forces in the form of applied electromagnetic fields. In the Lorentz model, a charge carrier is characterized by its mass m, charge e, and displacement from equillibrium x. Assuming that the forces on this particle can be expressed as a linear spring force $F = Kx$, a velocity dependent damping $F = b\dot{x}$, and a driving force supplied by the local electric field of any incident light $F = e\mathbf{E}$, the equation of motion is

$$m\ddot{x} + b\dot{x} + Kx = e\mathbf{E}, \tag{1.7}$$

or normalizing by mass and introducing $\omega_0^2 = K/m$ and $\Gamma = b/m$,

$$\ddot{x} + \gamma\dot{x} + \omega_0^2 x = (e/m)\mathbf{E}. \tag{1.8}$$

A time-harmonic solution to Equation 1.8 can be found by substitution ($\dot{x} \leftrightarrow -i\omega x$ and $\ddot{x} \leftrightarrow -\omega^2 x$):

$$x = \frac{(e/m)\mathbf{E}}{\omega_0^2 - \omega^2 - i\Gamma\omega}. \tag{1.9}$$

Given the above response for a single oscillator, the optical properties of a material consisting of an ensemble of oscillators is constructed as follows: The dipole moment of each oscillator is by definition $p = ex$ and the polarization $\mathbf{P}$ of an ensemble of N oscillators per unit volume V, is $\mathbf{P} = (N/V)p$. Then

[2]The optical properties of materials are discussed in many excellent books and articles. Material in this section follows the texts cited above: *Absorption and Scattering of Light by Small Particles* by Bohren and Huffman [14], *Classical Electrodynamics* by Jackson, and *Computational Electrodynamics* by Taflove and Hagness.

Equation 1.9 can be expressed as

$$\mathbf{P} = \frac{\omega_p^2}{\omega_0^2 - \omega^2 - \mathrm{i}\Gamma\omega}\varepsilon_0\mathbf{E}, \tag{1.10}$$

where the *plasma frequency* ω_p is introduced and defined as

$$\omega_p^2 = \frac{(N/V)e^2}{m\varepsilon_0}. \tag{1.11}$$

As an aside, please note that the value of ω_p when used as an empirical fitting parameter to ellipsometric data co-varies with several other fit parameters (γ, ω_0), and does not necessarily provide an accurate metric for the actual plasma frequency, carrier density, or carrier effective mass of a given material.

Finally, the dielectric function is determined by comparison of Equation 1.10 with 1.5 and 1.6,

$$\varepsilon_{\text{Lorentz}}(\omega) = 1 + \frac{\omega_p^2}{\omega_0^2 - \omega^2 - \mathrm{i}\Gamma\omega}. \tag{1.12}$$

1.2.2 Multi-oscillator Lorentz-Drude model

The single-oscillator model, described above, can be made more general by superposition of $j+1$ individual oscillators,

$$\varepsilon_{\text{Lorentz-Drude}}(\omega) = 1 - \frac{f_0\omega_{p,0}^2}{\omega^2 + \mathrm{i}\Gamma_0\omega} + \sum_{j=1}^{j_{\max}} \frac{f_j\omega_{p,j}^2}{\omega_j^2 - \omega^2 - \mathrm{i}\Gamma_j\omega}. \tag{1.13}$$

Each Lorentz term (inside the sum) has 4 free parameters: oscillator strength f_j, plasma frequency $\omega_{p,j}$, damping rate Γ_j, and oscillator frequency ω_j. The zeroth order or "Drude" term outside the sum is essentially similar, but with oscillator frequency identically equal to zero. This term represents the contribution of free electrons which feel no restoring "spring" force when displaced. Using j not more than five, it is possible to construct an excellent fit to measured optical properties for arbitrary metals and many semiconductors throughout the visible spectrum.

In general, the $4(j+1)-1$ free parameters in the above multioscillator model can be determined from a number of nonlinear curve fitting algorithms. Most commonly, we use the fits to the data of Palik's *Handbook*

of Optical Constants [75] which have been performed by Rakic et al. [115] by a simulated annealing algorithm. These handbook parametric data for Au, Ag, Al, Cu, and Cr, converted into our notation, are tabulated in the Appendix B.3. When working with ellipsometric rather than handbook data, we use a simple iterative least-squares minimization algorithm to determine the unknown coefficients.

1.2.3 Extended Drude model

The optical properties of some metals are dominated by the contribution of free electrons. Aluminum, and the alkali metals including sodium (Na) and potassium (K), can be modeled quite well by using only the Drude or zeroth-order term of the LD multioscillator model,

$$\varepsilon_{\text{Drude}}(\omega) = 1 - \frac{\omega_p^2}{\omega^2 + i\Gamma\omega}. \tag{1.14}$$

The important plasmonic metals Ag and Au, however, exhibit a small but non-negligible contribution from bound electrons in addition to fundamentally free-electron-like behavior. The applicability of the Drude model can be extended by adding two additional fitting parameters, $\varepsilon_{\text{static}}$ and $\varepsilon_{\text{high}}$:

$$\varepsilon_{\text{ExtendedDrude}}(\omega) = \varepsilon_{\text{high}} - \frac{(\varepsilon_{\text{static}} - \varepsilon_{\text{high}})\omega_p^2}{\omega^2 + i\Gamma\omega}. \tag{1.15}$$

Using the extended Drude model we can achieve excellent parameterizations of Ag throughout the visible and infrared. It is also useful for Au, but any given set of parameters is valid over a smaller bandwidth, and agreement falls off entirely at high frequency (poor fit for wavelengths $\lambda_0 < 500$ nm). Several sets of Drude parameters for Ag and Au, valid for various frequency bands, are tabulated in the Appendix, B.2.

1.2.4 Debye model

The multioscillator model can be applied to linear media with almost complete generality by the inclusion of Debye oscillator terms, which we mention for completeness. Classically the Debye model is motivated by bound dipoles whose relaxation is smooth like an overdamped spring, rather than oscillatory. From a materials standpoint these terms describe polar media, such as water, or the behavior of solids for frequencies lower

than that of lattice vibrations. The dielectric function of a collection of Debye resonators can be expressed

$$\varepsilon_{\text{Debye}}(\omega) = \varepsilon_{\text{vib}} + \frac{\delta}{1 - i\tau\omega}, \tag{1.16}$$

with three fitting parameters: the intermediate frequency dielectric function ε_{vib}, the "DC offset" δ, and the relaxation time τ. The Debye terms are generally not explicitly considered in our models of plasmonic materials.

1.3 Resonant Plasmonic Properties of Metal Particles

The optical properties of metal particles are strikingly different from those of the bulk material. Contrast for example a brightly colored, translucent glass panel "stained" with Au or Ag nanoparticles, with the familiar metallic color of burnished mirror surfaces. In the language of modern electrodynamics, the interaction of light with a tiny metal particle is expressed as a boundary value problem, solving Maxwell's equations for a plane wave interacting with a spherical surface. This problem was first thoroughly addressed by Gustav Mie in an influential 1908 paper [89]. In the full treatment, the fields scattered from a sphere are expressed as an infinite series in the vector spherical harmonics. In this introductory section we will discuss the limiting case of very small particles, for which the lowest order spherical harmonic — the "dipole scattering" — is the dominant term.

1.3.1 Small metal particles in the quasistatic approximation

For metal particles with radius $a << \lambda$ much smaller than the incident wavelength, any applied fields can be considered uniform across the particle. Physically, the free conduction electrons inside the particle will all move in phase in response to the uniform illumination. At any given time, the problem is isomorphic to a particle in a uniform static field, and the electromagnetic response can therefore be determined using the quasistatic polarizability (i.e., the form of the polarizability α is determined by electrostatic theory, but the high-frequency material permittivities $\varepsilon(\omega)$ are used as parameters). The characteristic color and brightness of a given particle, and its experimentally observable transmission spectrum, are often expressed as the "cross

sections" for extinction, absorption, and scattering ($C_{\text{ext}}, C_{\text{abs}}, C_{\text{sca}}$, respectively). In the dipole approximation these are very simply related to the quasistatic polarizability α by the optical theorem of wave scattering [14],

$$C_{\text{ext}} \approx C_{\text{abs}} = k\Im(\alpha) \tag{1.17}$$

$$C_{\text{sca}} = \frac{k^4}{6\pi}|\alpha|^2 \tag{1.18}$$

with $k = 2\pi/\lambda$ the wavevector of the incident light. For a spherical particle of radius $a << \lambda$ surrounded by a medium of dielectric constant ε_m, the quasistatic polarizability α is

$$\alpha = 4\pi a^3 \frac{\varepsilon - \varepsilon_m}{\varepsilon + 2\varepsilon_m} \tag{1.19}$$

where the complex dielectric response of the metal particle is $\varepsilon = \varepsilon(\omega)$. Typically the embedding dielectric is considered to be a transparent nonabsorbing medium, and therefore ε_m is constant and a purely real number. The polarizability, and therefore the absorption and scattering cross sections, exhibit a resonance peak (i.e., a maximum value when considered as a function of frequency) at the condition $\Re(\varepsilon) \approx -2\varepsilon_m$, which minimizes the denominator of Equation 1.19. The frequency which satisfies this condition is sometimes called the Fröhlich frequency, or simply the particle dipole plasmon frequency. The spectral width of the resonance is limited by the nonzero imaginary part of $\varepsilon(\omega)$; physically the linewidth represents dephasing caused by Ohmic loss which damp the electrons' oscillation.

The plasmon resonance is also highly sensitive to the nanoparticles' shape [14, 63]. For an ellipsoidal particle with semiaxes a, b, c, the corresponding quasistatic polarizability can be expressed by including three geometric factors L_1, L_2, L_3,

$$\alpha_i = \frac{4\pi}{3} abc \frac{\varepsilon - \varepsilon_m}{\varepsilon_m + L_i(\varepsilon - \varepsilon_m)}, \qquad \sum_{i=1}^{3} L_i = 1. \tag{1.20}$$

The ellipsoidal polarizability reduces to the spherical case (for $a = b = c$; $L_i = \frac{1}{3}$), but in general, each

axis has a different geometrical factor[3] where $0 < L_i < 1$, so the optical response is anisotropic and strongly shape dependant. For spheroidal particles, ($L_1 = L_2 \neq L_3$), the extinction peak splits for two polarizations, that is, the particle is a different "color" depending on whether it is illuminated along the long or short axis of the particle. The extinction peak is strongly redshifted (i.e., the peak moves to significantly lower frequency) for light polarized longitudinally along the long axis of the particle, and blueshifted a small amount for the transverse polarization. A spectrum taken with random or circularly polarized light will show both modes superimposed. This splitting of resonance peaks is a general feature of reduced-symmetry plasmonic structures.

1.3.2 Introduction to non-quasistatic particles

Although the quasistatic approximation is valuable for generating an intuitive picture of particle plasmon resonances, most nanostructures of practical interest are not deep-subwavelength ellipsoids. In general, numerical methods such as the scattering T-matrix method, the discrete-dipole approximation (DDA), or as in this thesis, finite-integration or finite difference time-domain simulation (FITD, FDTD) are used to evaluate the scattering properties of more complex shapes. Before moving on, we will make a few general comments about specific interesting geometries.

The optical properties of a metal particle depend on its size. As the particle grows larger, the relative contribution of scattering to the total extinction, which is negligible for the tiniest particles, begins to grow. For particles which are finite size but still small, with radius $a > \lambda/10$ or so, the dipolar plasmon resonance peak redshifts and broadens. Particles which are a substantial fraction of the incident wavelength in size are no longer homogeneously polarized by incident light and so the quasistatic approximation breaks down entirely. Higher-order modes appear and become increasingly dominant. As the particle size continues to increase, the multitude of peaks broaden and eventually become indistinguishable, approaching the bulk spectral response.

Another interesting class of particles are core-shells, composed of a dielectric core and a metallic shell. In the case of relatively thick shells, plasmonic resonances can be excited, approximately independently, on either the outer or inner metallodielectric surface of the shell. For thin shells, the two modes interact strongly

[3] Defined as $L_1 = \frac{abc}{2}\int_0^\infty \frac{dq}{(a^2+q)f(q)}$ with $f(q) = [(q+a^2)(q+b^2)(q+c^2)]^{1/2}$, and with L_1, L_2, L_3 by cyclic permutation of a, b, c

with one another, and form two new coupled-plasmon modes, including a low-energy mode with symmetric surface charge polarization of each surface, and a high-energy mode with surfaces antisymmetrically polarized. [109]. Core-shell particles are an exciting technology in part because their spectral response can be tuned over a very large range by varying the shell thickness, as the peak splitting is very sensitive to the plasmon coupling between the two surfaces.

Finally, we are interested in 1D and 2D arrays of regularly spaced nanoparticles, close enough to one another to interact via electromagnetic field coupling. Consider for example, one-dimensional "chains" of small, closely spaced particles. When incident light is polarized with field transverse to the array, induced surface charges of like polarity on neighboring particles repel, increasing the energy required to drive a collective, resonant, oscillation. This effect translates spectrally to a blueshift of the transverse polarization extinction peak. Conversely , when excited by light longitudinal to the long axis of the array, induced dissimilar surface charges attract, which lowers the resonant energy, and results in a spectral redshift. Numerical studies [112] have shown that the polarization dependent peak splitting depends on the ratio of nearest-neighbor distance to particle radius, with large spectral shifts observed for very closely spaced particles. Particle arrays are promising for technical applications because of large resonant enhancement of the electromagnetic fields, which can be concentrated in the dielectric gaps between neighboring particles.

1.4 Surface Plasmons on Metallic Films

Propagating surface plasmons are the quanta of collective plasma oscillations localized at the interface between a metal and a dielectric.[4] Provided the thickness of the metal film exceeds the plasmon skin depth, oscillations at each metal-dielectric interface are decoupled, and independent surface plasmon modes at each metal-dielectric interface are sustained. A cross section of the geometry is shown as an inset in Figure 1.1; the metal is contained in the half space $z > 0$ with the metallodielectric interface located at $z = 0$. Wave propagation is along the x direction. Assuming a perpendicularly polarized electric field incident on the structure, the surface plasmon electric field takes the form

[4]This introduction to surface plasmons on thick metallic films has been adapted from Dionne, Sweatlock et al. PRB 2005 [31]. In that manuscript we also study propagating coupled plasmons on the two surfaces of a thin metal film.

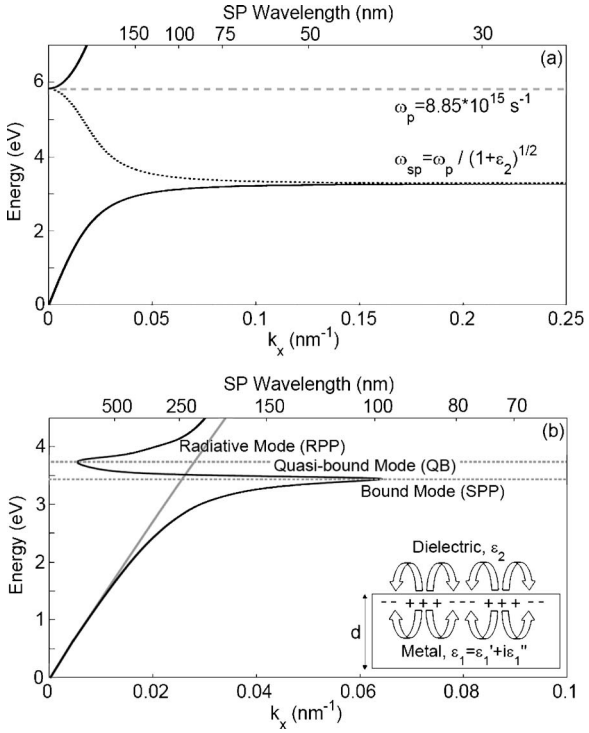

Figure 1.1: **(a)** Surface plasmon dispersion relation for the Ag/SiO_2 geometry computed using a free electron gas dispersion model. Note the existence of allowed modes (solid) for frequences below ω_{SP} and above ω_p, in contrast to the forbidden (i.e., purely imaginary) modes between these frequencies (dotted). **(b)** Bound (SPP), radiative (RPP), and quasibound (QB) surface plasmon dispersion relation for the $AgSiO_2$ geometry using the optical constants of Johnson and Christy. Unlike the free electron dispersion of panel (a), modes are allowed throughout the entire frequency range shown. The SiO_2 light line (gray) is also included for reference.

$$E(x,z,t) \sim E_0 e^{\mathrm{i}(k_x x - k_z|z| - \omega t)},$$

with components given by

$$\begin{aligned}
E_x^{\text{metal}} &= E_0 e^{\mathrm{i}(k_x x - k_{z1}|z| - \omega t)}, \\
E_x^{\text{dielectric}} &= E_0 e^{\mathrm{i}(k_x x - k_{z2}|z| - \omega t)}, \\
E_y^{\text{metal}} &= E_y^{\text{dielectric}} = 0, \\
E_z^{\text{metal}} &= E_0 \left(\frac{-k_x}{k_{z1}}\right) e^{\mathrm{i}(k_x x - k_{z1}|z| - \omega t)}, \\
E_z^{\text{dielectric}} &= E_0 \left(\frac{-\varepsilon_1 k_x}{\varepsilon_2 k_{z1}}\right) e^{\mathrm{i}(k_x x - k_{z2}|z| - \omega t)}.
\end{aligned}$$

The metal region is represented by $\varepsilon_1 = \varepsilon_1' + i\varepsilon_1''$ and corresponding k_{z1}, while the dielectric has ε_2 and k_{z2}. Demanding continuity of the tangential **E** and normal **D** fields at the interface yields the typical surface plasmon dispersion relations defined by [114]

$$k_x = \frac{\omega}{c}\sqrt{\frac{\varepsilon_1 \varepsilon_2}{\varepsilon_1 + \varepsilon_2}} \quad \text{and} \quad k_{z1,2}^2 = \varepsilon_{1,2}\left(\frac{\omega}{c}\right)^2 - k_x^2. \tag{1.21}$$

Provided $\varepsilon_1'' < |\varepsilon_1'|$ — a condition satisfied in Ag for $\lambda \geq 328$ nm using the optical constants of Johnson and Christy — the in-plane wave vector can be written as $k_x = k_x' + \mathrm{i}k_x''$, with

$$k_x' = \left(\frac{\omega}{c}\right)\sqrt{\frac{\varepsilon_1' \varepsilon_2}{\varepsilon_1' + \varepsilon_2}} \quad \text{and} \quad k_x'' = \left(\frac{\omega}{c}\right)\left(\frac{\varepsilon_1' \varepsilon_2}{\varepsilon_1' + \varepsilon_2}\right)^{3/2}\left(\frac{\varepsilon_1''}{2\varepsilon_1}\right). \tag{1.22}$$

Figure 1.1(a) illustrates the dispersion characteristics for this mode, plotted using the dielectric function of a free electron gas (FEG) with $\omega_p = 8.85 \times 10^{15} s^{-1}$. For energies below 3.3 eV, the typical bound surface plasmon-polariton (SPP) mode is observed, asymptoting at short wave vectors to the light line and at large wave vectors to the surface plasmon resonant frequency ω_{SP} (defined by the wavelength where $\varepsilon_1' = -\varepsilon_2$). Above 5.8 eV, the onset of the radiative plasmon-polariton (RPP) mode can be seen. For energies between

the SPP and RPP modes, the plasmon wave vector is purely imaginary (represented as a dotted line in the figure), indicating that modes in this regime are forbidden. Historically, this region between ω_{SP} and ω_p is referred to as the plasmon bandgap.

In contrast to the free electron behavior, dispersion arising from use of Johnson and Christy optical constants is plotted in Figure 1.1(b). For reference, the dispersion curve for the SiO_2 light line ($k_x = \varepsilon_2^{1/2}\omega/c$) is also included. Below 3.5 eV the SPP mode is observed, approaching the light line at short wave vectors but terminating at a *finite* wave vector on resonance ($k_x = 0.065$ nm^{-1} at ω_{SP}). As seen, the fairly large SPP wave vectors (and hence small SPP wavelengths) achieved near resonance compete with the largely reduced group velocity in this frequency range. Above 3.8 eV the RPP is observed, corresponding to wavelengths satisfying the relation $\varepsilon_1'' > |\varepsilon_1'|$ (i.e., $\lambda < 328$ nm). For energies between the SPP and RPP modes, k_x is determined by Equation 1.21 and what we term 'quasibound' (QB) modes appear to exist. Unlike the imaginary modes of the FEG dispersion, the modes plotted here have mathematically real components and hence are not *a priori* forbidden.

Quasibound modes provide an opportunity to study negative phase velocities in naturally occurring materials [72]. Nevertheless, the seemingly infinite group velocity marking the transition regimes between SPP/QB modes and QB/RPP modes is — at first sight — a disconcerting feature. In normal dispersive media, the group velocity is defined by the relation $v_g = d\omega/dk$. However, in regions of anomalous dispersion this linearization does not apply, and the propagation velocity of the wave packet must be modified to account for amplitude damping and wave profile deformation [134].

Figure 1.2 illustrates the propagation distance for an Ag/SiO_2 interface plasmon as a function of wavelength for both the Johnson and Christy and Palik dielectric data sets. The surface plasmon intensity decreases as $\exp(2\Re[ik_x x])$ so that the propagation length is given by $L = |2\Re[ik_x]|^{-1}$. As seen, at the important telecommunications wavelength of 1550 nm, propagation distance approaches ~ 400 μm using the Johnson and Christy dielectric function data set and ~ 70 μm using Palik; at shorter wavelengths, both curves converge toward nanometer-scale propagation at the surface plasmon resonance. Thus, although large surface plasmon wave vectors (and therefore short plasmon wavelengths) can be achieved near resonance, these attributes are often at the expense of propagation length.

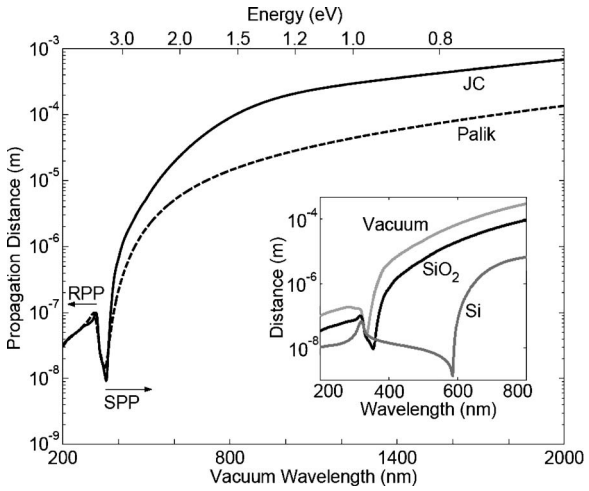

Figure 1.2: Surface plasmon propagation length for the Ag/SiO_2 geometry calculated using the optical constants of Johnson and Christy (solid) and Palik (dotted). A vanishing propagation length occurs at the surface plasmon resonance, around $\lambda = 355$ nm. The local maximum at $\lambda \sim 320$nm coincides with the transition between QB and RPP modes. Inset: Comparison of SP propagation for Ag/Air, Ag/SiO_2, and Ag/Si geometries plotted about the SP resonance.

Still, Figure 1.2 does reveal the presence of a local maximum in propagation existing close to the plasmon resonant frequency. Indicating the transition between the QB and RPP modes, the neighborhood about this maximum corresponds to the region of anomalous dispersion in the silver dielectric constant. Accordingly, the relative magnitude of this maximum can be controlled by altering the refractive index of the surrounding dielectric.

To illustrate the effects of varying the dielectric optical constant, the inset of Figure 1.2 plots propagation lengths for Ag/Air, Ag/SiO_2, and Ag/Si interface plasmons over the spectral range of 200 to 800 nm. By using materials of varying refractive indices, the surface plasmon resonant frequency can be tuned through a broad spectral range. As a result, the energetic location of the maxima and minima in the propagation distance plot can be controlled. Alternatively, at a given frequency, the surface plasmon wavelength (and hence damping) can be tuned by the dielectric constant. Such results suggest that by altering the optical properties of the embedding dielectric, propagation might be dynamically switched under electrical bias or optical pumping.

Figure 1.3 plots the surface plasmon electric field skin depth ($1/e$ decay length) in both Ag and SiO_2 as a function of wavelength. Note that in this graph, decay into the metal is plotted below $z = 0$. For clarity, the figure only includes skin depth computed using the Johnson and Christy data set. As expected, the SPP skin

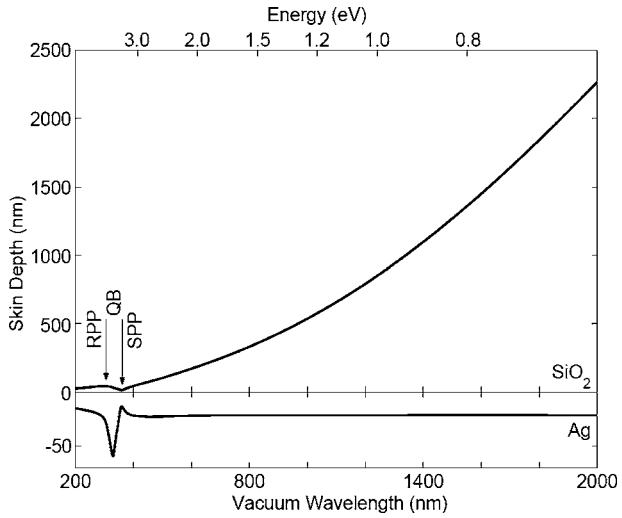

Figure 1.3: Surface plasmon electric field penetration depth in Ag and SiO_2, computed using the dielectric data of Johnson and Christy. The local penetration maximum at shorter wavelengths corresponds to the transition between the quasibound and radiative surface plasmon modes.

depth into the dielectric increases with increasing wavelength, reaching values of 1.3 μm (1.1 μm) in SiO_2 at $\lambda_{vac} = 1550$ nm for the Johnson–Christy (Palik) data sets, respectively. In contrast, the SPP skin depth into the metal remains roughly constant at ~ 25 nm for wavelengths beyond the plasmon resonance. At resonance, field penetration in the metal reaches a minimum in both the metal and dielectric (with $z \sim 15$ nm in both Ag and SiO_2). For even shorter wavelengths, field penetration reaches a maximum in the metal and a local maximum in SiO_2 ($z_{Ag} \sim 60$ nm, $z_{SiO_2} \sim 40$ nm) for $\lambda \sim 330$ nm — a wavelength regime corresponding to anomalous Ag dispersion and marking the onset of the radiative plasmon polariton.

This observation raises an interesting distinction between the system resonances corresponding to the extrema in the plot of propagation length versus wavelength (i.e., the local maximum and the global minimum in Fig. 1.2). At one system resonance, corresponding to anomalous dispersion, propagation is slightly enhanced despite high field confinement within the metal. However, at the surface plasmon resonance, propagation approaches single nanometer scales despite minimal energy density within the metal. The latter result is explained by the vanishing SPP excitation group velocity near the plasmon resonance. Still, the contradiction to the common localization versus loss heuristic is evident: field localization within the metal does not necessarily result in increased loss.

1.5 Scope of this Thesis

The work presented in this thesis falls into two broad categories. First is development of numerical methods for analysis of plasmonic nanostructures. Second is the design and characterization of plasmonic devices, with the broad and general goal of creating a significant impact in the fields of optoelectronics and photovoltaics. The two pursuits are, of course, intimately related. As the experimental state of the art has progressed from basic physical studies to the prototyping of various functional plasmonic devices, so too has the demand for numerical solutions evolved to include tools for quantitative prediction of practical figures of merit. The thesis is divided into three main parts:

1.5.1 Part I: Numerical Analysis Methods

Here, an overview is presented of the various numerical methods which will be employed systematically throughout the rest of the thesis. The methods discussed here are post-processing or algorithmic methods which can be applied to time-domain numerical data; in principle this process is independent of which commercial or custom software platform is used as a calculation engine. On a broad scale, these techniques parallel established methods in the RF computational electrodynamics literature, which are not necessarily discussed widely in the plasmonics community. This section will also highlight a variety of extensions specific to a nanophotonic design "toolbox," and in several cases reference experimental studies which corroborate the numerical analysis.

Chapter 2 develops techniques to analyze resonant nanostructures, such as small metal particles. The principal technique employed is impulse excitation ringdown spectroscopy, which allows the critical advantage of generating broadband spectra from a single time-domain simulation. Once the resonance spectrum is determined, time-domain techniques can also be used to find cavity parameters such as the local field enhancement factor f, effective mode volume V, and quality factor Q.

In Chapter 3, simulations of plasmonic waveguiding structures are studied. Fourier-space analysis is used to reveal the dispersion properties of waveguides, and to perform mode filtering. Full-field simulation is most valuable as a tool for characterizing non-analytic geometries, such as the incoupling to waveguides from scattering objects such as grooves. To this end, we demonstrate the use of phasor field subtraction to

isolate scattered fields from a subwavelength object. Numerical calculation of the local energy dissipation via divergence of the Poynting vector is introduced as a metric for differentiating thermal loss from "good" absorption, e.g., in a solar cell.

1.5.2 Part II: Resonant Plasmonic Nanostructures

The theme of Part II is resonant plasmonic nanostructures, especially small metal nanoparticles. The first two chapters explore the plasmonic resonances of nanoparticles which act as very strongly coupled dipole scatterers, in order to achieve extreme enhancement of the local electromagnetic field. The strongest local field confinement comes from very small particles which are very close together, and to this end (Chapter 4) describes an unusual fabrication technique in which high-energy ion beam irradiation is used to form linear chains of 10 nm Ag particles, only a few nm apart, in a glass matrix. We indeed observe very strong anisotropy in the optical properties of the glass. Finite element finite difference time-domain (FDTD) methods employing impulse-excitation ringdown spectroscopy are used to correlate the observed nanostructure and spectral data in Chapter 5, building confidence in the use of FDTD to describe the local electromagnetic environment of the tiny particle arrays.

In Chapter 6 the focus changes from basic science to an intriguing application. Theory predicts that the radiative rate of a dipolar emitter, such as that of nanocrystalline Si, can be modified by near-field coupling to a passive dipole, such as an Ag nanoparticle. Finite element methods are used as a design tool to help generate an "nanoantenna" array of metal particles with variable resonant frequency. The observed optical extinction spectra of the fabricated arrays provide additional confirmation of the accuracy of the impulse-ringdown method. Furthermore, the simulated field enhancement is found to correctly predict the actual photoluminescence enhancement, supporting the predictive power of our numerical method. In Chapter 7, impulse-ringdown spectroscopy is successfully applied to analysis of an entirely different form of microcavity, formed by a grating in a metal surface.

1.5.3 Part III: Guided-Wave Plasmonics

Part III deals with analysis of guided wave plasmonics. Chapter 8 introduces metal/insulator/metal (MIM) or "plasmon slot" waveguides via a semi-analytic numerical solution. These waveguides are rapidly becoming a staple of nascent plasmonic device applications due to favorable trade-off between confinement of fields to the dielectric core, and relatively low loss. This chapter also serves to provide context for the applicability of full-field time domain simulation in MIM applications. Since the characterization of steady-state waveguide modes proves analytically tractable, the great value for FDTD analysis is in low-symmetry structures such as in-couplers and junctions and for providing rapid feedback in support of device prototyping, as in Chapter 9.

Part I

Numerical Analysis Methods

Chapter 2

Impulse Excitation Analysis of Resonators

2.1 Introduction

This chapter reviews numerical methods used to generate the wide-band spectral response from a single time domain simulation of a plasmonic resonator[1]. Here, we will focus initially on the simple example of a small, spherical metallic shell.

A plasmonic resonator, such as our exemplary metal shell, acts as a damped, harmonic oscillator. The free electrons in the metal feel a driving force in the presence of an applied electromagnetic field, and a restorative force that depends on the resulting induced non-equilibrium polarization. The resonant frequency is an intrinsic property of the particle and depends on the shape and the optical properties of the particle itself, and of its dielectric environment.

In order to find the resonant frequency, we need to generate an appropriate impulse function. Consider the case of an analogous harmonic oscillator, a damped mechanical spring, for which the appropriate initializing impulse would be a state where the spring is stretched and suddenly released. The resonance frequency of the spring can be observed by monitoring the length of the spring as a function of time as it oscillates, or "rings down," following the impulse excitation. In the case of our metallic particle, the corresponding impulse excitation is the spontaneous application of a non-equilibrium charge distribution. We will present the method in which we can generate this impulse initialization in finite-element time domain electromagnetic

[1] Material used in this chapter is compiled from References [107, 131] as well as previously unpublished work performed in collaboration with C. E. Hoffman.

calculations and analyze the resulting ringdown response.

2.2 Impulse Excitation, Resonant Ringdown Method

Our sample resonant structure is a metallodielectric "core-shell" particle, that is, a metal sphere, composed of a dielectric core surrounded by a metallic shell. The plasmon frequency of these particles can be tuned throughout the visible and near-infrared part of the spectrum by varying core diameter and shell thickness [1, 91, 96]. Additional tuneability can be obtained by shape anisotropy, which induces a splitting of the plasmon resonance in red-shifted longitudinal and blue-shifted transverse plasmon bands [14, 103, 104, 139].

The inner radius is $R_{core} = 228$ nm; the shell itself is a layer of Au with thickness $t_{\mathrm{Au}} = 38$ nm. The core material and the surrounding medium are both considered as a dielectric with index $n = 1.45$, while the optical response of Au is determined with a Drude model:

$$\varepsilon(\omega) = \varepsilon_d - \frac{\omega_p^2}{\omega^2 + i\omega\gamma} \tag{2.1}$$

with $\varepsilon_d = 9.54$, $\omega_p = 1.3 \times 10^{16}$ rad/s, and $\gamma = 1.25 \times 10^{14}$ rad/s. This structure is input into a commercial finite element time-domain software package [48] with a graded mesh to minimize any error due to discretization of the curved surface.

We next seek to initialize resonant "ringdown" of our particle by applying an impulsive excitation. This technique is motivated by a common method in the radiofrequency (RF) time domain computation literature, in which the broadband frequency response of an antenna can be found by driving it with a Gaussian modulated pulse. The finite length of the pulse in the time domain is Fourier equivalent to a wide band excitation. Using an initialization procedure which is conceptually similar but employs an effectively instantaneous impulse, the strategy is to instantaneously apply a non-equilibrium polarization charge distribution to the particle that is similar to the charge distribution of the particle's natural mode(s) of resonance. In practice to build up such an impulse, the simulation volume is illuminated with a low-frequency source, switched on gradually and allowed to come to steady-state. The source may be either a plane wave or a point dipole, and the excitation frequency is arbitrary, assuming it is low compared to any resonance of interest in the struc-

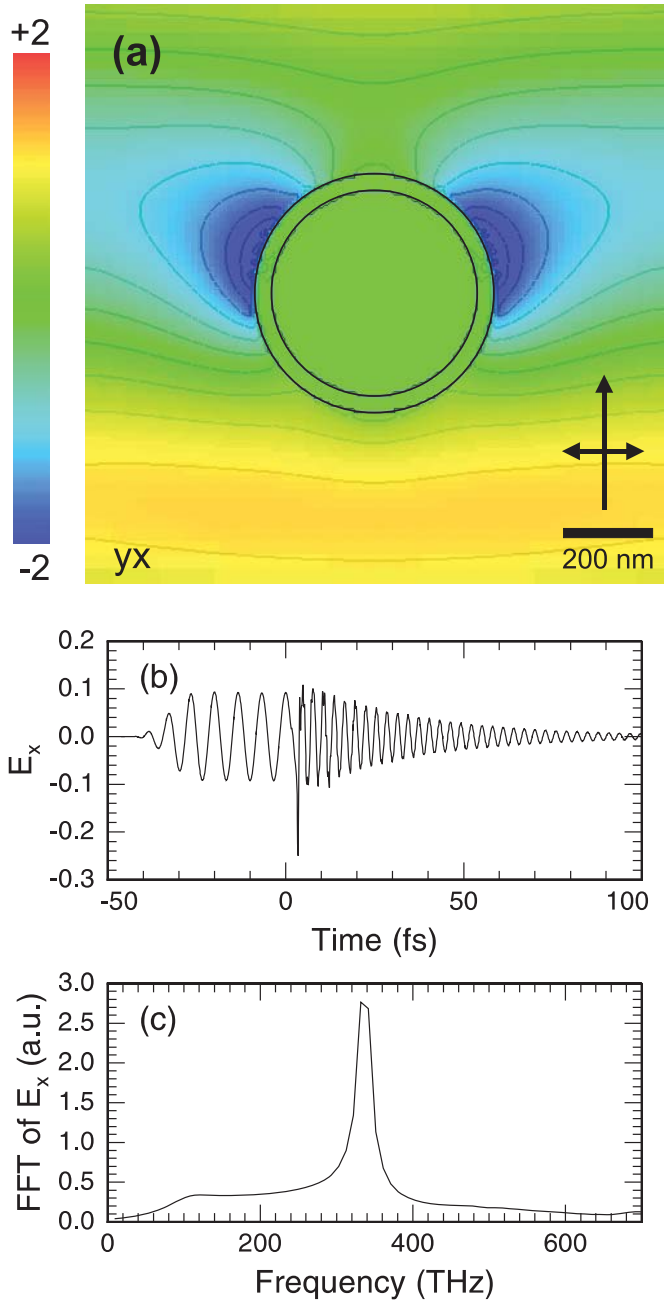

Figure 2.1: Impulse excitation ringdown spectroscopy of a metallic shell. In panel **(a)**, the x-component of the electric field, E_x, of a plane wave propagating in the y-direction, at a frequency of 150 THz, and interacting with a spherical Au shell (inner radius $R_{\text{core}} = 228$ nm, thickness $t_{\text{Au}} = 38$ nm) embedded in silica ($n = 1.45$). **(b)** Impulsive excitation and subsequent relaxation trace of the E_x field in a monitor point in the center of the particle. The initializing plane-wave is turned on $t = -40$ fs, and abruptly turned off at $t = 0$. **(c)** Fast Fourier transform of the ringdown of E_x, showing a resonance peak at a frequency of 335 THz

ture. The simulation is paused in the steady-state once the particle has become polarized. The driving field is abruptly turned off and, additionally, the magnetic field is set to zero in all space. The result is a purely electric polarization field, corresponding to a static nonequilibrium charge distribution. Time evolution of the simulation is then restarted, and the electromagnetic fields are monitored in the time domain as any particle modes excited by the impulse ring down. Finally, this signal is transformed into the frequency domain by a fast Fourier transform (FFT) to provide spectral characteristics of the particle resonances. The method described above is illustrated in Figure 2.1.

Since absorption and ringdown are resonant phenomena, the frequency at which the peak FFT response occurs is directly comparable to the frequency of maximum absorption in an optical spectrum. This comparison has been tested in several studies against other theoretical methods [107] and experiment [131], used successfully as a predictive design tool [13], and extended to other types of plasmonic resonators beyond small metal particles [55].

2.3 Selection of Individual Modes by On-Resonance Excitation

This section further investigates a metallic resonator, using on-resonance time domain excitation. Here we will study a slightly different sample system, again a metallodielectric core shell particle, but with cylindrical rather than spherical symmetry. Specifically the particle consists of a cylindrical Si core with length $l = 500$ nm and radius $R_{\text{core}} = 100$ nm, with the outer radial surface coated with an Ag shell with thickness $t_{\text{Ag}} = 100$ nm, and embedded in an outer medium of air (cf. Figure 2.2. An interesting feature of this particle is that it supports multiple longitudinal modes, similar to the acoustic modes of an organ pipe. Each mode can be isolated and studied individually by impulse-excitation ringdown spectroscopy, as described in Figure 2.3. First, the multimodal spectrum is determined via a single wideband simulation, with the impulsive charge distribution generated by internal point dipole sources driven at a low, off-resonance frequency. The ringdown dynamics reveal the multiple modes of the particle. Then, individual modes are isolated using an impulse generated by excitation at the peak frequencies observed in the modal spectrum.

The mode spectrum excited in a multimodal resonator is also influenced by the spatial symmetry of

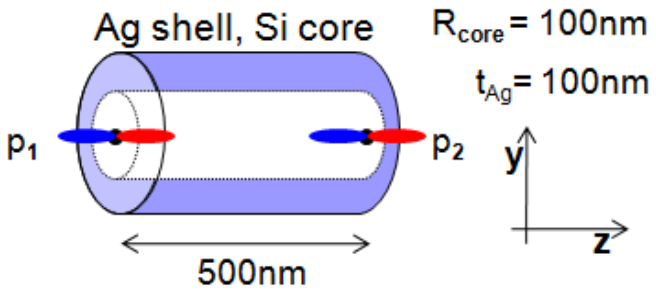

Figure 2.2: Schematic of 500 nm long cylindrical core-shell particle with a Si core of radius 200 nm and Ag shell with 100 nm thickness. Impulse fields are generated by z–oriented point dipole sources at points p1 and p2.

the initial impulse charge distribution. Consider, as above, driving the cylindrical core-shell particle with two dipole sources located at the end facets' centerpoints, corresponding to points p1 and p2 in Figure 2.2. Here the frequency, orientation, and amplitude of the two dipole sources are identical, but they are allowed to have nonzero relative phase. As illustrated in Figure 2.4, the source phase can be used to select the symmetry of modes that are excited in the simulation. In the top row, in-phase excitation produces an impulse charge distribution which selectively excites the "odd" modes of the resonator. In the bottom row, anti-phase excitation selects the resonators' "even" modes. In general, a phase difference other than 0 or π, or a less symmetric spatial distribution of sources, can be used to generate a superposition of both odd and even modes. This technique is applied in Chapter 7, where superposition of odd and even impulse sources is used to identify modes of either symmetry in an annular surface resonator.

The simulated, time-averaged local electric fields corresponding to any isolated resonance can be transformed into the modal free charge distribution $\sigma = \nabla \cdot E$. In many cases the physical character of the various modes of a resonator can be visualized more readily as a scalar charge distribution than as a vector field. For example, Figure 2.5 shows a simulation of a core–shell particle in which the Au shell is so thin that surface charges on the inner and outer surface of the shell are strongly coupled to one another. Calculation of σ allows characterization of the resulting hybridized modes as "symmetric" (mode 1) or "antisymmetric" (mode 2) based on the relative phase of charge oscillation on each interface.

Selective-frequency mode excitation allows for several quantitative measurements to be made on the simulated resonator. Measurements of fundamental importance include the quality factor of the cavity Q, and

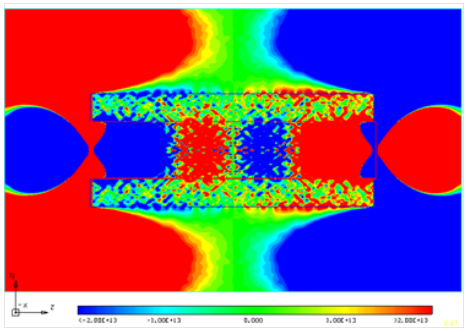

(a) Wideband impulse field, generating frequency $f = 200$ THz.

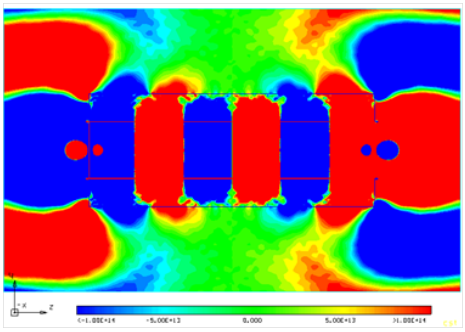

(b) Resonant impulse field, generating frequency $f = 561$ THz.

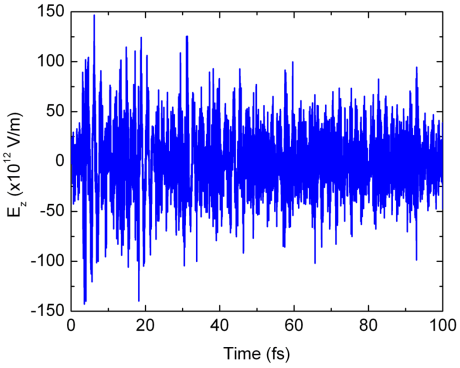

(c) Wideband time-domain ringdown.

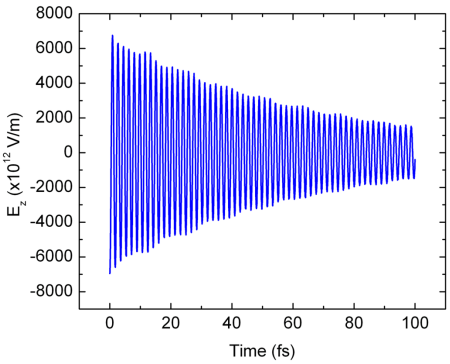

(d) Resonant time-domain ringdown.

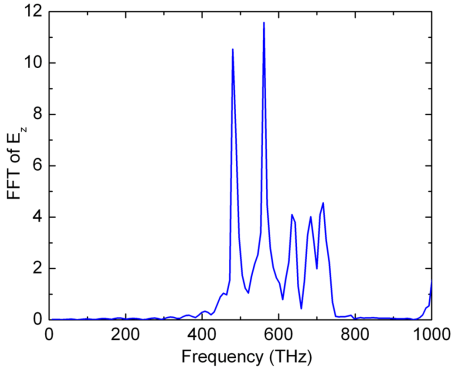

(e) Wideband FFT spectrum.

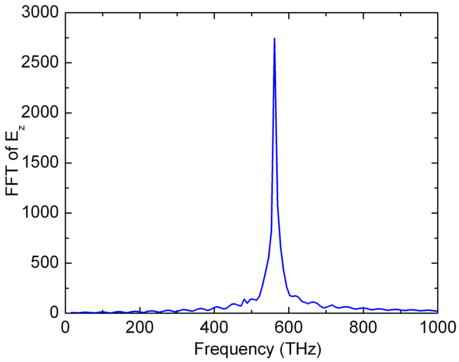

(f) Resonant FFT spectrum.

Figure 2.3: Impulse excitation analysis of a multimodal, cylindrical Si/Ag core-shell resonator. The panels of the left column illustrate initial multimode spectral characterization: **(a)** The impulsive electric field distribution generated by an internal point dipole source driven at arbitrary, off-resonance frequency ($\nu = 200$ THz). **(c)** Wideband, time-domain ringdown behavior generated by off-resonance impulse. **(e)** Fast Fourier transform (FFT) of (c), revealing the several modes of the particle. The panels of the right column illustrate subsequent isolation of a single resonance: **(b)** An impulsive electric field generated by an internal point dipole source driven at on-resonance frequency ($\nu = 561$ THz), corresponding to the largest peak observed in (e). **(d)** Single-exponential ringdown behavior of a resonantly excited mode. **(f)** FFT spectrum of (d) revealing a single resonant peak.

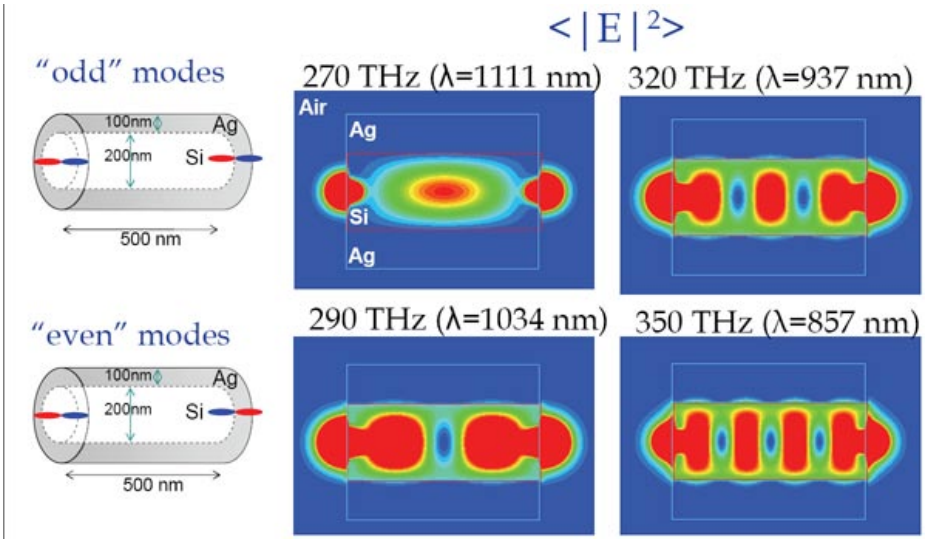

Figure 2.4: Mode selection by controlling symmetry of impulse function

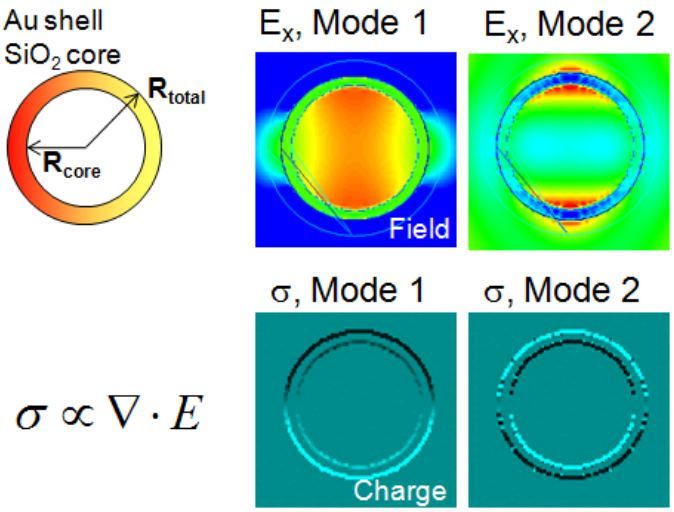

Figure 2.5: Characterization of selected modes by field divergence

the local enhancement of electromagnetic fields as a function of position $f(x,y,z)$. The quality factor is a measure of the lifetime of energy stored in a resonator, often described colloquially as the average number of "round trips" that a quantum of energy is expected to make in the cavity before being dissipated.

$$Q = 2\pi\nu\tau, \tag{2.2}$$

where ν the frequency and τ the decay time are determined by a fit to the exponential decay of observed harmonic ringdown. For example, for the spherical shell of Figure 2.1(c), $Q = 35$. Thicker gold shells, up to $t_{\mathrm{Au}} = 90$, are found to have higher quality factors ($Q > 150$) [107], at the cost of increased screening of the particle core from the outside world. The multimodal, cylindrical resonators of Figure 2.3 have observed quality factors ranging from $Q \approx 30$ for high-order modes, to $Q = 120$ for the fundamental mode.

The local enhancement of electromagnetic fields is perhaps the most important parameter, as it is a direct measurement of the ability of a plasmonic resonator to concentrate light in nanoscale volumes. We calculate this quantity by numerically generating a map of the time averaged field intensity for a system driven at steady-state at a frequency of interest ν,

$$< E^2 > (x,y,z) = \frac{1}{N} \sum_{(n=1)}^{N} E^2(x,y,z;t = t_0 + n\Delta t) \tag{2.3}$$

where, given the period of an optical cycle $T = 1/\nu$, the field intensity is averaged over N time steps where $(N\Delta t)$ is an integer or half-integer multiple of T. To avoid discretization error the calculation time step (Δt) should be ideally no greater than $T/20$. However, it is generally a much greater time step than the elementary time step of the underlying FDTD simulation. Since the calculation is performed at steady-state, the initial phase does not matter (starting time t_0 arbitrary).

In the common special case of a quasistatic particle, for example, a metallic sphere much smaller than the wavelength of excitation, the harmonically driven fields at all points will be oscillating with the same phase, that is, $E(x,y,z,t) = E_0(x,y,z)e^{\mathrm{i}(\omega t+\phi)}$. In this case the time average field can be inferred from a single time "snapshot,"

$$< E^2 >_{\text{quasistatic}} (x,y,z) = \frac{1}{2} E_0^2(x,y,z). \tag{2.4}$$

This method removes the computational burden of processing N full-field data sets, but does instead requires selection of a snapshot with time t_0 such that $e^{i(\omega t_0 + \phi)} = 1$.

The field intensity enhancement factor is determined by the ratio of the local field intensity to that of the incident driving field,

$$f(x,y,z) = \frac{< E^2 > (x,y,z)}{< E^2_{\text{incident}} >}. \tag{2.5}$$

A variety of figures of merit (f.o.m.) can be constructed from the quality Q, intensity enhancement f, and modal volume V. The construction of an appropriate f.o.m. depends critically on the target application. As an example, consider using plasmonic shell particles to enhance the spontaneous emission rate of an optical emitter placed inside the particle core. For this application the f.o.m. is the Purcell factor [111],

$$P = \frac{3}{4\pi^2} \left(\frac{\lambda}{n} \right)^3 \frac{Q}{V}. \tag{2.6}$$

Using the parameters of the spherical core-shell particles of Figure 2.1, $Q = 150$ and $V = 0.07(\lambda/n)^3$, a significant spontaneous emission enhancement is predicted of $P = 140$. For further discussion of spherical core-shell particles, refer to Reference [107]. See also discussion of effective mode volume in plasmonic cavities in Reference [78].

Chapter 3

Fourier Mode Spectrum Analysis

3.1 Introduction

This chapter discusses numerical methods relevant to Fourier (wavevector-space) mode spectrum analysis (FMSA) of propagating waves. These methods are suitable for post-processing of a finite-difference time-domain (FDTD) simulation capturing the steady-state behavior of a plasmonic waveguide device illuminated with continuous wave, monochromatic input[1]. In particular, our input for FMSA calculation is a map of time-harmonic electromagnetic fields with a known drive frequency ω_0. From this data set, we wish to determine the spectrum of energy propagating with wavevector k. Typically the resulting spectrum will contain peaks corresponding to various waveguided modes. We are interested in quantitatively characterizing each such mode, i.e., measuring the spatial energy density profile of the modal electromagnetic fields, calculating the linewidth of the mode in the frequency domain, and determining the propagation length in the guide. In addition to analyzing the mode spectrum, a set of techniques will be generated to connect the simulated dataset to other useful design figures of merit, such as the in-coupling power efficiency of a waveguide junction, or the parasitic loss for a given device.

First, techniques for the conversion of "raw" time domain simulation results into suitable time-harmonic data will be reviewed. Then, Section 3.3 will demonstrate the FMSA method, using as an illustrative example a simulation of a basic multimode metal-insulator-metal plasmonic waveguide.

[1] The methods described in this chapter are previously unpublished, developed in collaboration with V. E. Ferry.

3.2 Preprocessing Time-Domain Data for Mode Spectrum Analysis

3.2.1 Construction of time-harmonic fields

The unprocessed output from a finite-element time-domain calculation consists of all the electric and magnetic field components, at every grid cell position and at every time step. Assuming typical values of 1×10^6 grid cells and 1×10^4 time steps, and at least 3 field components in the case of a two-dimensional simulation, this represents a relatively intractable set of 3×10^{10} data points. In order to analyze the spatial information content, that is, the wavevector of propagation in our simulations, the spatial resolution must be maintained. However, the data from the time domain can be reduced to a complex-valued, time-harmonic field using a discrete Fourier transform (DFT),

$$F(\omega) = \int_0^T f(t)e^{-i\omega t}dt = \Delta t \sum_{n=0}^{N} f(n)e^{-i\omega n\Delta t}. \tag{3.1}$$

Here $f(t)$ represents any field component in any one grid cell as a function of time, and N the number of time steps over which the discrete calculation is performed. Therefore in the limit that a simulation reaches a true steady-state, and in the special case where the analysis frequency equals the continous wave drive frequency $\omega = \omega_0$, the N time domain data can be compressed losslessly to a single complex number. Ideally the DFT calculation is performed recursively in real time during the course of the finite element simulation; in this case it is possible to compile terms at every time step without writing to disk a significant amount of extra data. Otherwise, data storage provides a practical limit to the number of terms N and resolution $n\Delta t$.

It is also possible to employ DFT in conjunction with wideband excitation, such as a pulse with Gaussian envelope of finite width, to generate data for many frequencies from a single FDTD run. See for example, the discussion of wideband far-field conversion in Taflove [132]. However, caution is advised in applying this method to analysis of strongly dispersive channels, which may introduce error through pulse distortion.

3.2.2 Scattering via linear field subtraction

For many applications we are interested in studying propagating surface waves which are launched by a local scattering center, such as a groove in a metallic surface. A full-field FDTD simulation of this in-coupling

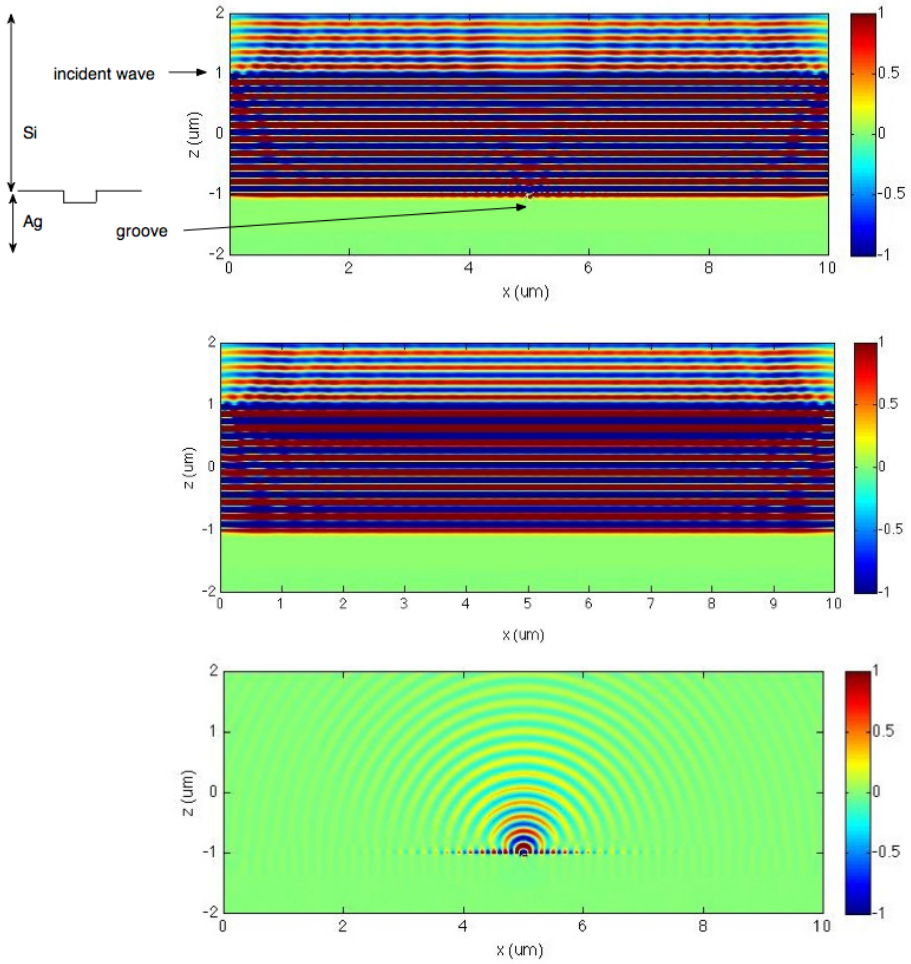

Figure 3.1: Determination of scattered fields by subtraction. Top: Total magnetic field H_{total} generated by a wave incident upon a subwavelength groove (located at x=5 μm, z=-1 μm) in a Si/Ag surface (z=-1μm). Center: Field H_{control} generated by a wave reflecting from a Si/Ag surface with no groove. Bottom: Scattered field determined by subtraction, $(H_{\text{total}} - H_{\text{control}})$

structure generates a complicated field pattern formed by interference of the incident beam (H_{inc}) with the fields reflected from the smooth metal surface (H_{r}) and with fields scattered from the groove (H_{s}). This interference can prove an obstacle to performing accurate calculations on the scattered fields. However, when working with the complex valued time-harmonic fields, it is straightforward to isolate the scattered field contribution by employing linear subtraction.

In Figure 3.1, we study a subwavelength (width w= 100 nm, depth d= 50 nm) groove in a planar Si/Ag interface. In this simulation the scatterer is illuminated by a continuous wave source (wavelength λ_0= 1000 nm) normal to the surface. The metal interface is located at the plane $z = -1$ μm, and the incident wave is generated in the plane $z = 1$ μm. In the top panel of Figure 3.1, the resulting magnetic field $\mathbf{H}$ is displayed. Notice in the region of interest ($-1 < z < 1$) the interference pattern generated by the sum of the component fields, $\mathbf{H}_{\text{total}} = \mathbf{H}_{\text{inc}} + \mathbf{H}_{\text{r}} + \mathbf{H}_{\text{s}}$. Note that behind the input plane in the region $z > 1$, only the fields $\mathbf{H}_{\text{r}} + \mathbf{H}_{\text{s}}$ are observed. Next, we run a "control" simulation with only a smooth metal surface and no groove. All other parameters are identical, so that in the region of interest $\mathbf{H}_{\text{control}} = \mathbf{H}_{\text{inc}} + \mathbf{H}_{\text{r}}$, which is shown in the center panel of Figure 3.1. Finally, the scattered field is determined by subtraction,

$$\mathbf{H}_{\text{s}} = \mathbf{H}_{\text{total}} - \mathbf{H}_{\text{control}}. \tag{3.2}$$

After subtraction the scattered field is cleanly isolated, as shown in the bottom panel of Figure 3.1. By performing subtraction of all the complex-valued electric and magnetic field components, the propagating scattered fields can be accurately determined in all regions of the simulation volume external to the scattering object. As a sample application, consider comparing the power scattered from the subwavelength groove in a Si/Ag surface as discussed above, with that from a ridge of the same width and height. In each case the scattered fields are calculated by subtraction and then energy flow is determined using the time-harmonic form of Poynting's theorem,

$$\langle \mathbf{S} \rangle = \frac{1}{2} \Re(\mathbf{E_s} \times \mathbf{H_s}^*), \tag{3.3}$$

where $\langle \mathbf{S} \rangle$ is the power flow (averaged over an optical cycle), $\mathbf{E_s}$ the electric field launched from the scatterer

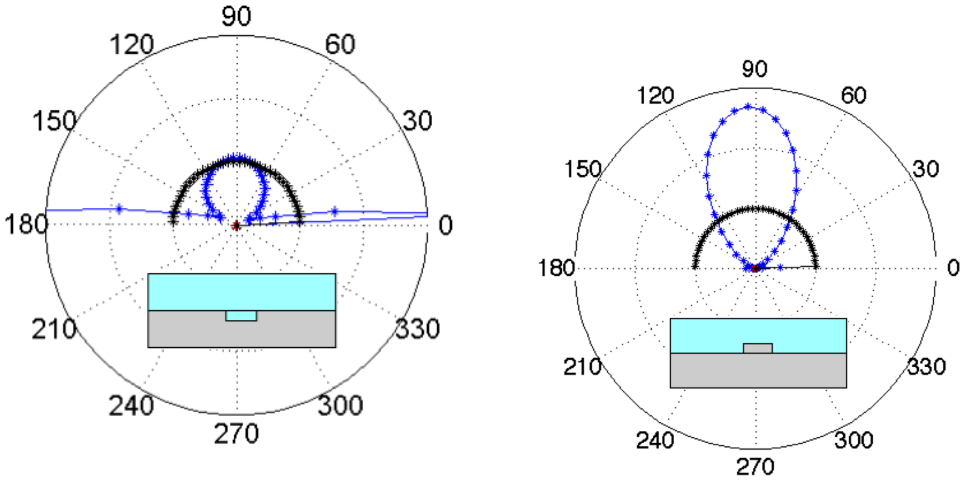

(a) Groove (b) Ridge

Figure 3.2: Normalized scattered power versus angle from subwavelength scattering centers in a Si/Ag surface. In each panel the blue line represents the calculated scattered power; the dark line an isotropic source with the same normalized total output power.

and $\mathbf{H_s}^*$ the complex conjugate magnetic field. Figure 3.2(a) shows (blue line) the normalized scattered power per unit angle, determined by projection of the Poynting vector upon a closed rectangular surface in the near field of the scatterer. Lobes at angles near 0°and 180°demonstrate significant coupling of scattered energy into propagating surface modes. The dark line, provided for comparison, represents a hypothetical isotropic source with the same total power. In Figure 3.2(b), we find that the scattering from the ridge has a qualitatively different form: the fraction of power coupled into surface modes is almost negligible.

3.3 Fourier Mode Spectral Analysis Method

In this section the method of Fourier space mode spectral analysis (FMSA) is illustrated on a two-dimensional simulation of transverse magnetic propagation in a metal-insulator-metal (MIM) waveguide structure. The insulating waveguide core is modeled as a 500 nm thick layer of nitride (Si_3N_4), with non-dispersive index $n = 2.02$. The cladding metal layers are optically thick layers of Ag, with dispersive optical properties as described in Table B.4. The waveguiding properties of this relatively simple structure are solvable by semi-analytic methods [32] and therefore provide a suitable controlled test of the FMSA technique. For excitation at visible frequency, this 500 nm core waveguide supports both plasmonic and conventional modes. Bound

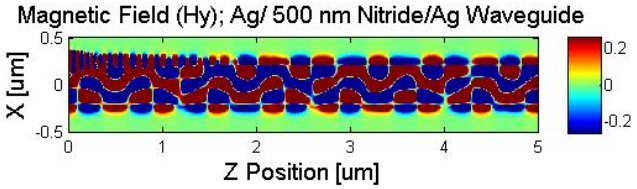

Figure 3.3: Simulated H_y propagation in a multimode Ag/nitride/Ag waveguide with 500 nm thick core. Several plasmonic and conventional guided modes are present.

plasmonic modes are characterized by field maxima at the metal-dielectric interface and by large wavevectors ($k > \frac{2\pi n}{\lambda_0}$). Conversely, conventional or "photon-like" modes are characterized by one or more field maxima inside the waveguide core, minimal penetration of field into the metallic cladding, and small wavevectors (generally, if not strictly, $k < \frac{2\pi n}{\lambda_0}$).

Figure 3.3 shows a visualization of magnetic fields from FDTD simulation of the Ag/nitride/Ag waveguide, generated with an input plane at $z = 0$ which launches surface modes on the metal-insulator interface at $x = 0.25$ μm. As discussed in Section 3.2.1 the simulation is performed with continuous wave input, in this case with $\omega = 2.50$ eV (free space wavelength λ_0 = 496 nm), and the resulting fields are captured in time harmonic form by DFT. Examining "by eye" the image of $\mathbf{H_y}$, it is clear that energy has indeed been coupled both into a plasmonic mode (short wavelength, confined to $x = 0.25$ μm interface) and into one or more photonic modes.

The propagation direction z is related to the wavevector k by the Fourier transform pair,

$$f(k) = \int F(z) e^{-\mathrm{i}kz} dz, \tag{3.4}$$

$$F(z) = \frac{1}{2\pi} \int f(k) e^{\mathrm{i}kz} dk. \tag{3.5}$$

Therefore we can transform each electromagnetic field ($\mathbf{E}_x(x,z), \mathbf{E}_z(x,z), \mathbf{H}_y(x,z)$) to wavevector space

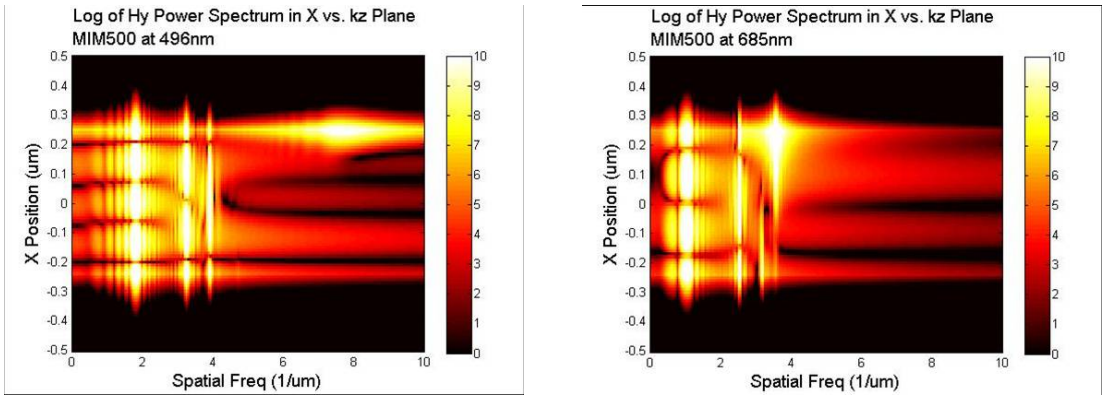

(a) $\omega = 2.50$ eV (λ_0 = 496nm)

(b) $\omega = 1.81$ eV (λ_0 = 685nm)

Figure 3.4: Fourier space power spectral maps of a Ag/nitride/Ag waveguide with a 500 nm core, with incident frequency of **(a)** $\omega = 2.50$ eV **(b)** $\omega = 1.81$ eV

$(\mathbf{e}_x(x,k), \mathbf{e}_z(x,k), \mathbf{h}_y(x,k))$ by employing a one-dimensional fast Fourier transform (FFT) along the z axis. Note that the x axis remains untransformed. In order to visualize the energy content of the modes in Fourier space, we calculate a power spectrum,

$$|\mathbf{h}_y(x,k)|^2 = \mathbf{h}_y(x,k)\mathbf{h}_y^*(x,k). \tag{3.6}$$

Such Fourier-space power spectra appear in Figure 3.4. The horizontal axes are the propagation wavevector k_z, expressed in wavenumber units (μm^{-1}). Vertical axes are position in the x direction, that is, transverse to the propagation direction. The left panel depicts the data for drive frequency $\omega = 2.50$ eV (λ_0 = 496 nm). Three bright, vertical streaks which appear at approximately 2, 3.5, and 4 μm^{-1} represent the three photonic modes which are present in the waveguide. The mode number can also be inferred from this plot; note that the streaks have four, three, and two (respectively) field nodes in the waveguide core $-0.25 < x < 0.25$. Another bright spot at 8 μm^{-1} represents another feature which can be identified as the plasmonic mode by its high k, broad linewidth, and localization at the $x = 0.2$ surface. In the right panel is a power spectrum generated with a significantly lower drive frequency, $\omega = 1.81$ eV (λ_0 = 685 nm). At this lower energy, notice that the highest-order photonic mode no longer "fits" in the guide, and is cut off.

Since the fields are distinguishable by k in Fourier space, we may perform analysis on individual modes that was not possible in the Cartesian (x,z) domain. For example, the energy content of each mode can be

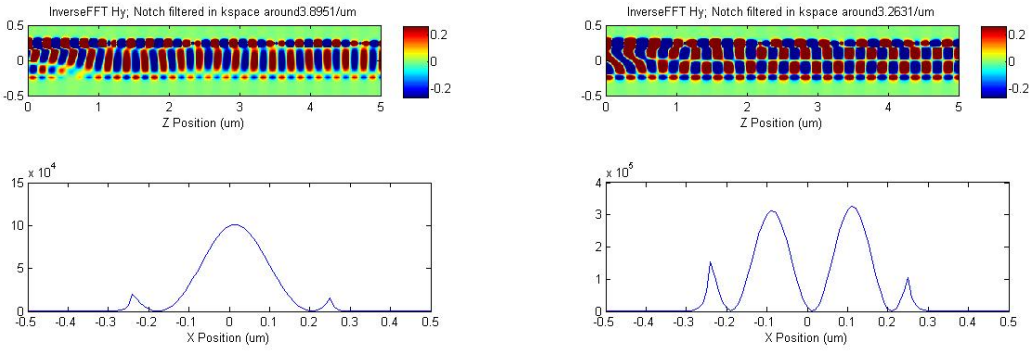

(a) Filter center: $k_i = 3.90\ \mu\text{m}^{-1}$

(b) Filter center: $k_i = 3.26\ \mu\text{m}^{-1}$

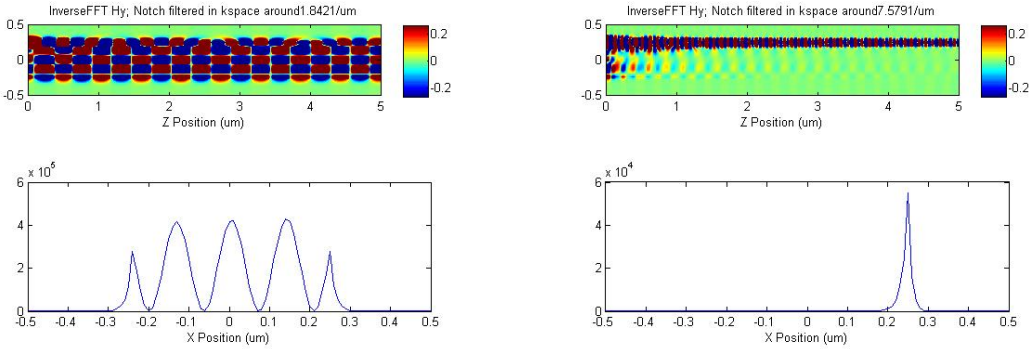

(c) Filter center: $k_i = 1.84\ \mu\text{m}^{-1}$

(d) Filter center: $k_i = 7.58\ \mu\text{m}^{-1}$

Figure 3.5: Mode isolation by Fourier space filtering, and subsequent inverse transform back to Cartesian space. All panels are for Ag/nitride/Ag waveguide with 500 nm core, with four different notch pass filters applied in Fourier space.

determined by integrating the energy in each "streak." As a further demonstration, we isolate each mode using notch pass filters in Fourier space. Each filter has the simple rectangular form

$$\chi(k) = \left\{ \begin{array}{ll} 0, & |k| < k_{\text{lo}} \\ 1, & k_{\text{lo}} < |k| < k_{\text{hi}} \\ 0, & k_{\text{hi}} < |k| \end{array} \right\}. \tag{3.7}$$

Modal fields in Cartesian space (x,z) are then simply obtained by applying the inverse FFT to fields which have been filtered in Fourier space. In Figure 3.5, we demonstrate the procedure of mode isolation by Fourier space filtering, and inverse transform back to Cartesian space. All panels are for Ag/nitride/Ag waveguide with 500 nm core, with four different notch pass filters applied in Fourier space. Within each

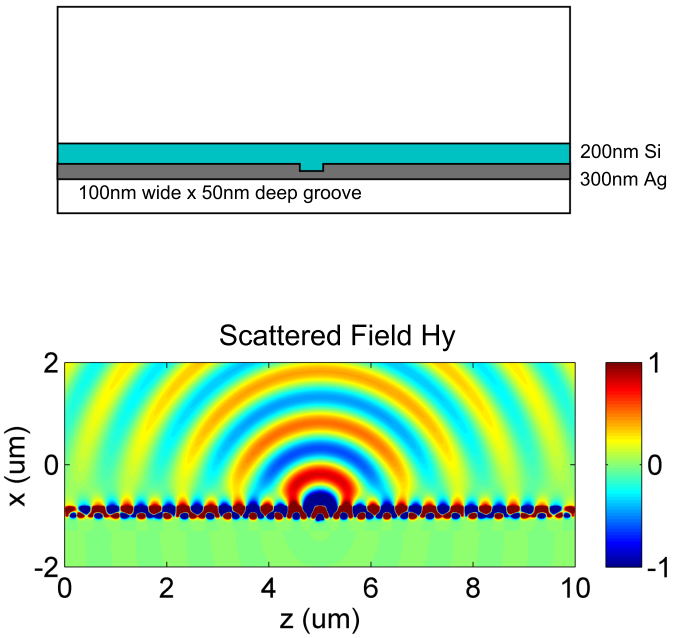

Figure 3.6: Scattering from a subwavelength groove in a Si/Ag interface. Top: Schematic of the structure, a 200 nm Si film on a 300 nm Ag substrate, with a 100 nm wide by 50 nm deep groove. The structure acts as a multimode photonic and plasmonic waveguide. Bottom: Light (TM polarized, $\lambda = 1000$ nm) scattered from the groove at normal incidence.

panel, the subpanels are: (top) H_y modal field after inverse Fourier transform, (bottom) corresponding cross section through power spectrum $|\mathbf{h}_y(x,k)|^2(x,k)$ along the x axis for given filter center frequency k_i.

3.4 Application of FMSA to Characterization of Groove In-coupling

In this section the methods discussed above are combined to quantify the incoupling of light, interacting with a single subwavelength groove, into the propagating modes of a surface plasmon waveguide. As in Figure 3.1, incident light is scattered from a 100 nm wide by 50 nm deep groove in a Si/Ag metallodielectric surface. In the present case, however, the structure as illustrated in Figure 3.6 consists of a thin 200 nm film of Si on a 300 nm thick layer of Ag. This stack acts as a multimode waveguide, supporting hybrid "photonic" as well as surface plasmonic modes.

The Fourier-space intensity spectrum is generated by transform over the $\hat{z}$ spatial dimension to analyze the energy incoupled into the guided surface modes. The Fourier intensity spectrum is represented on a

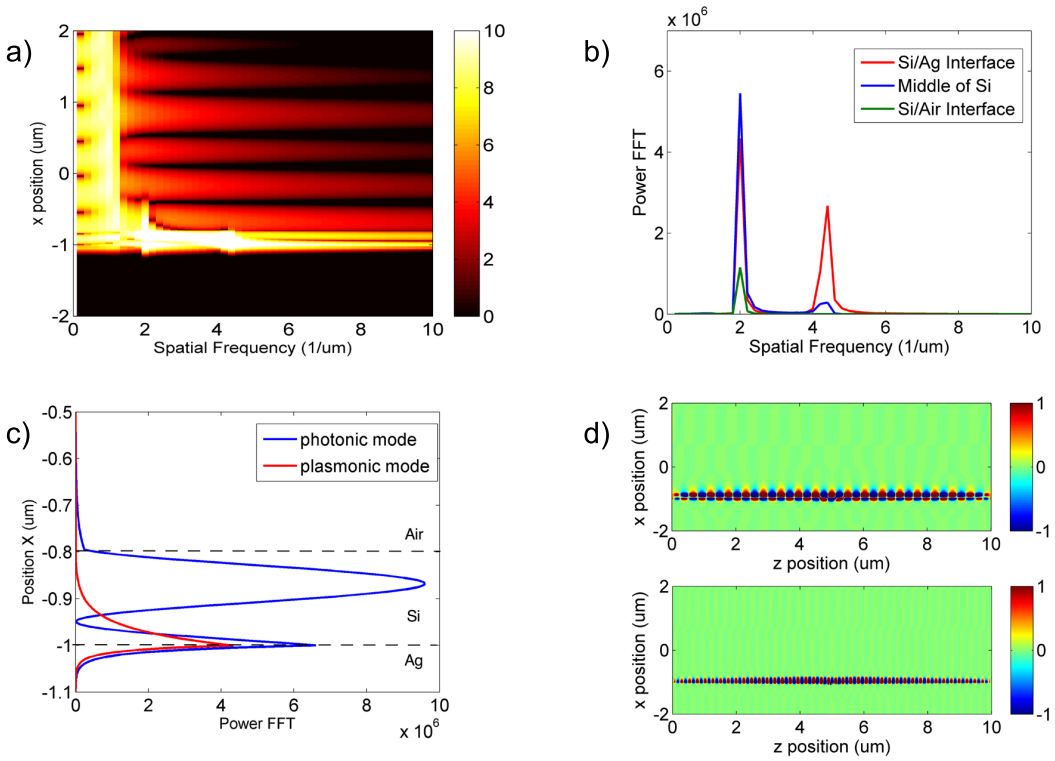

Figure 3.7: Fourier space analysis of scattering from a subwavelength groove in a thin-film-Si on Ag surface. **(a)** Fourier-space intensity spectrum, on logarithmic scale. **(b)** Mode spectrum: intensity versus spatial frequency. **(c)** Spatial energy profile: intensity versus transverse position. **(d)** Photonic (top) and plasmonic (bottom) modes inverse-transformed back to direct space.

logarithmic scale in Figure 3.7(a), where the horizontal axis shows the transform spatial frequency, while the vertical axis corresponds to the untransformed transverse position in the $\hat{x}$ direction. The key information contained in this data can be parsed by observing several cross-cuts along either axis. Figure 3.7(b) shows the mode spectrum, that is, the field intensity plotted against spatial frequency at several x-positions within the device. The spectral peaks confirm the existence of two propagating modes in the waveguide, at $2\mu^{-1}$ and at $4.2\mu^{-1}$. Figure 3.7(c) is the spatial mode profile, or Fourier intensity as a function of position, generated by taking the cross-cut of 3.7(a) at the peak frequencies of the two modes. This plot allows us to visualize where the energy is localized in each mode. The peak at $4.2\mu^{-1}$ is shown in red; it is plasmonic in character, confined to the Si/Ag interface with intensity falling off exponentially on either side. The hybrid "photonic" mode at $2\mu^{-1}$ is plotted in blue. In Figure 3.7(d), the fields, filtered in Fourier space, are inverse-transformed back to direct space.

Part II

Resonant Plasmonic Nanostructures

Chapter 4

Mega-Electron-Volt Ion Beam Induced Anisotropic Plasmon Resonance of Silver Nanocrystals in Glass

30 MeV Si ion beam irradiation of silica glass containing Ag nanocrystals causes alignment of Ag nanocrystals in arrays along the ion tracks[1]. Optical transmission measurements show a large splitting of the surface plasmon resonance bands for polarizations longitudinal and transversal to the arrays. The splitting is in qualitative agreement with a model for near-field electromagnetic plasmon coupling within the arrays. Resonance shifts as large as 1.5 eV are observed, well into the near-infrared.

4.1 Introduction

The resonance frequency in spherical, isolated metal particles depends on the size and the dielectric constants of the metal and the surrounding medium. In ensembles of particles, electromagnetic coupling among particles causes plasmon bands to shift [44]. Numerical simulations showed the effect of particle size, next-neighbor distance, number of particles and shape of aggregates on the extinction spectra of aggregates of nanometer-sized silver spheres [112]. Significant plasmon blue- and redshifts are predicted for strongly coupled ensembles. Very recently, it was shown experimentally that such interacting metal nanoparticles can serve as miniature waveguides in which electromagnetic energy can be transported via a dipolar near-field interaction [82].

[1] This chapter has been adapted from Penninkhof, Sweatlock et al., Reference [105].

It is thus clear that nanoscale arrangements of metallic particles in glass are of great interest to study the fundamentals of plasmon interactions on small length scales. By tuning the interparticle interaction and particle shape, the plasmon resonance can be shifted to a wavelength of 1.5 μm. This may enable several applications in telecommunication, including polarization-dependent waveguides and nonlinear optical devices which take advantage of the high electromagnetic fields in plasmonic structures.

Anisotropic metal colloids can be fabricated controllably by mega-electron-volt (MeV) ion irradiation of colloidal particles which consist of a gold core surrounded by a silica shell [118]. This shape change is attributed to an anisotropic deformation effect in the silica that is known to occur in amorphous materials [126]. This chapter describes the effect of MeV ion irradiation on silver nanocrystals embedded in a planar sodalime glass film. Optical transmission data show polarization-dependent plasmon bands of silver, with red and blue plasmon shifts occurring for polarizations parallel and orthogonal to the irradiation axis, respectively. The splitting is attributed to an ion-beam-induced alignment of the Ag nanocrystals into linear arrays and can be tuned by varying the ion fluence.

4.2 Method

Silver nanocrystals were made in a sodium-containing borosilicate glass by a combination of $Na^+ \leftrightarrow Ag^+$ ion exchange and ion irradiation [108]. A 1 mm thick Schott BK7 glass wafer was immersed in a salt melt containing 5 mol% $AgNO_3$ in $NaNO_3$. One sample was ion exchanged for 7 minutes at 310 °C, and other samples for 10 minutes at 350 °C. After the ion exchange, Ag nanocrystals were nucleated by a 1 MeV Xe irradiation at normal incidence, room temperature, and $1\times10^{16}/cm^2$ ion flux. This nanocrystal formation process is well documented and ascribed to the enhanced mobility of Ag ions due to atomic displacements caused by the ion beam [23, 108]. Subsequently, the samples were subjected to a 30 MeV Si ion beam at 77 K under an angle of 60° off-normal. Si ions at this high energy exhibit very high electronic energy loss, a prerequisite for anisotropic deformation processes which are thought to be caused by the highly anisotropic thermal spike along the ion trajectory. The Si beam flux was in the range of $(15)\times10^{11}/cm^2s$. Fluences were chosen between 0 and $3\times10^{15}/cm^2$. Note that the fluences projected normal to the surface are half these

values.

Rutherford Backscattering Spectrometry was performed to determine the composition of the glass after the ion exchange. The Ag surface concentration is $\approx$ 6 at.%, and the depth profile extends to 600 nm for a 7 minute, 310 °C ion exchange and to 1100 nm for a 10 minute, 350 °C condition. The projected range of 1 MeV Xe, i.e., the depth over which silver nanocrystals are formed, is 360 nm. Simulations [148] indicate that at an incoming angle of 60°, the projected range of 30 MeV Si amounts to 4.8 μm, which is well beyond the depth of the ion exchanged region.

Optical transmission spectra were taken with a spectroscopic ellipsometer at normal incidence. Transmission electron microscopy (TEM) images were taken using a 400 keV electron beam. Preparation of plan-view TEM samples was done using a conventional backthinning method by polishing and ion milling using a 4 keV Ar ion beam under an angle of 6° with the surface.

4.3 Results

Figure 4.1 shows the optical extinction versus energy of the samples made by the 7 min/310 °C ion exchange. After the initial Xe irradiation, the ion exchanged glass shows an extinction peak at 3.0 eV (410 nm), due to the surface plasmon absorption of Ag nanocrystals in a colorless BK7 glass matrix with refractive index 1.61. This absorption band is polarization independent, as expected. From a fit of Mie theory to the spectrum [108], it is estimated that approximately 11% of the Ag ions have agglomerated into nanocrystals. After Xe irradiation the glass shows a bright yellow color. After the subsequent irradiation with 30 MeV Si ions to a fluence of 2×10^{14}/cm^2, the color of the glass changed to red and is now angle dependent. This is confirmed by the optical extinction measurements shown in Figure 4.1, taken using normal-incident light polarized either parallel (open circles) or orthogonal (closed circles) to the direction of the Si beam projected onto the surface. Also shown in Figure 4.1 is a reference measurement for a Ag ion exchanged sample that was irradiated with Si only; it does not show a plasmon absorption band and is colorless.

Plan-view TEM images are shown in Figure 4.2, taken under normal incidence. Figure 4.1(a) shows the Ag nanocrystals formed after 1 MeV Xe irradiation, with typical diameters in the range 215 nm, randomly

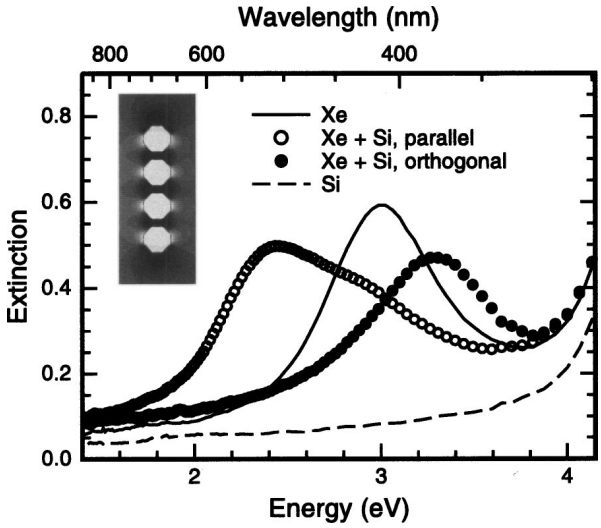

Figure 4.1: Optical extinction spectra of Ag ion exchanged BK7 glass samples irradiated with 1 MeV Xe (line) to form Ag nanocrystals, and with subsequent 30 MeV Si under an angle of 60° off-normal, using normal incidence light. The Si irradiation (2×10^{14}/cm^2) causes a large split in the plasmon bands for polarizations transverse (closed circles) and longitudinal (open) to the direction of the Si beam as projected onto the surface. The inset shows a representative time snapshot of the electric field distribution obtained from an FDTD simulation with enhanced field amplitude both inside (white, positive field) and between (black, negative field) the Ag particles.

distributed in the glass. Figure 4.2(b) shows data taken after Xe and Si irradiations: randomly oriented Ag nanocrystals are still observed, but in addition, arrays of aligned nanoparticles are found. These arrays are along the direction of the ion tracks (arrow). The redistribution of Ag is ascribed to the effect of the thermal spike caused by the 30 MeV ions, possibly in combination with anisotropic strain generated along the track [21]. The anisotropy is also observed in the spatial Fourier transform (inset) of Figure 4.2(b), in contrast to that of Figure 4.2(a). Note that no clear shape change of the nanoparticles is observed, as was seen for Au cores in silica colloids [118].

The splitting of the plasmon bands observed in Figure 4.1 can be explained by electromagnetic coupling among the aligned nanocrystals [112]. For polarizations parallel to the particle array, such coupling is known to result in a redshift. Conversely, transverse polarization will result in a blueshift. Finite difference time domain (FDTD) simulations of arrays similar to those observed in Figure 4.2(b) show that the splitting due to the coupling can be well over 1 eV. As an example, a representative time snapshot of the electric field amplitude distribution obtained from FDTD simulation of a four Ag nanoparticle array is shown as an inset

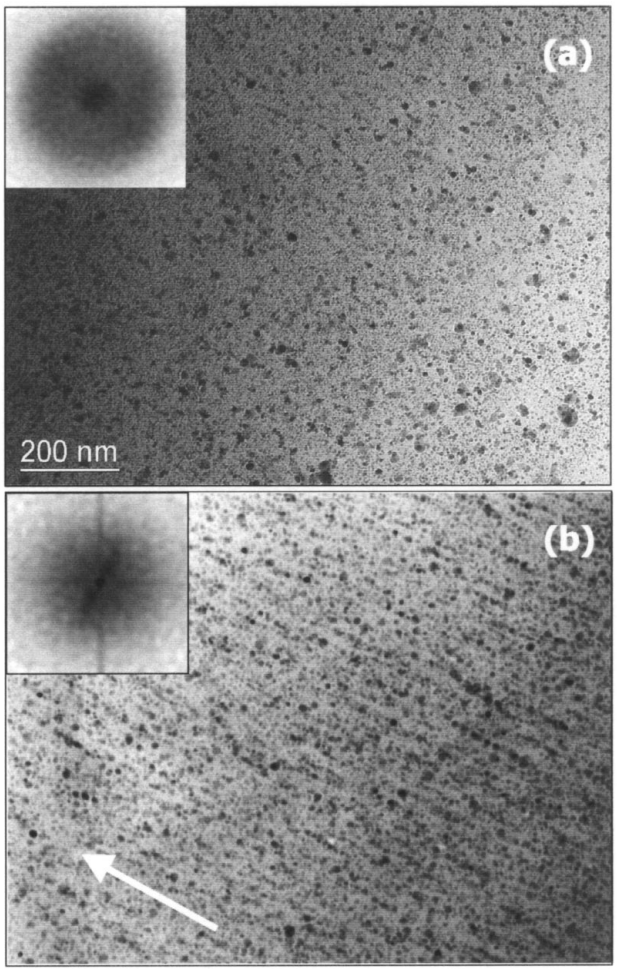

Figure 4.2: Plan-view TEM images of Ag ion exchanged BK7 glass after 1 MeV Xe **(a)**, and after subsequent 30 MeV Si irradiation **(b)**. Scales of (a) and (b) are identical. The ion beam was under 60° off-normal and its projection onto the surface is indicated by an arrow. Clear alignment of Ag nanocrystals is observed along the ion beam direction. The insets show the spatial Fourier transform of the images (full scale 0.3 nm^{-1})

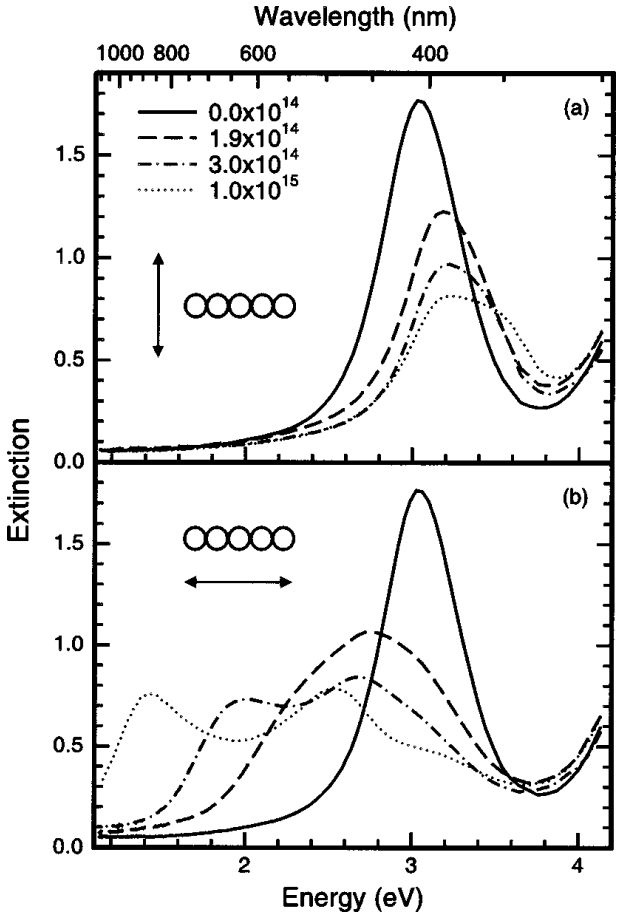

Figure 4.3: Optical extinction spectra for Ag ion exchanged and Xe irradiated BK7 glass irradiated with 30 MeV Si at various ion fluences up to 1×10^{15}/cm^2 (indicated in the figure). The polarization of the incoming light is transverse **(a)** or longitudinal **(b)** to the ion irradiation direction projected onto the surface. The splitting of the plasmon band can be tuned by changing the ion fluence and a shift well into the near-infrared is observed.

in Figure 4.1. The strongly enhanced field between adjacent particles is indicative of strong interparticle coupling. Details of the simulation with quantitative results are reported in [131], and in Chapter 5 of this thesis.

The plasmon band shift can be tuned by varying the Si ion fluence, as is illustrated in Figure 4.3. Here optical extinction spectra are shown for Si fluences up to 1×10^{15}/cm^2 (10 min/350 °C). With increasing Si fluence, the plasmon absorption band for the transverse polarization is blueshifted, as shown in Figure 4.3(a), whereas the plasmon absorption band for the longitudinal polarization is redshifted as in Figure 4.3(b). At a fluence of 1×10^{15}/cm^2, a redshift by as much as 1.5 eV is observed well into the near-infrared (870 nm).

Another feature to notice in Figure 4.3(b) is a second absorption band around 2.5 eV for high Si fluences. We attribute this to the formation and alignment of new Ag nanocrystals during the Si irradiation, and to the growth of existing nanocrystals. Note that after the original Xe irradiation, only 10% of the Ag ions are incorporated into nanocrystals, while 90% remain in solution. The slight difference in shape of the extinction spectra for Si fluences of $2\times10^{14}/\text{cm}^2$ in Figs. 4.1 and 4.3 is attributed to different ion exchange conditions for the two cases, resulting in different Ag depth profiles. A next challenge is to further increase the Si ion fluence and investigate if the plasmon resonance can be shifted further, into the important telecommunication bands around 1.3 and 1.5 μm.

4.4 Conclusion

We have shown that 30 MeV Si ion irradiation of BK7 glass containing Ag nanocrystals induces a partial redistribution of the nanocrystals into linear arrays along the ion tracks. The anisotropy causes a splitting in the optical extinction spectra, so that different surface plasmon resonance bands for longitudinal and transverse polarizations are observed. Resonance shifts as large as 1.5 eV are observed, well into the near-infrared and are in qualitative agreement with a model for near-field electromagnetic plasmon coupling.

Chapter 5

Highly Confined Electromagnetic Fields in Arrays of Strongly Coupled Silver Nanoparticles

Linear arrays of very small Ag nanoparticles (diameter ≈10 nm, spacing 0–4 nm) were fabricated in sodalime glass using an ion irradiation technique[1]. Optical extinction spectroscopy of the arrays reveals a large polarization-dependent splitting of the collective plasmon extinction band. Depending on the preparation condition, a redshift of the longitudinal resonance as large as 1.5 eV is observed. Simulations of the three-dimensional electromagnetic field evolution are used to determine the resonance energy of idealized nanoparticle arrays with different interparticle spacings and array lengths. Using these data, the experimentally observed redshift is attributed to collective plasmon coupling in touching particles and/or in long arrays of strongly coupled particles. The simulations also indicate that for closely coupled nanoparticles (1–2 nm spacing) the electromagnetic field is concentrated in nanoscale regions (10 dB radius: 3 nm) between the particles, with a 5000-fold local field intensity enhancement. In arrays of 1 nm spaced particles the dipolar particle interaction extends to over 10 particles, while for larger spacing the interaction length decreases. Spatial images of the local field distribution in 12-particle arrays of touching particles reveal both a particlelike coupled mode with a resonance at 1.8 eV and a wirelike mode at 0.4 eV.

[1] This chapter has been adapted from Sweatlock, Penninkhof et al., Reference [131].

5.1 Introduction

In recent years, significant progress has been made toward reducing the size of optical devices. This trend toward miniaturization is driven by the increase in system functionality and reduction in power dissipation that may be achieved when highly integrated photonic networks replace today's discrete devices and stand-alone modules. Another important motivation is a vision of an architecture in which photonic circuits integrate seamlessly into large-scale electronic systems. This requires waveguides that bridge the gap in size between conventional micron-scale integrated photonics and nanoscale electronics. Additionally, nanostructured materials often possess strong nonlinear properties that can be exploited in the development of novel active devices, since the confinement of light to small volumes can lead to nonlinear optical effects even with modest input power.

In purely dielectric materials, the optical diffraction limit places a lower bound on the transverse dimension of waveguide modes at about $\lambda_0/2n$, i.e., several hundreds of nanometers for visible light [33, 120]. Plasmonic waveguides, on the other hand, employ the localization of electromagnetic fields near metal surfaces to confine and guide light in regions much smaller than the free-space wavelength and can effectively overcome the diffraction limit.

In plasmonic systems there is generally a trade-off between the size of the electromagnetic mode and loss in the metallic structures. With this design principle in mind there are several choices for plasmonic waveguiding technologies which may prove useful for various applications. For example, thin metal stripes support long-range surface plasmon polaritons with an attenuation length as long as millimeters, but lack subwavelength mode confinement [9, 10, 25, 26, 94, 121]. Another geometry is metallic nanowires, which indeed can provide lateral confinement of the mode below the optical diffraction limit. Nanowires have larger attenuation than planar films, but light transport over a distance of several microns has been demonstrated [65]. Finally, metal nanoparticles are used to achieve three-dimensional (3D) subwavelength confinement of optical-frequency electromagnetic fields in resonant "particle plasmon" modes [14, 63, 89]. Nanoparticles provide highly enhanced local fields which are promising for molecular sensors [41, 43, 84, 143] or miniature nonlinear optical elements [42, 49, 51, 110, 124], and arrays of these particles can act as waveguides over modest distances [113]. Indeed, linear chains of metal nanoparticles have been shown to support coherent energy

propagation over a distance of hundreds of nanometers [82] with a group velocity around two-tenths the speed of light in vacuum [81]. The minimum length scales in fabricated structures are generally determined by the resolution of electron beam lithography, with particle diameters of $30 \times 30 \times 90$ nm^3 and interparticle spacings of 50 nm.

In this chapter, we investigate the mode confinement and plasmon coupling in nanostructures with even smaller length scales, composed of linear chain arrays of Ag nanoparticles with diameters in the 10 nm range and interparticle spacing as small as several nanometers. This work is inspired by our recent experimental results in which linear Ag nanoparticle chain arrays with such small length scales are formed in silica glass by ion irradiation [105]. Other methods for generating very small ordered metal structures include pulsed-laser irradiation [59] and biologically templated assembly [85].

We first present experimental optical extinction spectroscopy data that show evidence for strong plasmon coupling in ion-beam-synthesized Ag nanoparticle chain arrays. We compare experimental extinction data with full-field 3D electromagnetic simulations for arrays with various chain lengths and particle spacings. The simulations corroborate the experimental data and reveal large local-field enhancements in arrays of strongly coupled nanoparticles.

5.2 Nanoparticle Array Fabrication

Linear nanoparticle arrays in glass are formed by use of a high-energy ion irradiation technique as follows [105]. First, ionic Ag is introduced into sodalime silicate glass (BK7) by immersion in a melt of $AgNO_3$, 10% by mass, in $NaNO_3$ at 350 °C for 10 min. Silver displaces the constituent sodium via an ion exchange interaction, resulting in a Ag content of ≈ 6 at.% near the surface. Next the sample is irradiated with 1 MeV Xe ions to a fluence of 1×10^{16}cm^{-2} at normal incidence to induce the nucleation and growth of Ag nanoparticles. The typical particle diameter is in the range of 5–15 nm, and the particles preferentially form in an approximately 80 nm thick near-surface region of the silica glass [88]. Finally, the sample is irradiated with 30 MeV Si ions at an angle of 60° with respect to the surface normal while cryogenically cooled to 77 K.

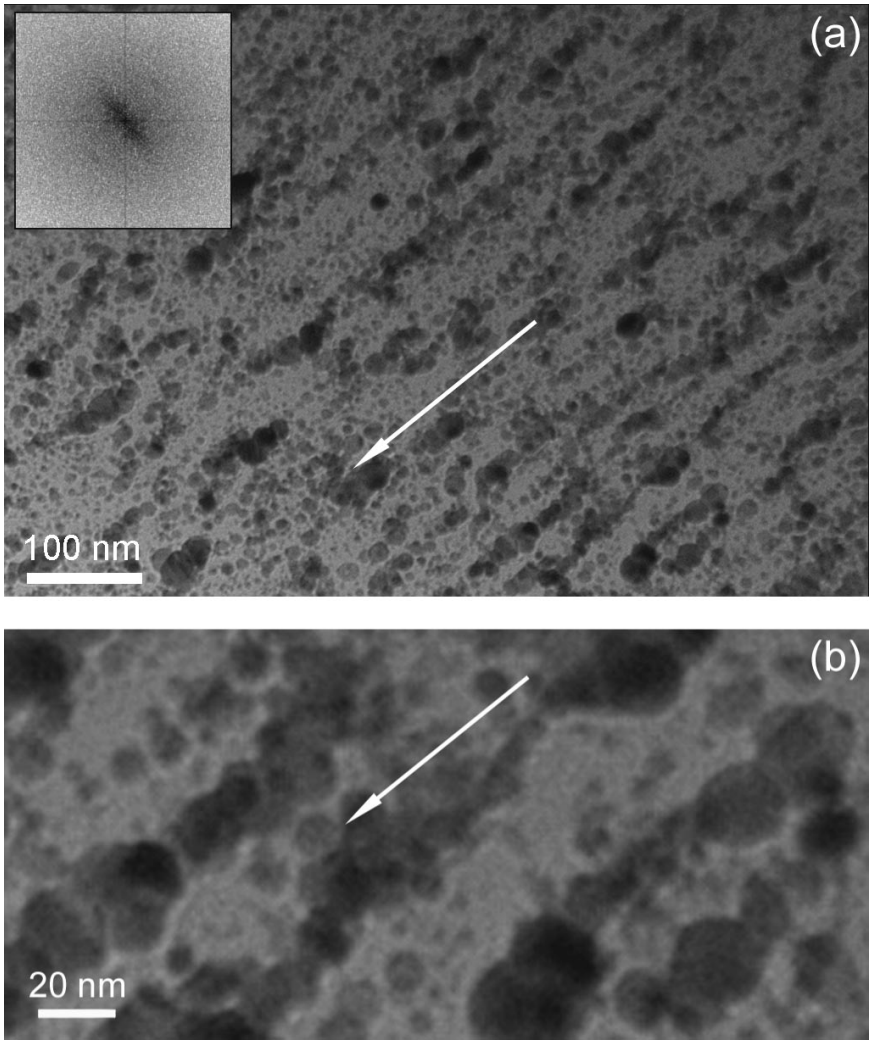

Figure 5.1: Plan-view TEM images of Ag nanoparticles in sodalime glass after 30 MeV Si ion irradiation at two different magnifications. Nanoparticle arrays are observed along the ion beam direction (indicated by arrows). The inset in (a) shows a spatial Fourier transform image of the micrograph confirming this anisotropy. The typical particle diameter in the micrographs is 10 nm, albeit with significant size polydispersity. Touching or closely spaced particles are observed, in arrays with a length of up to approximately 10 particles.

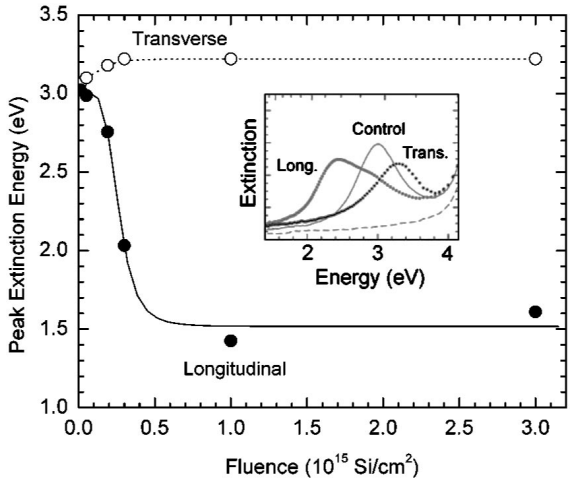

Figure 5.2: Measured optical extinction resonance peak energy for Ag nanoparticle arrays in glass as a function of 30 MeV Si fluence. Polarization of the incident light is transverse (open circles) or longitudinal (solid) to the projection of the ion beam into the normal plane. Inset: typical extinction spectra for both polarizations in a sample before irradiation "control" and after irradiation with 2×10^{14} cm^{-2} 30 MeV Si.

Figure 5.1 shows a plan-view transmission electron microscopy (TEM) image on a sample irradiated with 2×10^{14} Si cm^{-2}. A polydisperse Ag particle size distribution is found, with a typical diameter of 10 nm and an upper bound of about 20 nm diameter. The majority of Ag particles appear to have been incorporated into quasilinear chain arrays, aligned along the ion beam direction. This observation is confirmed by spatial fast Fourier transform of the image, inset in Figure 5.1(a). The redistribution of Ag is ascribed to the effect of the thermal spike caused by silicon ions' electronic energy loss [106]. Figure 5.1(b) shows a magnified view of the particle arrays. While in these plan-view images it is not possible to seperately identify individual arrays, as they overlap in the image, we estimate a typical array length of up to ten particles, with particles either touching or very closely spaced.

5.3 Optical Absorption Spectroscopy

The inset to Figure 5.2 shows optical extinction spectra taken under normal incidence of a sample before ("control") and after irradiation with 2×10^{14} cm^{-2} 30 MeV Si. Data were derived from optical transmission spectra measured using a spectroscopic ellipsometer with the incident beam perpendicular to the sample surface. The wavelength was scanned from 300 nm to 1100 nm in 5 nm steps. Before irradiation, an extinc-

tion peak is observed at an energy of 3.0 eV (freespace wavelength 410 nm), corresponding to the surface plasmon dipole excitation of isolated small Ag nanoparticles in a sodalime glass matrix with refractive index $n = 1.60$. After irradiation, two distinct spectra are observed for incident light polarized either parallel or perpendicular to the ion beam incidence direction projected into the sample surface plane. The splitting of plasmon extinction bands can be explained by "collective particle plasmon" resonances which result from electromagnetic coupling between neighboring particles in linear arrays [45, 112]. When incident light is polarized transverse to the array axis, repulsion between like surface charges on neighboring particles increases the energy required to drive a resonant oscillation and therefore results in a spectral blueshift. Conversely, attraction between nearby unlike surface charges under longitudinally polarized incident light will result in an extinction redshift.

The main panel of Figure 5.2 shows the peak energy of the transverse (open circles) and longitudinal (solid) mode extinction spectra as a function of Si ion fluence up to 3×10^{15} cm^{-2}. The transverse branch shows a modest blueshift that saturates at 3.2 eV (390 nm) while the longitudinal absorption peak can be tuned over a wide range, from 3.0 eV (410 nm) to 1.5 eV (830 nm), into the near infrared.

The longitudinal resonance redshift of over 1.5 eV is much greater than that previously recorded in chains of noble-metal particles with relatively large diameter and spacing, for which a redshift of 100 meV is observed [81, 82, 140]. The 1.5 eV shift is attributed to the very strong particle coupling in the present arrays. The ability to tune the resonance frequency into the near infrared is clearly valuable, as it potentially enables applications at important telecommunications wavelengths. Also, the strong interparticle coupling implies a large enhancement of electromagnetic fields [64] in the interparticle gaps, as will be discussed further on. In the context of nanoparticle waveguides, the extraordinarily large splitting of the plasmon bands indicates a large bandwidth and high group velocity for transport [18, 102]. However, very strongly coupled nanoparticles are suitable for waveguiding only over short distances, as significant spatial overlap of the mode with the metal particle leads to severe damping [80].

5.4 Finite Integration Simulation Proceedure

The influence of geometrical parameters on the collective plasmon resonance of linear chains of Ag nanospheres is studied by three-dimensional full-field electromagnetic simulations which employ finite element integration techniques to solve Maxwell's equations [48]. We keep the particle size constant at 10 nm diameter and assume that the particles are spaced evenly along a line with perfect axial symmetry. Particle spacing was varied from 0 nm (touching particles) to 4 nm. The optical constants of Ag are modeled with a Drude model:

$$\varepsilon(\omega) = 5.45 - 0.73\frac{\omega_p^2}{\omega^2 - i\omega\gamma}, \tag{5.1}$$

with ω_p =1.72×10^{16} rad s^{-1}and γ =8.35×10^{13} s^{-1}, which provides a good fit to tabulated experimental data [75] throughout the visible and infrared. The index of the surrounding glass matrix is set to n =1.60. The simulation volume is a rectangular solid which extends at least 100 nm beyond the nanoparticle surfaces in all directions. The mesh is linearly graded with a 10:1 ultimate ratio; i.e., if the grid cells in the immediate vicinity of the particles are 0.25 nm on each side, those on the outer boundary of the simulation volume are 2.5 nm on each side. Technical limitations constrain the mesh size under these conditions to about 2×10^6 total grid cells. In all simulations the incident light is polarized longitudinally relative to the array. We focus on the longitudinal plasmon resonance because the optical response has a strong functional dependence on geometrical parameters and because the extraordinary tunability of the longitudinal resonance may be of interest for a variety of applications.

A two-step process is used to find the collective particle plasmon resonant mode and its frequency for each array. First, the simulation volume is illuminated by a propagating plane wave with an off-resonance frequency that allows the particle chain to absorb energy. Second, the incident field is switched off and the electric field amplitude is observed in the time domain as any particle modes excited by the incident plane wave resonantly decay or "ringdown." The data presented below are all monitored at nanoparticle centers, but in general the time response of the electric field in interparticle gaps and other points of lower symmetry are also observed to provide additional information about the mode structure. A fast Fourier transform (FFT) of these data gives the spectral response that enables the resonant frequencies to be identified. Since the

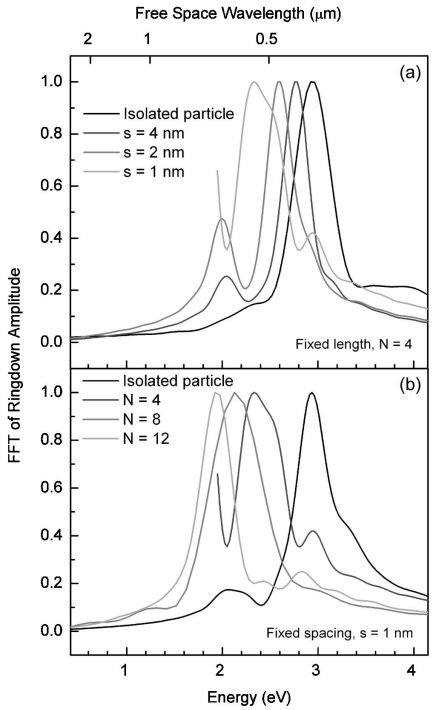

Figure 5.3: Simulated normalized longitudinal extinction spectra for linear arrays of 10 nm diameter Ag particles in glass. **(a)** Array of four particles spaced by 1, 2, or 4 nm. **(b)** Array of 4, 8, or 12 particles with interparticle spacing fixed at 1 nm.

absorption and ringdown are resonant phenomena, the frequency at which the peak FFT response occurs is directly comparable to the frequency of maximum extinction in an optical spectrum. Once the spectrum was outlined in this way, on-resonance excitation was used to excite individual modes to examine the corresponding spatial distribution of the field intensity. Such distributions can be used to discriminate between spectral features which correspond to the collective dipole excitation and other physical resonances or, in some cases, unphysical artifacts of the simulation or frequency domain transform which can be eliminated once identified. In some cases small "hot spots" were observed in the intensity maps, which occurred at slight faceted corners of the rendered nanospheres. By varying the grid size and geometry these were identified as artifacts of the simulation. When the grid cell linear dimensions were reduced to 0.25 nm in the immediate vicinity of the metal nanoparticles, these hot-spot artifacts had a negligible effect on the overall field distribution. This requisite fine mesh density has the indirect effect of constraining the maximum simulation size to linear arrays of about 12 nanoparticles.

Figure 5.3(a) shows peak-normalized Fourier transform amplitude spectra of particle ringdown for four-

particle chains of 10 nm diameter Ag particles, with interparticle spacings of 1 nm, 2 nm, and 4 nm, and for an isolated particle. We verified that the peak frequency value is robust against small changes to the mesh cell density, sphere smoothness, or other minor variations in simulation procedure. In contrast, the apparent linewidth and spectral shape of the resonance are not reliably determined, as they were found to be somewhat dependent on arbitrary factors such as the total ringdown time and the absorption cross section of the structure at the off-resonance excitation frequency. The Fourier transform spectra often also contain several peaks with normalized amplitude less than one. Investigation of spatial energy density profiles using selective-frequency excitation revealed that low-energy secondary peaks [e.g., around 2 eV in Figure 5.3(a)] correspond to artifact modes particular to the 3D polygonal representation of the nanoparticle. The weak features observed in the spectra of Figure 3 at energies slightly greater than that of the primary peak likely correspond to real multipolar nanoparticle resonances. Selective-frequency excitation simulation of these features proves intractable due to the low scattering strength of these resonances and spectral proximity to the primary peak. The primary peak, however, was found to correspond to the dipole excitation in all cases. From the above analysis we conclude that the peak energy of the Fourier transform spectra is a good metric for the dipole resonance energy and can thus be compared with experimental peak extinction energies.

5.5 Results and Discussion

The resonance peak for isolated particles in Figure 5.3(a) occurs at 2.93 eV (free-space wavelength 424 nm), in good agreement with the experimental data (Figure 5.2), indicating that the initially prepared Xe-irradiated sample without ordered nanoparticle arrays consists of essentially uncoupled nanoparticles. This is consistent with earlier work showing that under these Xe irradiation conditions about 33% of the incorporated Ag is agglomerated in nanoparticles with a mean diameter of 5–10 nm, while the remaining 67% remains embedded in the glass network as Ag ions. The corresponding interparticle distance is about three particle diameters, too large for significant interparticle coupling [88, 108].

Figure 5.3(a) also shows that a decrease in particle spacing in the four-particle array increases the interparticle coupling, leading to an increased resonance redshift. At 1 nm spacing the simulated resonance occurs

at 2.35 eV (528 nm). Figure 5.3(b) shows the effect of total chain length on simulated spectral response of Ag nanoparticle chains with the interparticle spacing fixed at 1 nm. Data are shown for arrays with a total length of 12, 8, 4, and 1 particle(s). As can be seen, increasing the chain length causes a larger shift towards lower frequencies, implying that the particle interaction extends beyond the first nearest neighbor. In the 12-particle chain the observed frequency is 1.92 eV (647 nm), a difference as large as 1.0 eV compared to the single-particle plasmon resonance. We expect that the effect of increasing chain length will saturate in chains of not more than 20 particles, based on Quinten and Kreibigs numerical calculations for Ag particles in air [112]. In less strongly coupled chains, with 2 nm or 4 nm spacing, we found that extending the overall length of the chain beyond four particles did not lead to a further shift in resonance frequency. This result is consistent with our earlier work [80], in which it was reported that in chains of widely spaced and therefore relatively weakly coupled Au particles, the resonance frequency was not a strong function of array length.

Figure 5.4 shows the spatial images of the peak instantaneous electric field intensity (i.e., E^2) at steady state for arrays of four 10 nm diameter particles, excited on resonace. Data are shown for interparticle spacings of (a) 4 nm, (b) 2 nm, or (c) 1 nm. The background level is normalized to the maximum instantaneous square amplitude of the incident plane wave. Note that this normalization level is different than the plane-wave background at the same instant in time as the field profile snapshot, since there is a phase lag between the amplitude peaks in the driving wave and in the resonant response. Each contour line represents an intensity difference by a factor $\sqrt[4]{10} = 1.8$ (four lines correspond to one order of magnitude). The maximum local field is observed in the dielectric gap between the two metal particles at the midpoint of the array. The factor by which the field intensity at the array midpoint exceeds the background level is approximately 80 in the weakly coupled array, Figure 5.4(a), and approximately 5000 in the more strongly coupled array (c). For comparison, the maximum field intensity enhancement near an isolated nanoparticle driven resonantly is typically 30. The giant 5000-fold intensity enhancement is consistent with previous reports of 10^6 to 10^8-fold enhancement of the effective Raman scattering cross section near metallic nanostructures, since Raman scattering is quadratic in field intensity [41, 143].

Figure 5.5 shows the field intensity along a line normal to the particle axis through the interparticle gap at the midpoint of a four-particle array. The field confinement is most pronounced for the array with the smallest

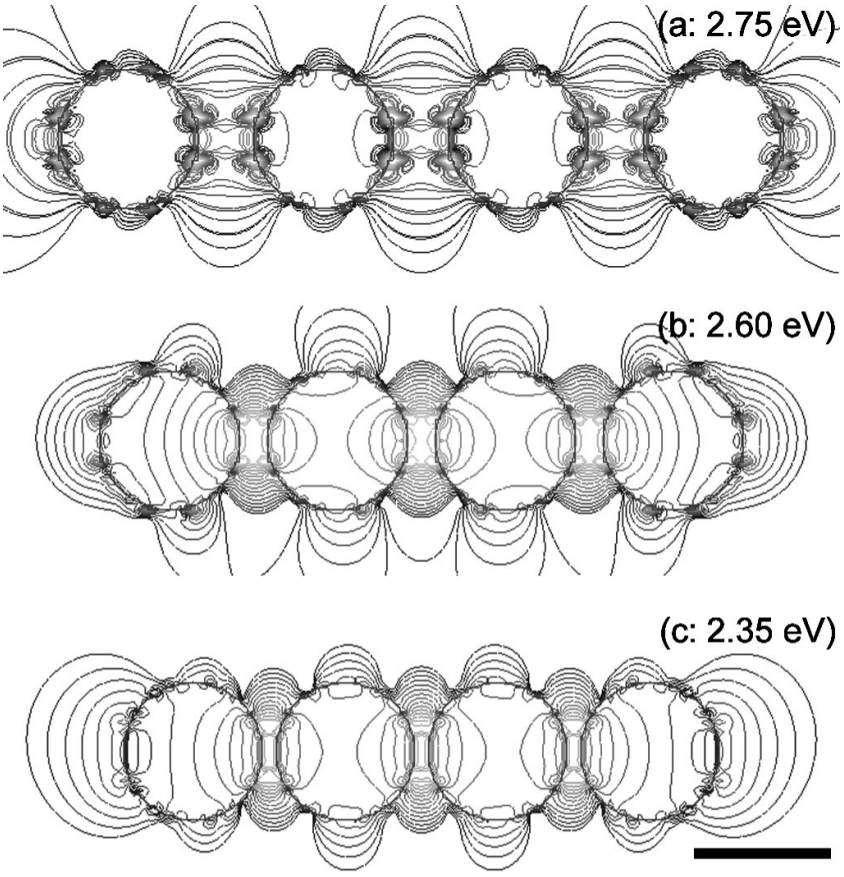

Figure 5.4: Two-dimensional spatial images of the simulated electric field intensity in a plane through the particle centers of four Ag nanoparticles with interparticle spacing of **(a)** 4 nm, **(b)** 2 nm, and **(c)** 1 nm at resonant excitation. The background is normalized to maximum instantaneous intensity of the incident plane wave. Each contour line represents an intensity difference by a factor of $\sqrt[4]{10} = 1.8$ (four lines represent one order of magnitude).

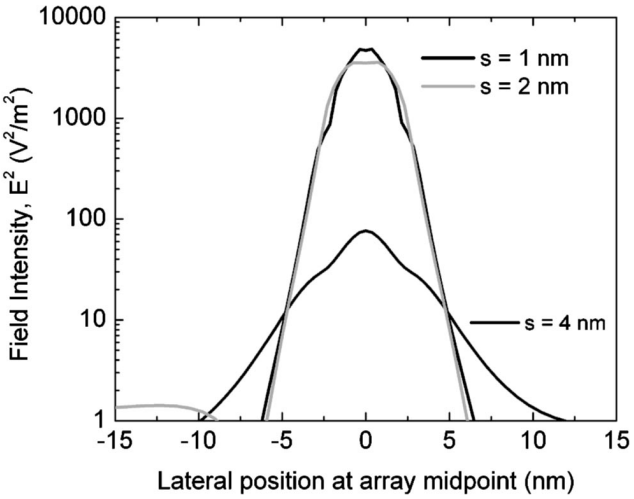

Figure 5.5: Electric field intensity on a line through the dielectric gap at the midpoint of an array of four Ag nanoparticles with interparticle spacing of (a) 4 nm, (b) 2 nm, and (c) 1 nm at resonant excitation. Maximum instantaneous intensity of the incident plane wave is 1 V^2 m^{-2}.

spacings, 1 nm and 2 nm, where the lateral distance (from the array axis) at which the field diminishes by 10 dB is 3 nm; it vanishes by 30 dB in less than 6 nm. Given that the resonant excitation wavelength for this mode in bulk glass is 330 nm, this clearly demonstrates the giant field enhancement and localization in these closely spaced nanoparticle arrays. Figure 5.5 also shows that for 4 nm spacing the field is less concentrated, with a 10 dB decay distance of 5.5 nm and peak field intensity nearly 100-fold lower than for the 1 nm spaced array. This demonstrates that true nanoscale engineering is required to take advantage of these high-field-concentration effects.

In TEM images such as Figure 5.1 we observe a strong possibility that in some arrays the interparticle separation has been reduced to the point that the nanoparticles just touch their neighbors. We refer to these arrays as having "0 nm interparticle spacing." In simulations the touching spheres are defined to overlap each other by about 0.25 nm (one grid cell depth) and therefore share a circular boundary surface with a radius of about 1 nm. In this case two distinct longitudinal modes are found in the spectrum. For an array length of 12 particles these occurred at 0.35 eV (free-space wavelength 3500 nm) and 1.65 eV (750 nm). As described in Sec. 5.4, we selectively excite and study the spatial distribution of the electric field for these two modes. In this case, the additional low-energy peak is not an edge or corner artifact but has real physical significance. This is demonstrated in Figure 5.6, which shows the longitudinal component (E_x) of the electric

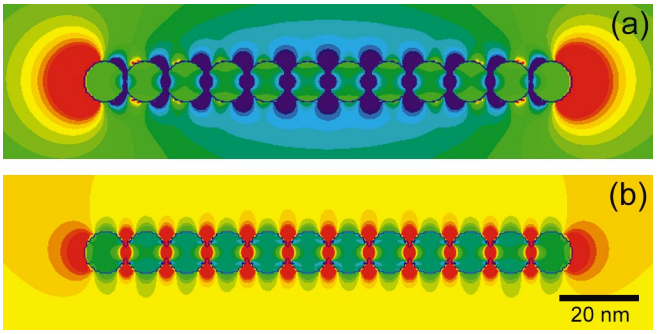

Figure 5.6: Distribution of the longitudinal component of the electric field (E_x) in the vicinity of an array of 12 Ag particles with 10 nm diameter, illustrating two distinct modes. In panel (a), an antenna-like mode resembling that of a single elongated wire is excited resonatly at 0.35 eV; in panel (b), a coupled-particle-like mode resembling that of a chain of independent particles is excited resonantly at 1.65 eV. The slight axial asymmetry of the field distribution is caused by superposition of the resonant mode with the exciting plane wave.

field in a system which consists of a linear array of 12 touching Ag spheres excited at the two resonance frequencies. Areas colored red have positive field amplitude, while areas colored blue have negative field amplitude. In a snapshot of the chain driven by a longitudinally polarized plane wave at 0.35 eV [panel 5.6(a)], regions of positive E_x are observed at either end, with negative E_x throughout the body of the array. This electric field pattern indicates that positive surface charge is concentrated on the rightmost particle and negative charge on the leftmost particle. The mode is typical of a single-wire antenna and requires surface charge to flow from particle to particle along the entire length of the array. Alternatively, when the same structure is driven at 1.65 eV (cf. Figure 5.6(b)) the coupled-dipole resonance is selectively excited. The field alternates from positive in each dielectric gap to negative inside each particle. This indicates an alternating surface-charge distribution in which each individual particle is polarized but electrically neutral. Thus, in the touching-particle configuration, the system can support two kinds of longitudinal resonance: the particles can act either as individual coupled dipoles or, instead, as a single continuous elongated "wire".

Although particle-like and wire-like modes of touching particle chains have strongly shifted peak resonance frequencies, we found that they do not in general exhibit an extremely high degree of local-field amplification. The lack of a dielectric gap means that the interparticle interaction is only weakly capacitive in nature, and therefore only a small magnitude of opposing surface charge builds up on neighboring particles. However, a contrary influence also comes into play. The sharp "crevice" formed between two

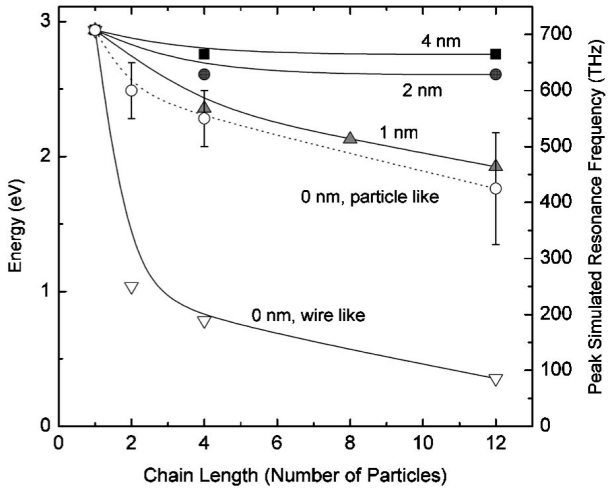

Figure 5.7: Simulated longitudinal collective resonance frequency for linear arrays of various overall length, ranging from 1 to 12 Ag particles each 10 nm in diameter. Series represent interparticle spacing from 0 to 4 nm. In the case of zero nanometer spacing, the frequencies of both coupled-nanoparticle-like and wire-like modes are plotted.

intersecting spheres may contribute to shape-induced enhancement to the local fields. For the specific geometric configuration and material properties input to our simulation, we found the former effect to dominate. Various aspects of coupled modes in nanoparticle dimers, including the touching-particle case, are discussed in References [4, 62, 95].

Figure 5.7 shows a compilation of longitudinal resonance energies for linear arrays of 10 nm diameter Ag particles, plotted as a function of chain length. The data series represent interparticle spacings of 4, 2, 1, or 0 nm. In the case of zero nanometer spacing, the energies of "particlelike" and "wirelike" modes are plotted separately. The particlelike resonances are relatively weak, leading to some uncertainty in their position, as indicated by error bars on that series. The figure shows that for 12 particle array length the resonance of the most strongly coupled arrays (0 or 1 nm spacing) shifts by about 1 eV to a peak resonance energy around 2 eV. More weakly coupled chains saturate at peak energies above 2.5 eV.

We now compare these data with the experimental particle distributions and resonance energy measurements in Figures 5.1 and 5.2. Indeed, touching and nearly touching particles are observed in the TEM, which according to our simulations lead to large plasmon shifts. The decrease in plasmon energy with increasing fluence (Figure 2) can be attributed to either a gradual growth in particle array length or a decrease in interparticle spacing, or a combination of both effects. The experimentally observed peak resonance for

high-fluence irradiation in Figure 5.2 is 1.5 eV. The resulting resonance energy is thus lower than the lowest coupled-particle mode energy calculated in Figure 5.7 (1.8 eV). This may indicate that long chains ($N > 12$ particles) form at large fluence. Alternatively, wirelike modes in small chains could be dominating as the interparticle spacing approaches zero. Further investigation of the relative interaction cross section for the wire and particle modes would be necessary to support this hypothesis.

For applications of field enhancements at the important telecommunication wavelength of 1.5 μm (0.8 eV), very strongly coupled arrays of nanoparticles are required. Comparing our data with our results from arrays of larger particles [81] and with previous results in the literature [112], it appears that it is the combination of particle center-to-center spacing and diameter, rather than interparticle spacing alone, that is a key parameter determining the coupling strength. Finally, we note possible applications of the wirelike mode in the THz-frequency domain, in particular for very long array lengths.

5.6 Conclusion

Linear arrays of very small Ag particles in glass, made using ion irradiation, show a strong anisotropy in optical extinction spectra, which is attributed to strong coupling between the particle plasmons. Full-field simulations of the electromagnetic field distribution on arrays of closely spaced Ag nanoparticle arrays show that coupling between the plasmonic particle modes leads to a reduction in the longitudinal resonance energy. In weakly coupled arrays, in which 10 nm particles are separated by 2 nm or 4 nm interparticle gaps, the resonance shift is less than 0.4 eV. For the "strongly coupled" case of 1 nm spacing or touching particles, a shift larger than 1.0 eV is observed. In those arrays the longitudinal plasmon resonance energy decreases with the total chain length up to at least ten particles. In particle arrays with 1 nm spacing, the simulations indicate a giant 5000-fold enhancement in field intensity between the particles. The resonant electric field is concentrated in extremely small regions with a radial dimension of 3 nm (radius defined at the 10 dB point). By comparing the simulated data with the experimental optical data it is concluded that plasmon coupling behavior in the experimental samples is dominated by short arrays of touching particles and/or long arrays of strongly coupled particles. Due to the great utility of wavelength tunability and local field enhancement

for applications such as nonlinear optics and sensing of small volumes, nanosized ordered or quasiordered ensembles of very closely spaced metal particles serve as an ideal platform for active device regions in integrated plasmonic networks. Innovative nanoscale engineering and fabrication are required to synthesize particle arrays with these interesting properties.

Chapter 6

Plasmon-Enhanced Photoluminescence of Silicon Quantum Dots: Simulation and Experiment

The enhancement of photoluminescence emission from silicon quantum dots in the near field of cylindrical silver particles has been calculated using finite integration techniques[1]. This computational method permitted a quantitative examination of the plasmon resonance frequencies and locally enhanced fields surrounding coupled arrays of silver particles having arbitrary shapes and finite sizes. We have studied Ag nanoparticles with diameters in the 50–300 nanometer range and array pitches in the range of 50–800 nm, near a plane of optical emitters spaced 10–40 nm from the arrays. The calculated and experimental plasmon resonance frequencies and luminescence enhancements are in good agreement. In the tens-of-nanometers size regime, for the geometries under investigation, two competing factors affect the photoluminescence enhancement; on one hand, larger field enhancements, which produce greater emission enhancements, exist around smaller silver particles. However, as the spacing of such particles is decreased to attain higher surface coverages, the interparticle coupling draws the enhanced field into the lateral gaps between particles and away from the emitters, leading to a decrease in the plasmonic emission enhancement. The computations have thus revealed the limitations of using arbitrarily dense arrays of plasmonic metal particles to enhance the emission from coplanar arrays of dipole-like emitters. For such a geometry, a maximum sixfold net emission enhancement is predicted for the situation in which the plasmonic layer is composed of 50 nm diameter Ag particles in an array having a 300 nm pitch.

[1]This chapter has been adapted from Biteen, Sweatlock, Mertens et al. Reference [13].

6.1 Introduction

Si quantum dots are of interest in potential applications ranging from biological sensing to light-emitting devices because the optoelectronic properties of zero-dimensional quantum dot silicon nanocrystals are different from the optical properties of bulk Si. In contrast to the very weak emission from bulk Si, silicon nanocrystals (nc-Si) having dimensions below ≈ 5 nm emit light efficiently and exhibit emission energies that can be tuned throughout the visible spectrum by varying the size of the nc-Si [20, 37, 90]. One important advantage of using light emitters based on silicon is that such systems can be fabricated with CMOS-compatible methods such as ion implantation.

The overall brightness of nc-Si is limited by the low emission decay rate, 10^4-10^5 s^{-1}, that results from the indirect band gap of silicon [20]. Plasmonic interactions, which exploit the intense local field near the surface of a metal particle or a rough metal surface, can modify the radiative decay rate and quantum efficiency and thus modify the photoluminescence (PL) intensity of an emitter [47, 69, 142]. The coupling of dyes and semiconductor quantum dots to the plasmon modes of silver and gold nanostructures has been shown to produce increased emission due to a plasmon-enhanced PL process [3, 67, 68, 125]. This approach has been extended to control the PL intensity, radiative rate, and optical polarization properties of nc-Si [12, 86], and the observed PL enhancement for nc-Si has been shown to arise from a resonant interaction [11]. Measurements to date of the plasmon-enhanced PL of nc-Si have, however, been performed via far-field ensemble measurement techniques that do not provide spatially resolved information on the origin of the enhancement [11, 12, 86]. Thus, in addition to near-field interactions, other processes could possibly contribute to the observed PL enhancement in this system. A theoretical approach is therefore needed to distinguish between these effects.

Previous theoretical treatments used analytical approximations to investigate the properties of plasmon-enhanced emission with electrodynamical theory that provides exact results for spherical particles [47, 69, 142]. These models have recently been improved to include radiation damping and dynamic depolarization [87]. While the latter model can be generalized for spheroids, it cannot treat metal nanoparticles of arbitrary shape, nor can it account for interparticle coupling. We are interested in quantitatively comparing calculated enhancements to experiments that involve arrays of nonspheroidal, coupled particles, and we

desire to avoid the approximations required to perform an analytical analysis of such a system. Computational approaches, such as T-matrix solutions [61], the discrete dipole approximation [52, 60, 146], and finite-difference time-domain simulations [48], have been utilized successfully in the past to examine the enhanced field about plasmonic metals. Given the lack of analytical models, we use a finite-element integration scheme of Maxwell's equations to calculate the resonance frequencies and mode intensity distributions for Ag particle arrays with arbitrary geometries in complex environments.

We have obtained quantitative information about the enhanced field experienced by silicon quantum dot emitters in the proximity of an array of lithographically defined silver particles. Full-field, finite-integration time-domain methods were used to simulate the frequency dependent nearfield and farfield optical properties of metal nanoparticle arrays. Specifically, the spectrum near the plasmon resonance has been simulated for planes of coupled, cylindrical np-Ag. Additionally, the enhancement of the local electric field intensity under the metal nanoparticle arrays has been calculated. The spatial distribution of nc-Si in the systems measured in Reference [11] have been taken into account in our comparison between the calculated results and the experimental measurements. We have also calculated the influence of the diameter and interparticle spacing of the Ag nanoparticles on the resonant frequency and electric field enhancements. In addition to verifying the physics that underlie the experimental observations [11], the electromagnetic simulations have been used to identify other, more optimal geometries that are predicted to exhibit larger field enhancements than the systems studied experimentally to date.

6.1.1 Field enhancements and spontaneous emission

A formalism for evaluating the decay rate of optical emitters in the near-field of a metal nanostructure has been developed by Gersten and Nitzan [47]. The formalism has been extended by Wokaun et al. to include fully radiationless energy-transfer quenching [142] and has been more recently restated by Kümmerlen et al. [69]. In the limit in which the calculated electric field distribution is dominated by dipole modes, the enhancement of the field intensity ($|E_{\mathrm{enh}}|^2/|E_0|^2$) is directly related to the photoluminescence radiative decay rate enhancement ($\Gamma_{\mathrm{rad,enh}}$), that is [69],

$$\Gamma_{\mathrm{rad,enh}}(\omega_{\mathrm{PL}}) = \Gamma_{\mathrm{rad,0}}|E_{\mathrm{enh}}(\omega_{\mathrm{PL}})|^2/|E_0(\omega_{\mathrm{PL}})|^2 \tag{6.1}$$

Computationally, the enhancement of the radiative decay rate of a dipole emitter in close proximity to a metal nanoparticle can be obtained by comparing the energy flux through a surface that encloses both the dipole source and the metal particle to the radiated power of the same dipole source in the metal of the particle [119]. Alternatively, by invoking the reciprocity theorem [53], radiative decay rate modifications can be obtained from the enhancement, at the position of the emitter, of the electric field intensity generated by plane wave illumination. In general, this procedure requires averaging over all angles of incidence. However, for a particle that is much smaller than the wavelength of light, the electric field intensity generated by plane wave illumination is independent of the angle of incidence and depends only on polarization [14]. Consequently, finite-difference time-domain (FDTD) simulations of the electric field intensity generated by plane wave illumination from one specific angle can be used to obtain maps of the radiative decay rate enhancement near a small metal nanostructure. We adopt such an approach in this chapter and justify the approach in the Results and Discussion section.

6.2 Experimental Section

Three-dimensional full-field electromagnetic simulations using finite-difference integration techniques were performed to solve Maxwell's equations [48]. This method allowed simulations to be performed on the exact shape of the metal cylinders that were fabricated lithographically, with no need to approximate the cylinders as oblate ellipsoids, as is commonly done to facilitate the use of analytical calculations. The simulations accounted for retardation, nonradiative damping by Ohmic loss, and interparticle coupling.

The experimental samples of Reference [11], to which the calculations were compared, consisted of 100 μm by 100 μm square arrays of cylindrical silver nanoparticles (np-Ag) that were 20 nm in height and had a range of diameters, d, between 135 and 320 nm. In the experiments, the nanoparticles were adhered, via a 2 nm thick amorphous Si wetting layer, onto the surface of a 3 mm thick substrate of fused silica doped with nc-Si at a depth of $\Delta \approx 10$ nm beneath the base of the np-Ag plane.

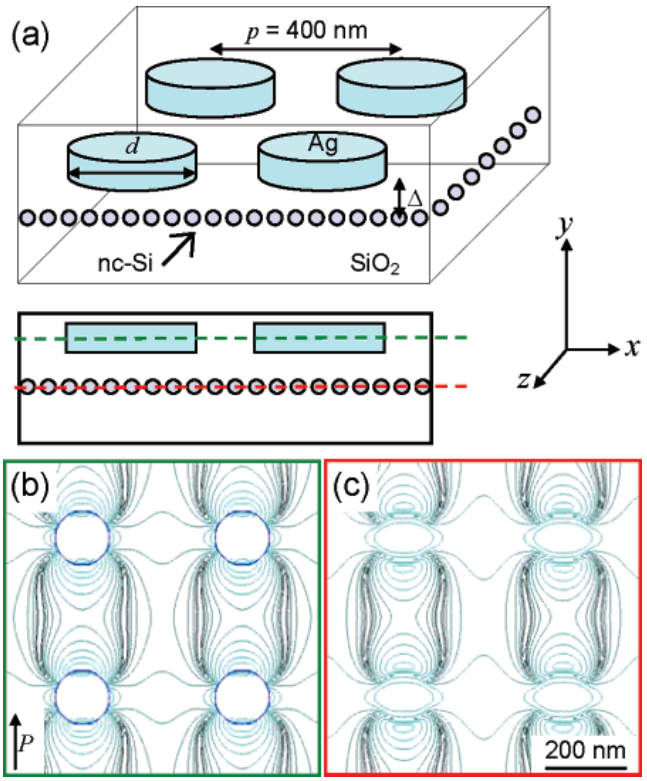

Figure 6.1: **(a)** Schematic of the simulated system showing a periodic array of Ag nanoparticles with pitch, p, and diameter, d, situated a distance, Δ, above a plane where Si quantum dots are located in the experimental configuration. Field intensity maps calculated for $d = 135$ nm, $p = 400$ nm, and $\lambda_{exc} = 633$ nm are plotted in the center plane of the np-Ag array **(b)** and in the plane 10 nm below the np-Ag **(c)**. Each four contour lines represent an order of magnitude in the x-component of the field intensity. The arrow, P, in (b) indicates the polarization direction of the incident plane wave.

Computations were conducted on a system (Figure 6.1a) that, given the restrictions of the simulation package [48], best emulated the experimental samples. The simulated np-Ag were cylinders 20 nm in height. The particle diameters in each array were chosen to correspond to those examined experimentally, based on scanning electron microscopy (SEM) data on the samples of interest [11]. A fixed pitch (particle center-to-center spacing) of $p = 400$ nm was considered in the simulations. The quasiinfinite arrays that were fabricated were simulated by using von Karman periodic boundary conditions to construct a two-dimensional infinite array of np-Ag. The simulation was performed over the volume of four particles that were arranged in a 300 nm deep, 800 nm by 800 nm box. This volume was divided into 2×10^5 grid cells that were refined to give the greatest detail in the area near the Ag particles. Simulations that have employed similar conditions have been shown previously to correspond well to experiments [131]. The dielectric function of Ag, ε_{Ag}, as a function of radial frequency, ω, was approximated using a modified Drude model that was fitted to tabulated data over the wavelength range of interest [75]

$$\varepsilon_{Ag}(\omega) = 5.45 - 0.73\frac{\omega_{b,Ag}^2}{\omega^2 - i\omega\gamma_{Ag}}, \tag{6.2}$$

where the bulk plasmon frequency is $\omega_{b,Ag} = 1.72\times10^{16}$ rad s^{-1}, and the plasmon decay rate is $\gamma_{Ag} = 8.35\times10^{13}$ rad s^{-1}. It was not possible to simulate an interface that laid along a periodic boundary [48]; therefore, the fused silica ($\varepsilon_{SiO_2} = 2.2$) under the nanoparticles and the air ($\varepsilon_{air} = 1$) around and above the nanoparticles were represented by a single effective medium that represented the distribution of the electric field above and below the plane of the silica-air interface. This approach was justified by iteratively solving for the distribution until a self-consistent solution was achieved. In this way, 70% of the field emanating from a resonant Ag nanoparticle was found to lie above the interface, and 30% was found to lie in the substrate. The effective medium was thus chosen to have a dielectric constant of $\varepsilon_{eff} = (0.3\varepsilon_{SiO_2} + 0.7\varepsilon_{air}) = 1.36$.

The spectral response of the np-Ag array was determined by illuminating the particle assemblies with a plane wave incident normal to the plane of particles (y-axis in Figure 6.1a). The wave was polarized in the plane of the array (along the x-axis), as indicated by the arrow, *P*, in Figure 6.1b. After 75 fs, the incident plane wave was interrupted, and the electric field distribution was allowed to relax. The ring-down of the field was recorded for 100 fs at specific locations in the array. The inset to Figure 6.2 presents a characteristic

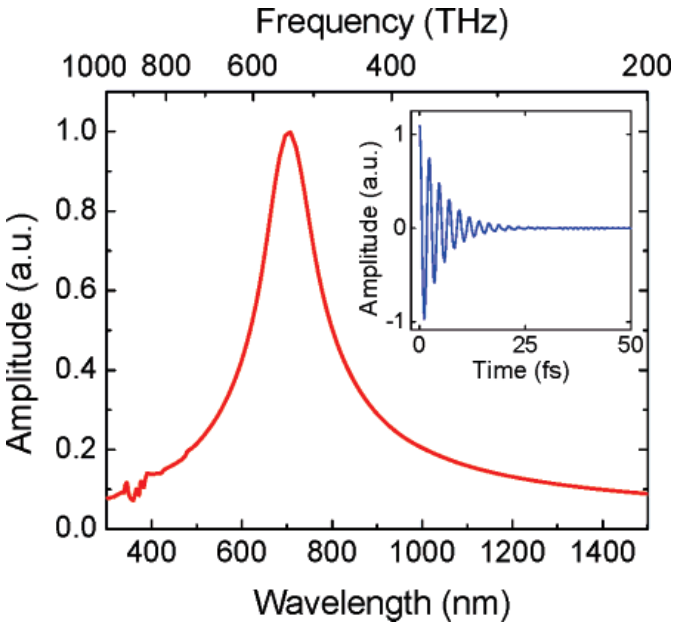

Figure 6.2: The np-Ag array collective plasmon resonance spectrum for a characteristic array ($d = 155$ nm, $p = 400$ nm), calculated via a Fourier transform of the electric field ring-down (shown in inset)

ring-down transient, taken at the center of a nanoparticle in a np-Ag array with $d = 155$ nm, for excitation on resonance at $\lambda = 705$ nm. Figure 6.2 presents a Fourier transform of this decaying field, which yielded the corresponding plasmon response spectrum, confirming the presence of a resonance peak at 705 nm. Note that although Fig. 6.2 was generated with resonant excitation in order to obtain a clean spectrum, the method does not generally require prior knowledge of the plasmon resonant spectrum. The initializing "impulse" field, due to abrupt truncation in the time domain has a very large effective bandwidth and therefore an essentially arbitrary center frequency can be used successfully.

Spatially resolved images of the electric field distribution around the particles were obtained by illuminating the particles at the resonant frequency determined for the corresponding array, using a plane wave normal to the sample, and allowing the array to store energy for 100 fs. The field distribution was then recorded in a plane 10 nm below the bottom of the np-Ag array, that is, where the emitters were located. This squared field amplitude was integrated over a full optical cycle to provide the time-averaged value of the local-field intensity, and this value was integrated over the plane of the nc-Si emitters to provide a comparison between the simulation output data and the experimental measurements.

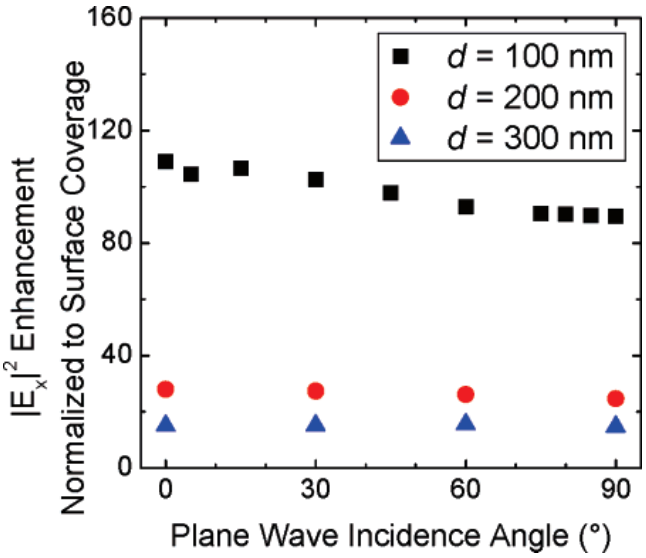

Figure 6.3: Computed field intensity enhancements in a plane 10 nm below the np-Ag array for different incident plane wave angles, θ, where the angle θ is measured from the particle plane. The pitch is 400 nm, and the np-Ag diameters are 100, 200, and 300 nm (squares, circles, and triangles, respectively).

6.3 Results and Discussion

To verify whether the 20 nm high cylindrical silver nanoparticles (np-Ag) having diameters of 50–300 nm were small enough to justify the reciprocal approach [53] described above, the electric field intensity enhancement was calculated in the nc-Si plane for a range of incident angles. Figure 6.3 shows the electric field intensity enhancement generated by plane wave illumination as a function of the angle of incidence relative to the z-axis (i.e., $\theta = 90^\circ$ for normal incidence) for three representative nanoparticle diameters (100, 200, and 300 nm) calculated at the plasmon resonance frequency for each sample. The incident plane wave is polarized in the x-direction (see Figure 6.1 for axis definition), and therefore, only the x-component of the electric field is considered. This is justified by the fact that, since we detect experimentally only light that propagates normal to the plane of the particles, the Si quantum dot emission of interest must originate from in-plane dipoles, which can only couple to the longitudinal modes of the metal nanoparticles. In Figure 6.3, the largest variation of field enhancement with angle is found for the largest particles, as expected. This variation of 15% thus provides an upper limit to the error in the simulation data shown hereafter. Since this error is small relative to the dynamic range of enhancements in field intensity studied herein, the electric field intensity enhancement, as calculated based on FDTD simulations at a single angle, is an appropriate measure

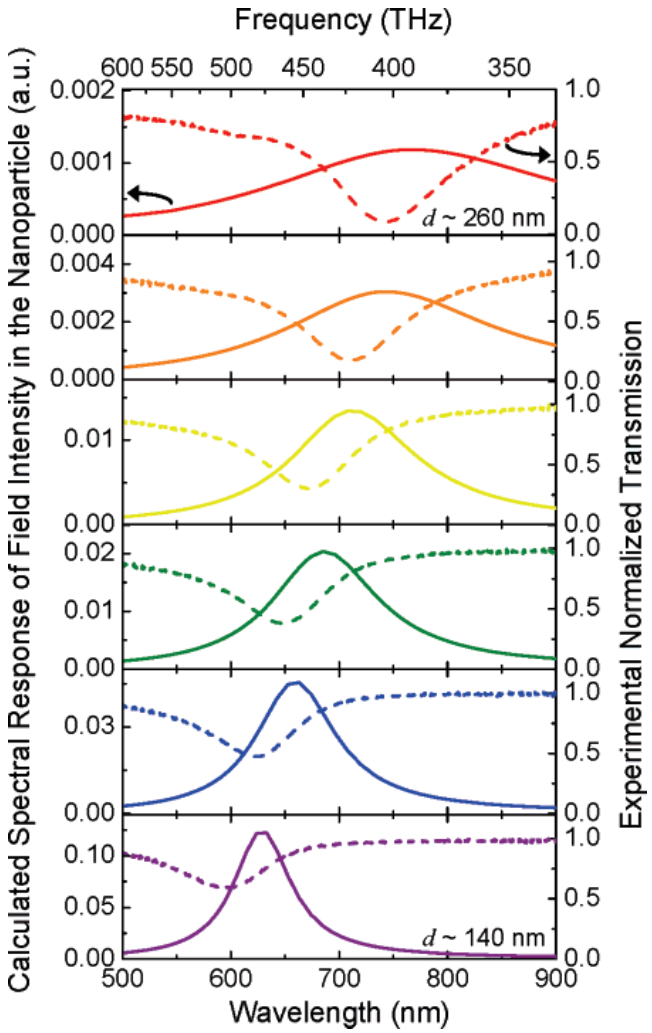

Figure 6.4: Calculated plasmon resonance spectra (solid lines) and one representative experimental transmission measurement (dashed) for np-Au arrays with $d = 260$, 230, 190, 185, 165, and 140 nm (from top to bottom)

for the radiative decay rate enhancement.

Figure 6.4 shows the computed plasmon resonance spectra (solid lines) recorded in the center of the metal nanoparticle, as obtained from simulations of arrays having $p = 400$ nm and $d = 260$, 230, 190, 185, 165, and 140 nm, from top to bottom, respectively. Also shown are the measured transmission spectra of representative experimental samples (dashed lines) having the same set of nanoparticle diameters. The calculations reveal a gradual red shift of the resonance spectrum for increasing particle diameter, as has been observed in the transmission spectra. The changes in resonance frequency are dominated by size (and aspect ratio) effects, and the red shift can thus be ascribed to the increased particle diameter, although a secondary contribution is

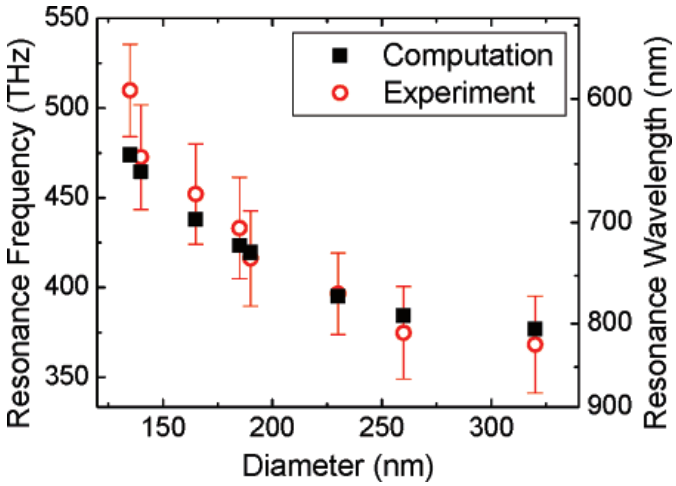

Figure 6.5: Comparison of resonance wavelengths derived from computation to those derived from an average over several (3 to 8) experimental transmission measurements

present from the increased interparticle coupling that occurs as particle diameters increase at a fixed pitch.

Calculations on isolated individual particles (rather than arrays), not shown here, yielded spectra that were blue-shifted by up to 100 nm compared to the spectra calculated for the nanoparticle arrays, verifying that the interaction between particles plays a role in determining the observed response of such arrays. Sample-to-sample variation causes subtle disagreements between experiment and theory for any single experimental sample. For instance, in Figure 6.4, the measured transmission peak is consistently blue-shifted relative to the calculated enhancement peak. However, when the transmission measurements are repeated on several experimental samples, these differences vanish, as illustrated in Figure 6.5. This figure shows the peak wavelength of the calculated resonance spectrum for $p = 400$ nm np-Ag arrays having particle diameters in the 135–320 nm range. Experimentally determined minima of transmission spectra are also shown (averaged over 3 to 8 samples for each value of d). Within the error bars, which arise from the sample-to-sample variations in experimental measurements, good agreement was observed between the experimental data and the simulations.

The electric field intensity throughout the three-dimensional space about each np-Ag array was also computed numerically. As an example, Figure 6.1b and c shows the field intensity/ amplitude distributions for an array having $d = 135$ nm excited at its computed resonance wavelength of 633 nm. The incident light was polarized in the x-direction. Figure 6.1b displays the electric field intensity at a cut along a plane through the

center of the Ag particles. Figure 6.1c shows a cut along the plane parallel to the np-Ag plane at a depth of 10 nm below the base of the nanoparticles, where the nc-Si emitters are located in the experimental samples. In these figures, four subsequent contour lines represent an order of magnitude change in the x-component of the field intensity.

In the experiments of Reference [11], the nc-Si were distributed uniformly across a plane. A measure of the field intensity experienced by an average emitter in this plane can be found by integrating the calculated electric field intensities over the area of the plane. For example, the average field intensity felt by a nc-Si emitter in the plane beneath an array of $d = 135$ nm np-Ag was found by integrating the field intensity plotted in Figure 6.1c over the area of that figure. This intensity was further normalized by the incident field and time-averaged over an optical cycle. According to Equation 6.1, this averaged computed field intensity enhancement should be directly reflected in a PL radiative rate enhancement. In the high pump flux regime in which the experiments were performed, the steady-state PL intensity is directly proportional to the radiative rate of the PL. A measured enhancement of the PL intensity therefore directly reflects an increase in the radiative decay rate, regardless of the existence of nonradiative decay paths. The measured PL intensity enhancement [11] should therefore be equal to the field intensity enhancement computed in the present work.

Figure 6.6a shows the computed time-averaged field intensity enhancement in the nc-Si plane for arrays having a fixed pitch of 400 nm, with particle diameters ranging from 20 to 320 nm (squares). Two trends are observed in the calculations. First, at small particle diameters, the average enhancement increased with increasing particle diameter. This effect can be ascribed to the increasing np-Ag surface coverage, which reflects the fraction of nc-Si emitters that coupled to the metal nanoparticles (in the limit of infinitesimal metal particle diameter, all nc-Si are uncoupled). The surface coverage effect is removed in Figure 6.6b, in which the computed and experimental field enhancements are normalized by the np-Ag surface coverage. These data therefore represent the local field enhancement under the nanoparticle. Second, above an optimum diameter of approximately 100 nm, the average enhancement decreases due to the decreasing local field in the nc-Si plane with increasing particle diameter. This behavior can be attributed to two important effects; (1) in the absence of coupling, the local field enhancement decreases with increasing diameter [141], and most importantly, (2) as the particles increase in size at a fixed pitch, the interparticle coupling increases,

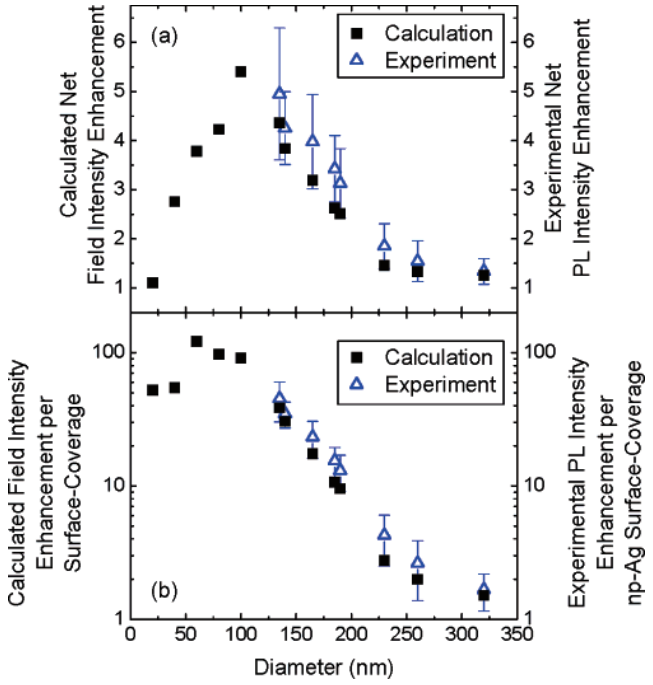

Figure 6.6: **(a)** Computed (squares) field intensity enhancement factors for arrays of np-Ag with various diameters and experimentally determined (triangles) photoluminescence (PL) enhancement factors. **(b)** Computed and experimental enhancements normalized by the np-Ag surface coverage.

and a proportionally larger part of the plasmon field lies in the lateral gap between the particles, resulting in a decreased field in the nc-Si plane. Though the present study is limited to examining arrays of np-Ag 20 nm in height, these principles hold true for all sizes and shapes of nanoparticles; the local field enhancement decreases about larger particles, and increased particle-particle coupling draws the field into the interparticle spaces.

Figure 6.6a also shows the experimentally determined enhancement of the PL intensity of the nc-Si emitters (triangles). Within the error bars, good agreement was observed between experiment and calculations. This agreement indicates that Equation 6.1 accurately describes the phenomenon of plasmon-enhanced photoluminescence in the particle size regime under investigation. The results depicted in Figure 6.6 also suggest that an optimum PL enhancement can be found by simultaneously optimizing the field enhancement and the density of the array. Optimization of the PL enhancement thus involves optimization of the metal particle diameter and the array pitch, keeping in mind that the array resonance frequency will shift with such geometrical changes.

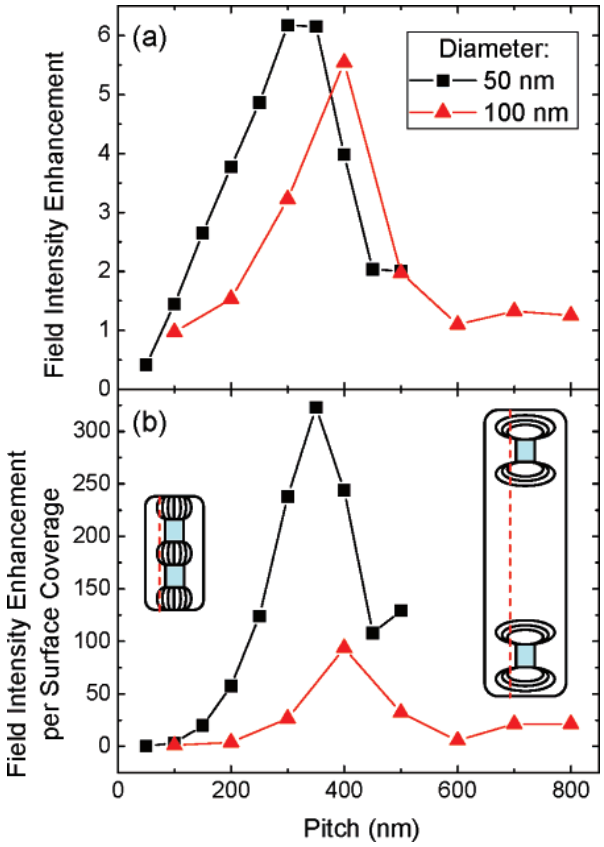

Figure 6.7: **(a)** Computed field intensity enhancement in the nc-Si plane for arrays of np-Ag with 50 nm (black squares) and 100 nm (red triangles) diameters and with varying pitches. **(b)** Computed field enhancements normalized by the np-Ag surface coverage. Inset: schematics illustrating the difference in field distributions between closely coupled particles (left) and distant weakly coupled particles (right)

A maximum field enhancement in the nc-Si plane cannot be straightforwardly attained by selecting an array with an arbitrarily high density of very small Ag nanoparticles. Figure 6.7a shows the field enhancement in the plane of the nc-Si at a depth of 10 nm beneath the bottom of an np-Ag array, for np-Ag arrays having $d = 50$ and 100 nm. The smallest pitches were 50 and 100 nm, respectively (i.e., touching cylinders), and the largest pitch was $p = 800$ nm. The results in this figure indicate that, despite the decreasing surface coverage upon increasing particle pitch, the field intensity enhancement in the nc-Si plane increases with increasing pitch until the pitch becomes much larger than the particle diameter. Figure 6.7b shows this same enhancement normalized for surface coverage. In the size regime considered herein, an increased pitch led to a decrease in the field intensity enhancement per particle as measured in the nc-Si plane, as schematically indicated in the insets to Figure 6.7. In these schematics, the blue rectangles represent np-Ag, the red dashed line is the nc-Si plane, and the black curves represent the region of enhanced field. Note that the greater interparticle coupling between very closely spaced (smaller pitch) np-Ag draws the enhanced field into the lateral gaps between Ag nanoparticles and out of the nc-Si plane that is 10 nm beneath the np-Ag plane. Similar effects are observed for the 50 and 100 nm diameter particles, with a smaller enhancement and a larger optimum pitch for the 100 nm diameter particles. The largest surface-average field enhancement in the present simulations is a factor 6 for 50 nm diameter particles with a 300–350 nm pitch. Perhaps surprisingly, the surface coverage for this geometry is only 6%.

Given the constraints of 20 nm thick cylindrical np-Ag particles arranged in a plane above a plane of emitters, further modifications within these constraints, such as replacing the circular np-Ag particles with squares or such as changing the array symmetry from a square to a hexagonal lattice arrangement (data not shown), were found computationally to have no significant effect on the field enhancement in the plane of the nc-Si emitters. The depth dependence of the field intensity under the arrays has also been evaluated through simulations. Figure 6.8 depicts the integrated field intensity as a function of depth for arrays having $p = 400$ nm and $d = 100$, 135, 185, and 320 nm. For all diameters, in the first 20 nm, the field intensity decreased rapidly with depth. The field enhancement was largest for the smallest particles and significantly enhanced field extend well beyond 40 nm for these smallest particles. For smaller distances ($\Delta < 5$ nm), quenching to the metal became dominant, and field enhancement calculations alone were not sufficient to determine the

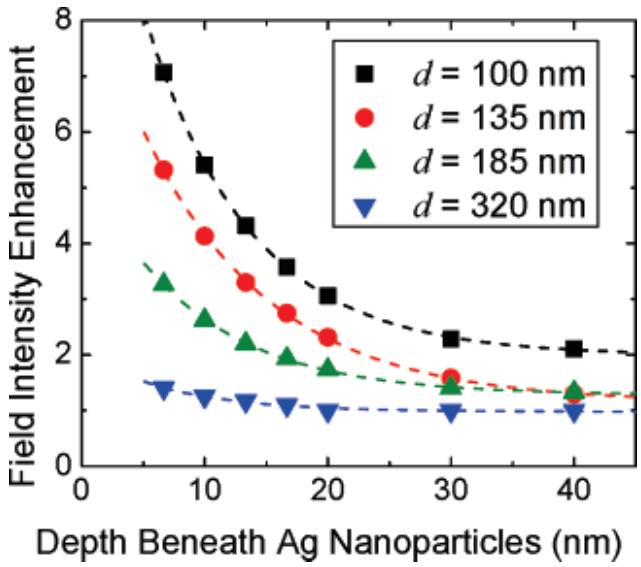

Figure 6.8: In-plane field intensity enhancement as a function of depth from the base of the np-Ag array for various np-Ag diameter, d

PL enhancement.

Simulations of this type can clearly be used to design future experiments and to predict the resonance frequency of a nanoparticle array *a priori*. This parameter could be important when coupling metals to emitters having sharp emission spectra, such as dyes and direct-band-gap semiconductor materials. In such situations, resonant coupling could only occur if the metal array was carefully designed to have a plasmon resonance spectrum that overlapped the precise emission spectrum. The simulations also provide beneficial three-dimensional maps which suggest the ideal placement of emitters near metals in different arrangements than that of the coplanar geometry considered in this chapter. The numerical studies described herein provide information about the far-field emission enhancement that results from near-field interactions. However, the results also provide insight into the local-field intensity as a function of position on a scale smaller than that which can be measured with far-field optics.

6.4 Conclusions

Electromagnetic simulations of the resonance spectra and field intensity distributions around Ag nanoparticles were performed with the aim to study plasmon-enhanced luminescence near arrays of these particles.

The simulations focused on determining the field enhancement in a plane at a fixed depth of 10 nm below the metal nanoparticles in order to enable comparison with experiments. Simulations showed a red shift of the plasmon resonance from 600 to 800 nm for particle sizes increasing from 140 to 340 nm, in good agreement with experiments. For a typical array pitch of 400 nm, simulations showed that interparticle coupling red shifted the resonance frequencies. In the 150 to 300 nm particle diameter range, experimental and calculated luminescence enhancements were in good agreement. The largest field enhancements were found for particles with diameters of 50 nm. At small interparticle spacing, a significant fraction of the field is drawn into the space between the metal particles. As a result, the largest surface-averaged field enhancement was observed for 50 nm diameter particles at a pitch of 300–350 nm, that is, a surface coverage of only 6%. The calculations provide fundamental insights into the factors that determine plasmon-enhanced emission in coupled nanoparticle arrays and can be used to study a wide range of alternative geometries.

Chapter 7

Plasmonic Modes of Annular Nanoresonators Imaged by Spectrally Resolved Cathodoluminescence

7.1 Introduction

In this chapter, we report the observation of plasmonic modes of annular resonators in nanofabricated Ag and Au surfaces that are imaged by spectrally resolved cathodoluminescence[1]. A highly focused 30 keV electron beam is used to excite localized surface plasmons that couple to collective resonant modes of the nanoresonators. We demonstrate unprecedented resolution of plasmonic mode excitation and by combining these observations with full-field simulations find that cathodoluminescence in plasmonic nanostructures is most efficiently excited at positions corresponding to antinodes in the modal electric field intensity.

7.2 Results

Excitation and localization of surface plasmon polariton (SPP) modes in metallodielectric structures is currently a topic of intensive research motivated by the ability to achieve truly nanophotonic materials and devices with tunable optical dispersion [6]. In particular, nanoresonators are essential building blocks of future subwavelength-scale photonic systems as both active [8] and passive [17] device components. Nanostructures consisting of annular grooves and gratings in metal films exhibit exciting properties such as photon-

[1] This chapter has been adapted from Hofmann et al., Reference [55].

to-plasmon coupling [71], focusing [73, 74, 128], and intensity enhancement [24, 73, 128], all of which are exciting for sensing [56] and surface-enhanced Raman scattering applications [93, 98]. In this chapter, we directly excite plasmonic modes in engineered annular nanoresonators on Ag and Au surfaces with a highly localized electron beam source, and use spectrally resolved cathodoluminescence imaging [40] to probe the plasmon field intensity as a function of excitation position.

Surface plasmon polaritons are generally excited optically at a metal/dielectric interface using a prism or grating to couple the incident light to the surface wave [114]. Previously, annular gratings have been investigated with near-field optical techniques capable of 20 nm optical probe sizes [74, 128]. Alternatively, a focused electron beam can be used to directly and locally excite SPPs with higher spatial resolution, without the intermediate step of generating and coupling an incident photon. Electron energy loss spectroscopy in the transmission electron microscope (TEM) has been used to visualize plasmonic modes in metal nanoparticles [144, 145], nanorods [15, 145], and nanotriangles [92] with spatial resolution limited only by the electron beam diameter, which can be as small as 1 nm. Such investigations in the TEM require samples to be electron transparent, for example, to have thicknesses less than 100 nm. However, cathodoluminescence (CL) excitation in the scanning electron microscope (SEM) does not impose such a constraint on sample thickness. In the SEM, electron beam excitation yields CL emission that has recently been used to investigate the propagation of SPPs along planar metal surfaces and linear gratings [7, 136] and to image modes in Au nanowires [138]. We extend this technique to investigate modes in nanofabricated plasmonic annular nanoresonators. When a metallic nanoresonator is excited with an electron beam, there are several phenomena that can result in light emission. High-energy electrons can directly excite d-band transitions in the metal film, producing photons with energies of approximately 4 eV (310 nm) upon relaxation in Ag [39, 133]. The incident beam can also excite localized surface plasmons (SPs) and propagating SPPs. In the annular nanoresonator structures described here, the SPs can couple to resonant plasmonic modes. We show that such resonant modes are most efficiently excited by focusing the localized electron beam at positions corresponding to antinodes in the modal electric field intensity.

Nanoresonators were fabricated on Ag and Au surfaces. The Ag structures were prepared by evaporating 400 nm of Ag on a quartz substrate and using focused ion beam (FIB) nanofabrication with a Ga^+ ion

source operating at 30 keV. Each annular resonator is composed of a center plateau and five concentric rings separated by grooves 50 nm deep with varying grating ring period and center diameter. Nanoresonators with 15 concentric grooves 100 nm deep were also patterned in the (111) surface of a polished single-crystal Au substrate grown by the Czochralski process.

Spectrally resolved CL analysis was performed using a field emission SEM operating at 30 keV and equipped with a mirror-based cathodoluminescence detection system [40]. For this technique, the spatial resolution in excitation is limited only by the electron beam spot size of 5 nm. Monte Carlo simulations [34] of electron trajectories in a 400 nm thick Ag film on quartz confirm that no significant beam broadening occurs within 20 nm of the Ag surface, one electric field skin depth [31]. Furthermore, although the electron trajectories extend beyond 4 μm into the substrate, any luminescence excited below several skin depths in the Ag film is significantly attenuated before emission and detection are possible. Thus, any detected light arises only from interactions near the surface of the Ag film.

Light emitted from the sample is collected with a retractable paraboloidal mirror positioned above the sample (collection angle up to (80 from the surface normal). For spectroscopy and spectrally resolved CL imaging of the Ag sample, emitted light is sent through a grating monochromator before being focused on the photomultiplier tube detector. For panchromatic imaging, the light emitted from the sample is focused directly onto the photomultiplier detector, detecting photons with wavelengths ranging from 300 to 900 nm. Spectrally resolved CL images are obtained by setting the grating monochromator to a specific wavelength and scanning the electron beam over a selected area of the sample with a per pixel dwell time of 10 ms and a passband of 27 nm. Secondary electron and CL images are obtained simultaneously. The images were postprocessed to correct for the drift in the scan direction by shifting each row of pixels of the SEM image to recreate the true annular resonator topography, and applying this same correction to the corresponding CL image. Any drift in the vertical direction is not corrected, explaining the elongated center region in several of the images. The single-crystal Au sample was imaged using spectral detection on a charge-coupled device array detector, sampling wavelengths from 387 to 947 nm. Spectrally resolved images are obtained by taking slices through the compiled image with 20 nm spectral resolution.

Two different simulation methods are employed to investigate the plasmonic modes of annular nanores-

onators. First, we perform three-dimensional full-field electromagnetic simulations which solve Maxwells equations using finite-element integration (FEI) methods [48]. We assume that the optical constants of Ag are described by the Drude model

$$\varepsilon(\omega) = \varepsilon_h - \frac{(\varepsilon_s - \varepsilon_h)\omega_p^2}{\omega^2 + i\omega v_c}$$

with relative permittivity in the static limit $\varepsilon_s = 6.18$, relative permittivity in the high-frequency limit $\varepsilon_h = 5.45$, plasma frequency $\omega_p = 1.72 \times 10^{16}$ rad/s, and the collision frequency $\omega_c = 8.35 \times 10^{13}$ rad/s. We simulate a structure with 600 nm center diameter and 300 nm grating period using a cylindrical slab of Ag (400 nm thick, 4 μm diameter) containing annular grooves (50 nm deep, 150 nm wide, spaced 150 nm apart) all enclosed in a matrix of air. In these finite difference time domain (FDTD) simulations, a propagating plane wave incident normal to the Ag surface is used as the source, polarized along an arbitrary direction in the plane of the surface. A two-step process is used to identify the resonant modes and their corresponding frequencies [131]. The structure is first excited nonresonantly with a low-energy plane wave. The excitation is then turned off, and the induced electric fields decay, or ring down, allowing the resonator to select its natural frequencies in the absence of an external driving field. This method of illumination effectively contains a wide spectral intensity that is peaked around the frequency of the initial plane wave. A fast Fourier transform (FFT) of the time domain ringdown data reveals the frequency response. Spectrally resolved cathodoluminescence imaging is not a time-resolved technique, and a valid comparison between experimental results and simulations must include observables that are averaged over at least one optical cycle. The time-averaged electric field intensity was determined by squaring the magnitude of 25 three-dimensional electric field snapshots from a single time period at the end of the simulation and averaging the result. Resonator modes with symmetries that are not supported by normal-incidence excitation were investigated with off-axis plane waves. The incident angle was chosen to impose the correct symmetry upon the center region of the nanoresonator.

Boundary element method (BEM) simulations [27, 28] allow us to calculate the probability of cathodoluminescence emission for various positions in the annular nanoresonators. Computations are performed in the frequency domain, where the electromagnetic field within each homogeneous region of space is expressed

in terms of auxiliary boundary charges and currents. The customary boundary conditions are used to obtain a set of surface-integral equations involving those boundary sources, which are solved using linear-algebra techniques upon discretization of the boundaries via a set of representative surface points. Furthermore, the axial symmetry of the annular resonators is used to decompose the fields in uncoupled azimuthal components m with azimuthal angle dependance as $e^{im\phi}$. This results effectively in a one-dimensional field calculation problem that is solved with great accuracy. Converged results for a nanoresonator of 600 nm center diameter and 300 nm period have been achieved using $\sim$ 1000 discretization points. Calculated CL intensities are obtained using as an external source the field of a 30 keV electron, which is separated analytically in frequency components. The integral of the time-averaged Poynting vector over emission directions in the far field for each frequency component yields the CL intensity at that particular photon frequency. Tabulated optical data have been used as input for the dielectric function [58].

Figure 7.1(a)-(c) shows panchromatic CL images of nanoresonators in Ag with 315 nm grating period and three different center diameters. The CL images represent the radiation collected from the entire resonator as a function of the electron beam excitation position on the structure. Bright regions in the images correspond to greater emitted photon intensity. For all annular nanoresonators shown here, we see high intensity for excitation at the edges of the center as well as the concentric rings. The locally increased emission inside the grooves is attributed to scattering from roughness in the polycrystalline Ag film, formed because of the crystal orientation-dependent focused ion beam milling rate. The intensity line profiles in Figure 7.1(e) correspond to the dashed lines through the panchromatic CL image in Figure 7.1(c) and the correlated SEM image in Figure 7.1(d). The CL profile clearly shows peaks in emission when the electron beam dwells near an edge. An overall decay in emission intensity is observed as the electron beam moves outward from the center. Thus, we see that a higher emitted photon intensity is obtained for electron beam excitation in the center of the structure, indicating that more efficient excitation and/or more efficient outcoupling occurs in this region.

Full-field FEI simulations are used to determine the plasmonic modes of an Ag annular nanoresonator with 600 nm center diameter and 300 nm grating ring period. We adopt a naming convention for the modes $\mathrm{M}_{s,n}$, where the integer s refers to the symmetry of the mode ($s = 0$ for modes with nodes in electric field intensity in the center, and $s = 1$ for modes with intensity antinodes in the center) and the integer n denotes

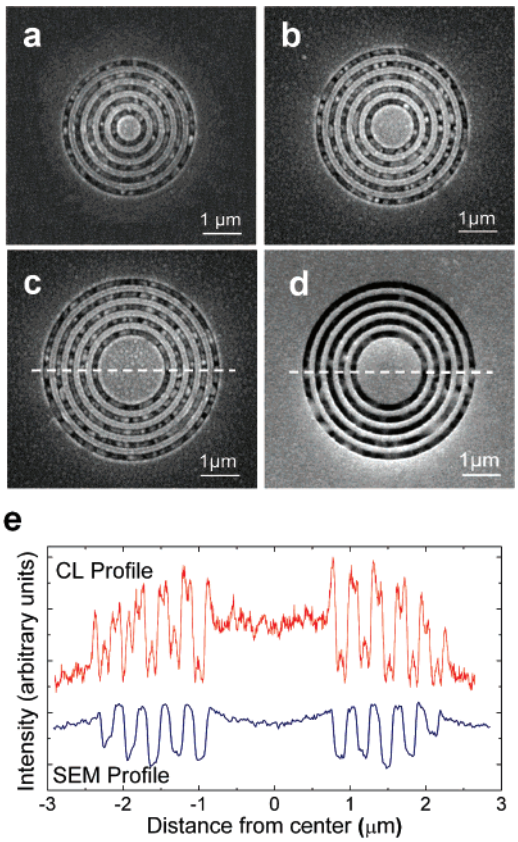

Figure 7.1: Panchromatic CL imaging of Ag annular nanoresonators with 315 nm period and center sizes of **(a)** 620 nm, **(b)** 1.07 μm, **(c)** 1.70 μm. **(d)** SEM image taken concurrently with panchromatic CL image of structure in (c). **(e)** Line profiles from regions indicated by the dashed line in (c) and (d) illustrating strong emission when the electron beam is positioned at an edge and decreasing intensity as the beam moves outward from the center

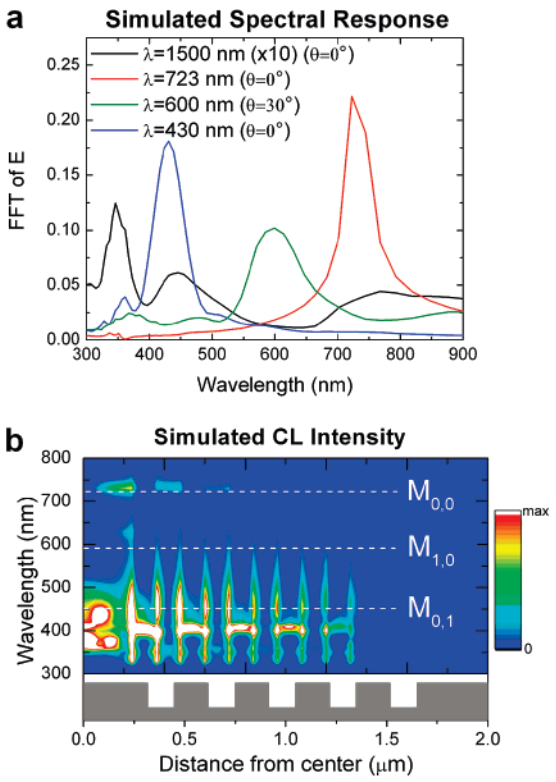

Figure 7.2: Simulated modes in Ag annular nanoresonator with 300 nm grating period and 600 nm center diameter. **(a)** Simulated spectral response for normal-incidence plane wave excitation at $\lambda = 1500$ nm, $\lambda = 723$ nm and $\lambda = 430$ nm and off-normal ($\theta = 30^\circ$) plane wave excitation at $\lambda = 600$nm. Peaks in the FFT spectra identify resonant modes of the structure. **(b)** Boundary element method simulations of plasmonic modes. Probability of cathodoluminescence emission is plotted as a function of excitation wavelength and position at a distance of 10 nm above the Ag topmost surface. Modes $M_{0,0}$, $M_{1,0}$, and $M_{0,1}$ are indicated at wavelengths of $\lambda = 720$ nm, $\lambda = 590$ nm, and $\lambda = 450$ nm, respectively. The surface topography is shown in gray.

the number of intensity antinodes in the radial direction of the center plateau, extending outward from the center of the structure and excluding peaks at the edges. The FFT spectra for low-energy normal incidence plane-wave excitation at $\lambda = 1500$ nm in Figure 7.2(a) show multiple features, including a peak at $\lambda = 330$ nm corresponding to the Ag surface plasmon resonance [31] and two broad peaks: one centered at $\lambda = 430$ nm and one in the 700–900 nm range. Subsequent excitation in each of these two bands at $\lambda = 723$ nm (mode $M_{0,0}$) and $\lambda = 430$ nm (mode $M_{0,1}$) leads to strong resonant response that we therefore attribute to plasmonic modes of the nanoresonator. Off-axis plane wave excitation enables investigation of an additional spectral peak centered at $\lambda = 600$ nm (mode $M_{1,0}$). Symmetry forbids excitation of this mode at normal incidence in our simulation, but off-normal incidence plane wave excitation breaks this symmetry constraint, and an antinode in electric field intensity is observed at the center. Characterizing the quality of these plasmonic nanoresonators is essential for development of future devices. We determine the quality factor [120], Q, of the nanoresonator for each mode from the exponential decay time of the electric field intensity during ringdown, giving $Q_{0,0} = 36$, $Q_{1,0} = 18$, and $Q_{0,1} = 8$.

Using BEM simulations, we calculate the probability of cathodoluminescence emission as a function of electron beam position for this same structure. Figure 7.2(b) shows CL intensity as a function of both distance from the annular nanoresonator center and wavelength of emitted light. The CL probability is calculated by integrating the emission for directions from the grating normal up to 30° from the normal. At $\lambda = 720$ nm, bright CL intensity is concentrated only at the edge of the center plateau, characteristic of $M_{0,0}$. Mode $M_{1,0}$ is observed at $\lambda = 590$ nm, characterized by a small peak in emitted intensity at the center of the structure. At $\lambda = 450$ nm, a node in CL intensity in the center of the structure and one antinode along the radial direction distinguishes $M_{0,1}$. For this mode, bright CL emission is also localized at the edges of the center and concentric rings.

Spectrally resolved CL imaging was used to experimentally reveal the plasmonic modes discussed above. Figure 7.3 shows SEM and spectrally resolved CL images of an annular resonator with a 620 nm center diameter and 315 nm grating period. At $\lambda = 350$ nm, which is very close to the Ag surface plasmon resonance, nearly uniform emission occurs for excitation anywhere in the structure. Near resonance, surface plasmon propagation lengths are very short and thus no resonator modes can build up. Several different modes are

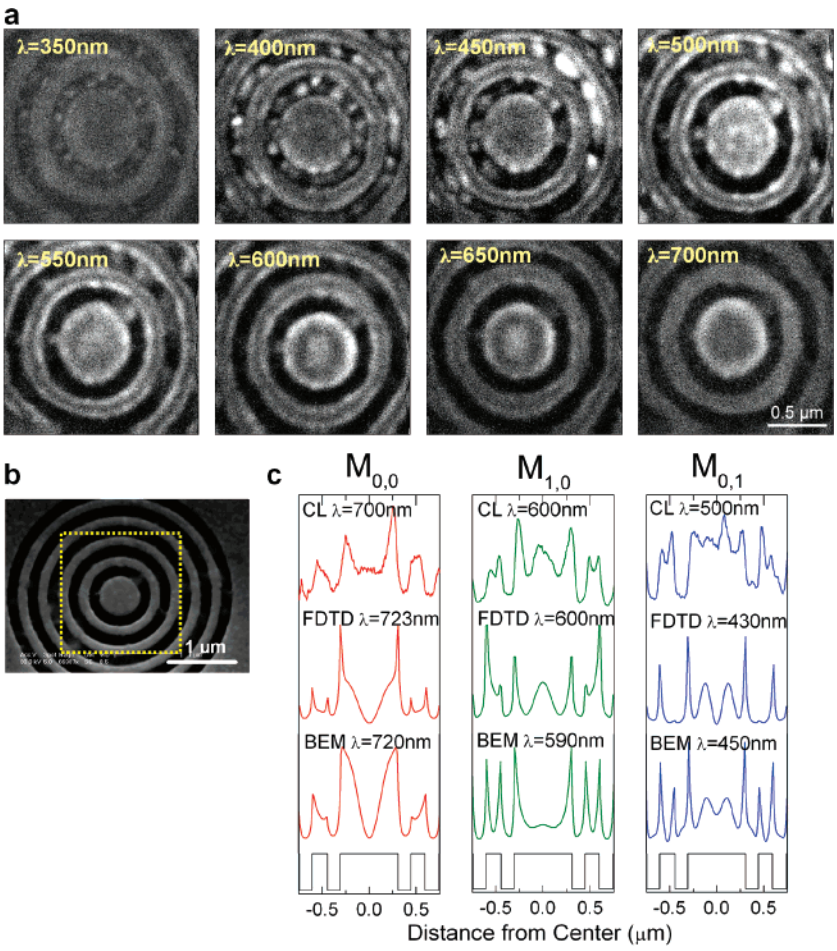

Figure 7.3: Spectrally resolved imaging of plasmonic modes in an Ag annular nanresontator with 620 nm center diameter and 315 nm grating period. **(a)** Spectrally resolved CL images at the indicated wavelengths, each 350×350 pixels^2 with a per pixel dwell time of 10 mn and 27 nm spectral passband. **(b)** SEM image of nanoresonator indicating the scan region for the CT images in (a). **(c)** Line profiles of modes $M_{0,0}$, $M_{1,0}$, and $M_{0,1}$ from finite element FDTD simulated time-averaged electric field intensity, probability of CL emission from BEM simulations, and spectrally resolved CL images at the indicated wavelengths. The corresponding surface topography is shown in gray.

observed at longer wavelengths, as illustrated in Figure 7.3(c). Line profiles of the simulated time-averaged electric field intensity from FDTD and the BEM-calculated probability of CL emission are plotted alongside experimental CL emission profiles $\lambda = 500$ nm, $\lambda = 600$ nm, and $\lambda = 700$ nm. At $\lambda = 700$ nm, CL data show bright emission for excitation near the edges of the center plateau, but uniform emission from the rest of the structure. This is consistent with excitation of $M_{0,0}$, where high fields are localized at the edges of the center region and not in the surrounding rings. Mode $M_{1,0}$, imaged at $\lambda = 600$ nm, is characterized by an antinode in the resonator center that is captured in experimental and simulated line profiles. The onset of $M_{0,1}$ is observed at $\lambda = 500$ nm with four peaks in the center region revealed in the CL linescan. These regions of enhanced emission in the center plateau correlate well with the simulated electric field intensity and CL profiles. For modes $M_{0,0}$ and $M_{0,1}$, the best agreement between simulated and experimentally imaged modes is found for slightly different wavelengths. This can be attributed to uncertainty in parametrization of the effective dielectric function in the grooves of the fabricated Ag nanoresonators. The FIB milling of polycrystalline Ag leads to very rough surfaces in the grooves, preventing accurate representation of the groove depth and profile in simulations. The remaining spectrally resolved CL images in Figure 7.3(a) can be understood primarily as superpositions of $M_{0,0}$, $M_{1,0}$, and $M_{0,1}$.

To further explore higher order modes in plasmonic nanoresonators, larger structures were fabricated in single-crystal Au. The absence of grain boundaries and hence longer propagation lengths enable clear observations of modes in larger resonators. Figure 7.4(a) shows spectrally resolved CL images of a resonator with a 2.6 μm center plateau surrounded by 15 concentric grooves with 250 nm grating period. The experimental line profiles in Figure 7.4(b) indicate that the CL emission along the center region varies with wavelength, showing modes with 5, 6, and 7 antinodes at wavelengths of $\lambda = 798$ nm ($M_{1,2}$), $\lambda = 720$ nm ($M_{0,3}$), and $\lambda = 661$ nm ($M_{1,3}$), respectively. The probability of CL emission is calculated from BEM simulations of this Au resonator with the number of grooves truncated at five. Simulated CL intensity line profiles at wavelengths of $\lambda = 800$ nm, $\lambda = 730$ nm, and $\lambda = 660$ nm are also plotted in Figure 7.4(b). Although the scan area of 5 μm $\times$ 5 μmprevents experimentally resolving the simulated peaks in emission intensity at the edges of the grooves, extremely good agreement is found between spatial variation of the experimental and calculated CL intensity along the center region for each mode.

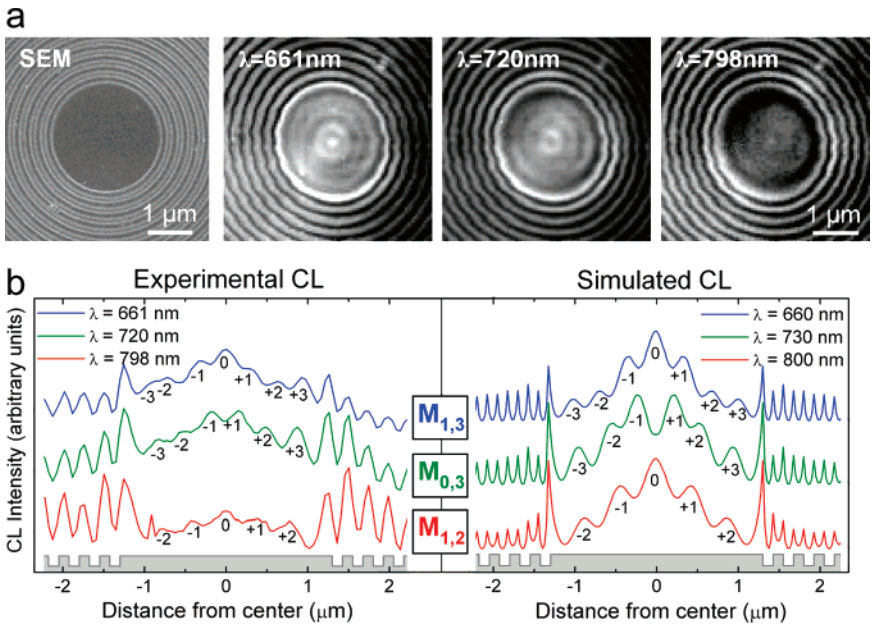

Figure 7.4: Imaging modes in a single-crystal Au nanoresonator with a 2.6 μm diameter center plateau surrounded by 15 grooves with 240 nm grating ring period and 100 nm groove depth. **(a)** SEM image of nanoresonator and spectrally resolved CL images at the wavelengths indicated. **(b)** Line profiles of modes $M_{1,3}$, $M_{0,3}$, and $M_{1,2}$ from spectrally resolved CL images and simulated CL intensity along the center of the resonator in (a). Experimental line traces at the designated wavelengths are obtained by summation over 4 pixel lines in the horizontal direction, corresponding to a 193 nm line width. Simulated CL intensity is calculated from BEM simulations. The peaks in CL intensity along the center region are numbered for both experimental and simulated line profiles. Surface topography is shown in gray.

7.3 Conclusion

We have demonstrated high-resolution spectrally resolved CL imaging as a powerful tool to reveal plasmonic modes in Ag and Au annular nanoresonators. Boundary element method calculations of the CL emission characteristics for each resonator mode agree very well with experimental results. Further, we have used fullfield electromagnetic simulations to identify the plasmonic modes of Ag nanoresonators, and we have proposed a direct correlation between the luminescence emission intensity and electron beam excitation at antinodes of the electric field intensity corresponding to particular plasmonic modes.

Part III

Guided-wave Plasmonics

Chapter 8

Plasmon Slot Waveguides: Towards Chip-Scale Propagation with Subwavelength-Scale Localization

In this chapter, we present a numerical analysis of surface plasmon waveguides exhibiting both long-range propagation and spatial confinement of light with lateral dimensions of less than 10% of the free-space wavelength[1]. Attention is given to characterizing the dispersion relations, wavelength-dependent propagation, and energy density decay in two-dimensional Ag/SiO_2 /Ag structures with waveguide thicknesses ranging from 12 nm to 250 nm. As in conventional planar insulator-metal-insulator (IMI) surface plasmon waveguides, analytic dispersion results indicate a splitting of plasmon modes corresponding to symmetric and antisymmetric electric field distributions as SiO_2 core thickness is decreased below 100 nm. However, unlike IMI structures, surface plasmon momentum of the symmetric mode does not always exceed photon momentum, with thicker films ($d \sim 50$ nm) achieving effective indices as low as $n = 0.15$. In addition, antisymmetric mode dispersion exhibits a cutoff for films thinner than $d = 20$ nm, terminating at least 0.25 eV below resonance. From visible to near infrared wavelengths, plasmon propagation exceeds tens of microns with fields confined to within 20 nm of the structure. As the SiO_2 core thickness is increased, propagation distances also increase with localization remaining constant. Conventional waveguiding modes of the structure are not observed until the core thickness approaches 100 nm. At such thicknesses, both transverse magnetic and transverse electric modes can be observed. Interestingly, for nonpropagating modes (i.e., modes where propagation does not exceed the micron scale), considerable field enhancement in the waveguide core is observed, rivaling the intensities

[1] This chapter has been adapted from Dionne, Sweatlock et al., Reference [32].

reported in resonantly excited metallic nanoparticle waveguides.

8.1 Introduction

Photonics has experienced marked development with the emergence of nanoscale fabrication and characterization techniques. This progress has brought with it a renewed interest in surface plasmons (SPs) — electron oscillations that allow electromagnetic energy to be localized, confined, and guided on subwavelength scales. Waveguiding over distances of 0.5 μm has been demonstrated in linear chains of metal nanoparticles [82], and numerous theoretical and experimental studies [22, 31, 94, 121] indicate the possibility of multicentimeter plasmon propagation in thin metallic films. Moreover, the locally enhanced field intensities observed in plasmonic structures promise potential for molecular biosensing [50, 54, 84, 94], surface-enhanced Raman spectroscopy [41, 46, 149], and nonlinear optical device applications [5, 16, 124, 129, 135].

In planar metallodielectric geometries, surface plasmons represent plane-wave solutions to Maxwell's equations, with the complex wave vector determining both field symmetry and damping. For bound modes, field amplitudes decay exponentially away from the metal/dielectric interface with field maxima occurring at the surface. While the dispersion properties of long-ranging SPs mimic those of a photon, multicentimeter propagation is often accompanied by significant field penetration into the surrounding dielectric. For thin Ag films ($\sim$10 nm) excited at telecommunications frequencies, electric field skin depths can exceed 5 μm [22, 31]. In terms of designing highly integrated photonic and plasmonic structures, a more favorable balance between localization and loss is required.

Surface plasmon polariton modes at a single metal/dielectric interface exhibit strongly wavelength-dependent electric field penetration depths, increasing rapidly in the dielectric as the wavelength is varied away from resonance. The field penetration in the metal, however, remains approximately constant ($\sim$ 25 nm) over a wide range of visible and near-infrared excitation frequencies. This observation has inspired a new class of plasmon waveguides that consist of an insulating core and conducting cladding. Not unlike conventional waveguides, including dielectric slab waveguides at optical frequencies, metallic slot waveguides at microwave frequencies, and the recently proposed semiconductor slot waveguides [2], these metal-insulator-metal (MIM) struc-

tures guide light via the refractive index difference between the core and cladding. However, unlike dielectric slot waveguides, both plasmonic and conventional waveguiding modes can be accessed, depending on transverse core dimensions. MIM waveguides may thus allow optical waveguide mode volumes to be reduced to subwavelength scales, even for frequencies far from the plasmon resonance. Several theoretical studies have already investigated surface plasmon propagation and confinement in MIM structures [36, 147]. However, few studies have investigated wavelength-dependent MIM properties arising from realistic models for the complex dielectric function of metals. In this chapter, we discuss the surface plasmon and conventional waveguiding modes of MIM structures, characterizing the metal by the empirical optical constants of Johnson and Christy [58] and numerically determining the dispersion, propagation, and localization for both field symmetric and antisymmetric modes.

When a plasmon is excited at a metallodielectric interface, electrons in the metal create a surface polarization that gives rise to a localized electric field. In insulator-metal-insulator (IMI) structures, electrons of the metallic core screen the charge configuration at each interface and maintain a near-zero (or minimal) field within the waveguide. As a result, the surface polarizations on either side of the metal film remain in phase and a cutoff frequency is not observed for any transverse waveguide dimension. In contrast, screening does not occur within the dielectric core of MIM waveguides. At each metal-dielectric interface, surface polarizations arise and evolve independently of the other interface, and plasma oscillations need not be energy- or wavevector-matched to each other.

Therefore, for certain MIM dielectric core thicknesses, interface SPs may not remain in phase but will exhibit a beating frequency; as transverse core dimensions are increased, "bands" of allowed energies or wave vectors and "gaps" of forbidden energies will be observed. This behavior is illustrated in Figure 8.1, which plots the TM dispersion relations for an MIM waveguide with core thicknesses of 250 nm (Figure 8.1(a)) and 100 nm (Figure 8.1(b)). The waveguide consists of a three-layer metallodielectric stack with an SiO_2 core and an Ag cladding. The metal is defined by the empirical optical constants of Johnson and Christy [58] and the dielectric constant for the oxide is adopted from Palik's handbook [75].

Solution of the dispersion relations was achieved via application of a Nelder-Mead minimization routine in complex wave-vector space; details of implementation and convergence properties are described elsewhere

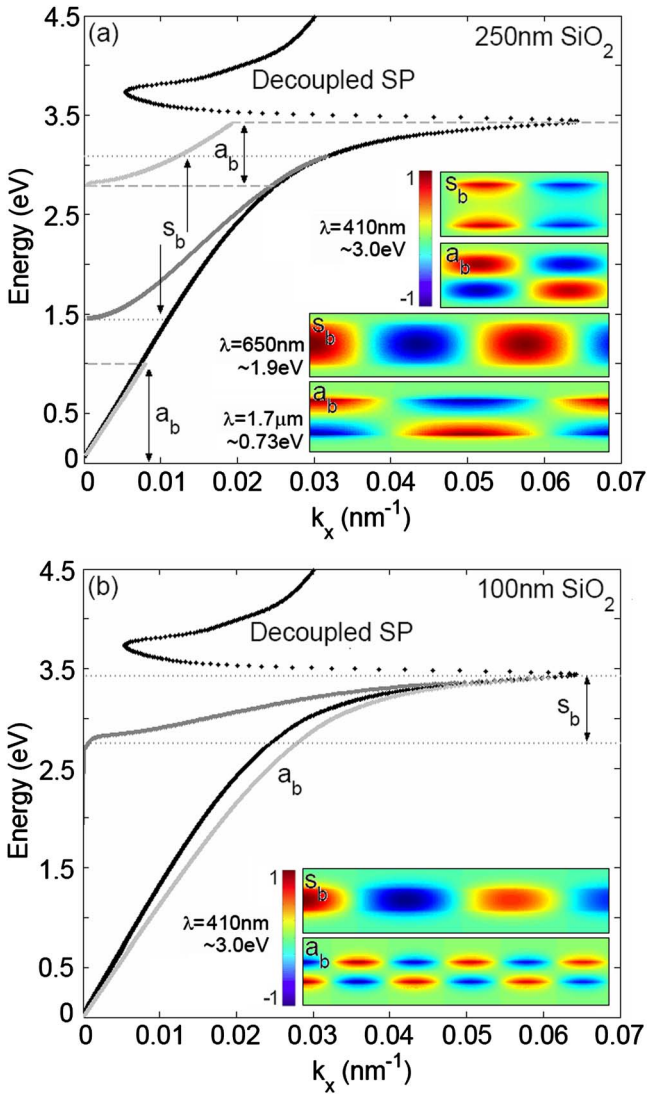

Figure 8.1: Dispersion relations for MIM planar waveguides with an SiO_2 core and Ag cladding

[31]. For reference, the figures include the waveguide TM dispersion curve in the limit of infinite core thickness, plotted in black. Allowed wave vectors are seen to exist for all freespace wavelengths (energies) and exhibit exact agreement with the dispersion relation for a single Ag/SiO_2 interface SP.

Figure 8.1(a) plots the "bound" modes (i.e., modes occurring at frequencies below the SP resonance) of a Ag/SiO_2/Ag waveguide with core thickness $d = 250$ nm. The asymmetric bound (a_b) modes are plotted in light gray; the symmetric bound (s_b) modes are plotted in dark gray. As seen, multiple bands of allowed and forbidden frequencies are observed. The allowed a_b modes follow the light line for energies below ~ 1 eV and resemble conventional dielectric core, conducting cladding waveguide modes for energies above ~ 2.8 eV. Tangential electric fields in each a_b regime are plotted in the inset and highlight the distinction in mode localization: At 410 nm, the mode is localized within the waveguide core and resembles a conventional TM waveguide profile. At 1.7 μm, dispersion is more plasmonlike and field maxima of the mode occur at each metal-dielectric interface. In contrast, the s_b modes are only observed for energies between 1.5 and 3.2 eV. Dispersion for this mode is reminiscent of conventional dielectric core, dielectric cladding waveguides; with end-point asymptotes corresponding to tangent slopes (i.e., effective optical indices) of $n = 8.33$ at 1.5 eV and $n = 4.29$ at 3.2 eV. For energies exceeding ~ 2.8 eV, wave vectors of the s_b mode are matched with those of the SP and the tangential electric field transits from a core mode to an interface mode (cf. the 1st (~ 3 eV) and 3rd (~ 1.9 eV) panels of the inset). As the core layer thickness is increased through 1 μm (data not shown), the number of a_b and s_b bands increases, with the a_b modes generally lying at higher energies. In analogy with conventional waveguides, larger (but bounded) core dimensions increase the number of modes supported by the structure.

Figure 8.1(b) plots the bound mode dispersion curves for an MIM waveguide with SiO_2 core thickness $d = 100$ nm. Again, the allowed a_b modes are plotted in light gray while the allowed s_b modes are dark gray. Although the s_b mode resembles conventional waveguide dispersion, the a_b mode is seen to exhibit plasmonlike behavior. Accordingly, the conventional waveguiding modes are found only at higher energies (over a range of about 1 eV), where photon wavelengths are small enough to be guided by the structure. The inset shows snapshots of the tangential electric field for both modes at a free-space wavelength $\lambda = 410$ nm (~ 3 eV). As seen, the s_b field is concentrated in the waveguide core with minimal penetration into

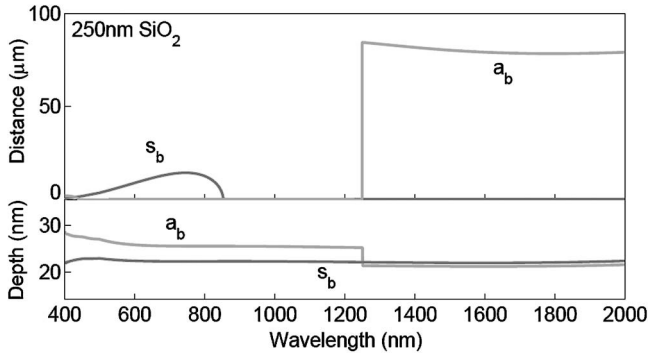

Figure 8.2: MIM ($Ag/SiO_2/Ag$) TM-polarized propagation and skin depth plotted as a function of wavelength for a core thickness of $d = 250$ nm. Both s_b and a_b modes are observed and exhibit cutoff in accordance with the dispersion curve of Figure 8.1.

the conducting cladding. In contrast, the a_b field is highly localized at the surface, with field penetration approximately symmetric on each side of the metal-dielectric interface. The presence of both conventional and SP waveguiding modes represents a transition to subwavelength-scale photonics. Provided momentum can be matched between the photon and the SP, and energy will be guided in a polariton mode along the metal-dielectric interface. Otherwise, the structure will support a conventional waveguide mode, but propagation will only occur over a narrow frequency band. As MIM core thickness is reduced below 100 nm, the structure can no longer serve as a conventional waveguide. Light impinging the structure will diffract and decay evanescently, unless it is coupled into a SP mode.

8.2 Mode Propagation and Skin Depth

Surface plasmon dispersion and propagation in planar structures are governed by the real and imaginary components, respectively, of the in-plane wave vector. Generally, propagation is high in regimes of near-linear dispersion where high signal velocities overcome internal loss mechanisms. In insulator/metal/insulator (IMI) structures, long-range propagation is achieved at the expense of confinement: transverse field penetration typically exceeds microns in the surrounding dielectric. In MIM structures, SP penetration into the cladding will be limited by the skin depth of optical fields in the metal. This restriction motivates the question of how skin depth affects propagation, particularly for thin films.

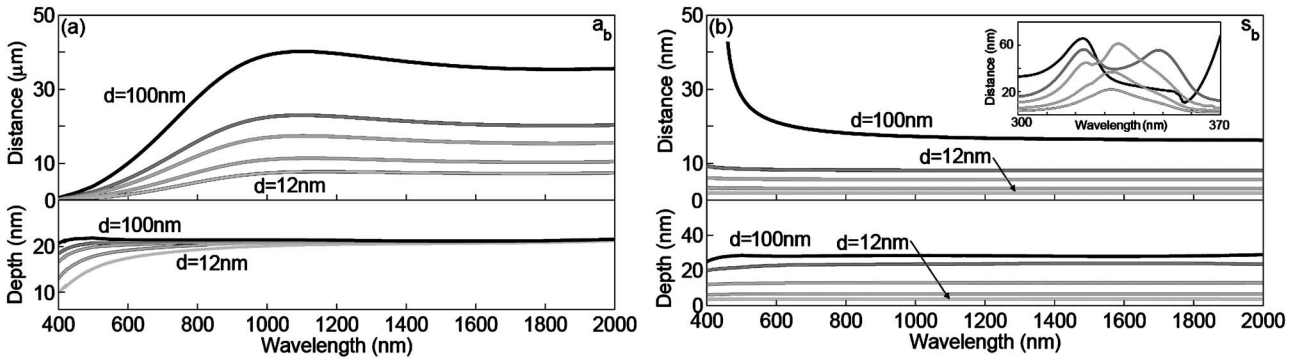

Figure 8.3: MIM (Ag/SiO_2/Ag) TM-polarized propagation and skin depth plotted as a function of wavelength for core thicknesses of $d = 12$ nm, 20 nm, 35 nm, 50 nm, and 100 nm. **(a)** Field antisymmetric modes of MIM guides propagate over 10 μm with skin depth never exceeding approximately 20 nm. **(b)** Symmetric modes of thinner films $d \leq 50$ nm remain evanescent for all wavelengths. However, as d approaches 100nm, conventional waveguiding modes can be accessed, and a region of long propagation distance is observed for $\lambda \leq 400$ nm. Inset: Propagation distances of the symmetric mode for wavelengths characteristic of the quasibound regime. The transition from the thin-film single peak to the thick-film double peak indicates the onset of conventional waveguiding.

Figures 8.2 and 8.3 illustrate the interdependence of skin depth and propagation in MIM structures for film thicknesses from 12250 nm. The top panels plot propagation of the TM modes for the structure as a function of free-space wavelength; the bottom panels plot the corresponding skin depth. Figure 8.2 plots propagation and skin depth for a 250 nm oxide layer. In accordance with the dispersion relations, wave propagation exhibits allowed and forbidden bands for the symmetric and antisymmetric modes. The s_b mode is seen to propagate for wavelengths between 400 and 850 nm, with maximum propagation distances of $\sim$15 μm. The skin depth for this mode is approximately constant over all wavelengths, never exceeding 22 nm in the metal. In contrast, the a_b mode is seen to propagate distances of 80 μm for wavelengths greater than 1250 nm. For wavelengths below 450 nm, a smaller band of propagation is also observed, though distances do not exceed 2 μm. In regions of high propagation (i.e., above 1250 nm), skin depth remains approximately constant at 20 nm; below 1250 nm, however, skin depths approach 30 nm. Interestingly, the figure indicates only a slight correlation between propagation and skin depth for both the a_b and s_b modes. This relation suggests that the metal (i.e., absorption) is not the limiting loss mechanism for wave propagation in MIM structures.

Figure 8.3(a) illustrates the propagation distance and skin depth for the antisymmetric bound mode for

oxide thicknesses from 12 to 100 nm. The continuous plasmon-like dispersion relations of Figs. 8.1 are well correlated with the observed propagation: decay lengths are longest for larger wavelengths, where dispersion follows the light line. Plasmon propagation generally increases with increasing film thickness, approaching $\sim$ 10 μm for a 12 nm oxide layer and 40 μm for a 100 nm thick oxide. Nevertheless, field penetration remains approximately constant in the Ag cladding, never exceeding 20 nm. Thus, unlike conventional plasmon waveguides, MIM waveguides can achieve micron-scale propagation with nanometer-scale confinement.

Figure 8.3(b) plots propagation and skin depth for the symmetric bound modes of thin films. As with the a_b modes, larger oxide thicknesses support increased propagation distances. However, the wave remains evanescent for thicknesses up through 50 nm, with propagation not exceeding 10 nm for longer wavelengths. As SiO_2 thicknesses approach 100 nm, a band of allowed propagation is observed at higher frequencies, reflecting the dispersion of Figure 8.1(b): at $\lambda = 400$ nm, propagation lengths are as high as 0.5 μm. In addition, thin films exhibit a local maximum in propagation for wavelengths corresponding to the transition between quasibound and radiative modes (see inset), analogous to IMI guides [31]. For films with $d < 35$ nm, only a single peak is observed. However, as film thickness is increased, the peak begins to split, with the lower energy peak forming the first band of allowed propagation. The transition indicates a dissociation of the quasi-bound modes and marks the onset of conventional waveguiding. While this regime is characterized by a slight increase in skin depth, field penetration for a given d remains generally constant over the full wavelength range. Thus, unlike IMI structures, extinction is determined not by ohmic losses but by field interference upon phase shifts induced by the metal. Whether MIM structures support propagating modes or purely evanescent fields, skin depth is limited by absorption and will not exceed 30 nm.

8.3 Conclusions

Device architectures of present are reliant on index contrasted media for signal storage and transmission. Accordingly, conventional waveguides are both well understood and heavily utilized for light propagation on macroscopic scales. However, as device sizes are scaled to theoretical limits, light-matter interactions must be tuned to support modes within nanoscopic dimensions. Conversion of the photon mode into a surface

plasmon mode is one such mechanism for subwavelength-scale signal transmission. In thin metallic films, surface plasmons can propagate over tens of centimeters at infrared wavelengths. However, this long-range propagation is achieved at the expense of confinement: field penetration increases exponentially from the metal-dielectric interface, extending over several microns into the surrounding dielectric. In contrast, the skin depth of MIM structures is limited by optical decay lengths in the metal. As the waveguide core is reduced to nanometer sizes, the structure still supports propagation over 10 μm, with fields confined to within 20 nm of the structure. Depending on transverse dimensions, MIM waveguides can support both conventional and plasmonic modes; cutoff wave vectors are not observed until the core diameter is reduced below $\sim$ 20 nm or exceeds $\sim$ 100 nm. This superposition of modes results in wide tunability of energy density throughout the electromagnetic spectrum. While energy densities are generally high at the metal interface, intensities within the waveguide can be comparable to values observed in nanoparticle array gaps.

Judicious arrangement of IMI and MIM plasmon waveguides promises potential for two-dimensional planar loss-localization balance. When combined with the recent remarkable progress in nanoscale fabrication, the aforementioned results might inspire an alternative class of waveguide architectures – ultimately, a class of subwavelength plasmonic interconnects, not altogether different from the silicon-on-insulator networks of today.

Chapter 9

Plasmonic Waveguide Cavity and Incoupling Analysis

9.1 Incoupling into Metal/Insulator/Metal Structures

In recent experimental studies [29, 30, 72] of metal/insulator/metal (MIM) or "plasmonic slot" waveguides, our laboratory has developed a method of coupling light into MIM stacks through subwavelength slits. These slits consist simply of narrow channels milled with a focused ion beam (FIB) through the top metal waveguide cladding and perhaps partway through the waveguide core (illustrated in cross section in the 2D schematic, Figure 9.1(a)). When illuminated by a lamp or laser, the slit is found to be effective at scattering light into waveguided modes of the MIM. These waveguided modes are launched with propagation direction transverse to the slit axis. Another, parallel slit can be milled some distance d away which scatters light from the guided modes back into free space. If this output slit is milled through only the bottom surface, the result is a dual-sided coupling geometry which allows investigation of waveguide propagation in a dark-field configuration with both far-field illumination and detection [30].

Such a double-slit scheme is an excellent geometry for laboratory investigation; since there is no direct path from the optical source to detector, the dark-field measurement has good signal-to-noise performance in general. However the absolute quantity of power coupled in through the subwavelength aperture may be small (in other words, the insertion loss is large). The incoupled power is highly sensitive to the exact geometry (e.g., width and depth) of the slit. The slit shape influences both the scattering power of the slit itself, and the spatial overlap of the scattered power with the guided modes of the MIM.

Recently we have demonstrated the operation of a micron-scale electrooptic modulator, in a device which combines plasmonic slot waveguiding with the electrical characteristics of a metal-oxide-silicon capacitor, or "plasmostor." Near-infrared transmission between an optical source and drain is controlled by an applied electric field that modulates the complex refractive index of the Si. In the dark-field configuration, amplitude modulation depths as large as 11.2 dB are achieved. Modulation is observed in devices with channel areas (length x thickness) as small as $0.01\lambda^2$, with sub-nanosecond switching speeds and minimal power requirements [29].

However, in order to consider integration of plasmostors or other subwavelength active devices as constituents of dense subwavelength photonic networks, we must also address strategies for coupling light in from in-plane, and develop design strategies to achieve low overall loss. From semianalytic mode calculation (see Ch. 8) we determine that the losses intrinsic to the waveguided modes of the plasmostor are around 1 dB. Theoretical results from the group of Fan et al. [137] have indicated insertion losses as low as 0.3 dB for an optimized, impedance matching coupler between a dielectric slab waveguide and a plasmonic MIM.

In this section, we employ FDTD simulation, first to characterize the loss of the actual slit coupler which has been employed in the actual plasmostors fabricated to date in Figure 9.1(a), and then to survey alternative coupling schemes which are achievable with minimal incremental changes to the fabricated device structure in Figure 9.1(c,e,g). The simulated MIM stack consists of a core of 160 nm of Si, with 10 nm layer of oxide on one side, and clad on both sides by 400 nm Ag. The simulation is 2D with PML boundaries. Material data are from the Palik handbook, using the Lorentz-Drude model for the dispersive dielectric of Ag, and are given in Appendix B. In all simulations the incident light is TM polarized, monochromatic, continuous wave excitation at the operating frequency of the plasmostor, $\lambda_0 = 1550$ nm. In the chosen coordinate system the MIM propagation axis is $\hat{z}$. In all cases the input port, whether slit or waveguide end facet, is centered at the center of the simulation volume, with coords $[z,x] = [2,0]$ μm. The power which is considered "incoupled" is that which passes is steady state through a monitor port consisting of a line segment which intersects the waveguide axis at $[z,x] = [2.5, -0.4 : 0.4]$ μm.

The following incoupling conditions are considered:

1. *Slit Incoupling.* Source plane is a Gaussian beam with waist (1/e radius) of $w_0 = 1.5$ μm in the plane

$x = 1\mu$m, about a half micron above the surface. The slit is an air-filled opening transverse the the waveguide, 400nm wide, 490nm deep through the metal cladding and halfway into the Si core. Note that the assumption that the focal radius $\approx \lambda$ is somewhat arbitrary but intended as a "best case" estimate; practically the spot would almost certainly be much larger. The reported incoupling coefficient represents the energy coupled into the MIM guide in the $+\hat{z}$ direction; due to the symmetry of this coupling scheme, the same amount also couples into the $-\hat{z}$ direction.

2. *Endfire Incoupling.* Source plane is a Gaussian beam with waist $w_0 = 1.5$ μm, incident normal to the end facet of a truncated MIM.

3. *Thin Waveguide Incoupling.* Source is the lowest-order TM mode of an air-clad Si-core waveguide with a 160 nm core, the same thickness as the Si core of the MIM.

4. *Tapered Waveguide Incoupling.* Source is the lowest-order TM mode of an air-clad Si-core waveguide with a 970 nm core, the same thickness as the entire MIM stack. This waveguide is joined to the 170 nm Si core of the MIM by a 1 μm segment of concave parabolic taper. The tapered segment is clad in air.

5. *Metal-Clad Tapered Incoupling.* Source is the lowest-order TM mode of an air-clad Si-core waveguide with a 970 nm core, same thickness as the entire MIM stack. This waveguide is joined to the 170 nm Si core of the MIM by a 1 μm segment of concave parabolic taper. The tapered segment is clad in Ag.

Table 9.1: Power incoupled to Ag/Si/Ag plasmonic waveguide from free space Gaussian beams in endfire or slit configuration, or from Si core dielectric waveguide.

Geometry	Incoupled Power (%)	Incoupled Power (dB)
Slit, Tightly focused beam	5.2%	-12.8dB
Endfire, Tightly focused beam	14.8%	-8.3dB
Thin 160 nm waveguide, endfire	35.9%	-4.4dB
970 nm guide, Air clad taper	20.4%	-6.9dB
970 nm guide, Ag clad taper	24.0%	-6.2dB

We find that the insertion loss for the waveguide end-fire scheme, see Table 9.1, is only -4.4 dB, an improvement of about 8 dB over the currently employed slit-coupling geometry. This type of analysis allows us to trade off the demand for increased performance with the desire to minimize added design complexity. Most

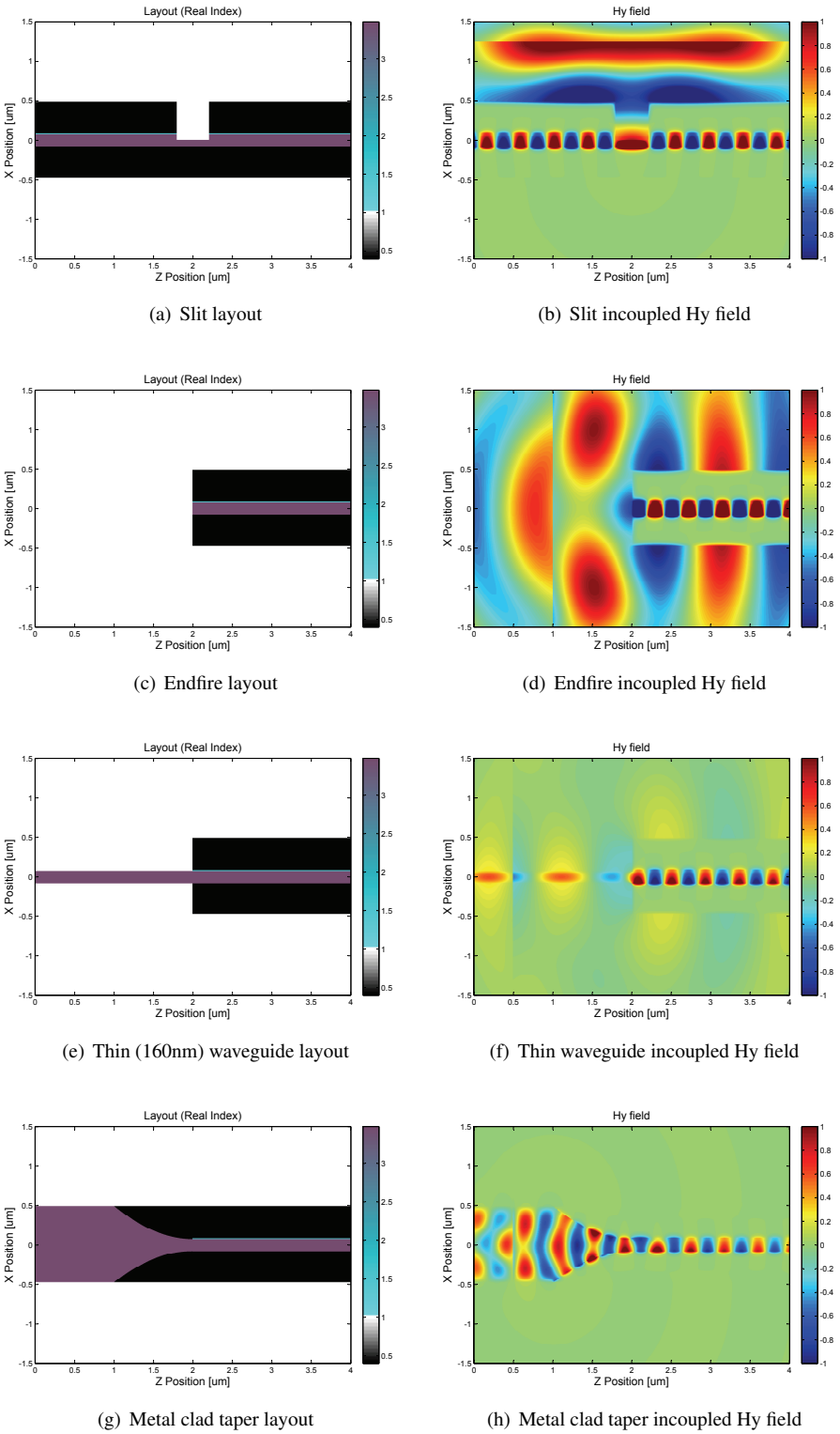

(a) Slit layout

(b) Slit incoupled Hy field

(c) Endfire layout

(d) Endfire incoupled Hy field

(e) Thin (160nm) waveguide layout

(f) Thin waveguide incoupled Hy field

(g) Metal clad taper layout

(h) Metal clad taper incoupled Hy field

Figure 9.1: Illustrated survey of simulated geometries for coupling into Ag/Si/Ag plasmonic waveguide from free space Gaussian beams or from Si core dielectric waveguide. Left column: Color scale represents the materials' real optical index in all space, materials Ag (black), air (white), Si (purple), and oxide (blue) are visible. Right column: Hy field at simulated steady-state.

importantly, the substantial improvement reported here can be achieved without varying the width of the Si core in the dielectric waveguide region relative to that of the core in the MIM active region.

9.2 Multilayer MIM structures with vias

In the following section, we study a stack containing two MIM waveguides, separated from each other by a 150 nm thick layer of Ag cladding[1]. The cladding silver layer is thick enough to suppress crosstalk due to mode coupling between the top and bottom waveguides. The waveguides' dielectric cores are here modeled as a purely transparent dielectric $n_1 = (2.02 + 0\mathrm{i})$, corresponding to that of silicon nitride at the excitation wavelength $\lambda = 1500$ nm. The two MIM waveguide layers are connected only by SPP propagation through slits or "vias" which are, here, only 50 nm wide. Note that the relative fraction of light which is "tapped" off by the via can be adjusted by varying the via width, or by fabricating the via in a manner that provides dielectric contrast relative to the core material.

Several interesting properties are illustrated by a simple simulation of two buried waveguides connected by a single via, as in Figure 9.2. The top of the simulation volume is illuminated by a plane wave incident upon a slit in-coupler; in this section we do not explicitly consider the insertion loss of this first element. This input slit, located at $(x,z) = (0.2,5)$ launches propagating waveguide modes into the top MIM layer, both to the left ($-\hat{z}$) and to the right ($\hat{z}$). Those waves which are launched to the right propagate uneventfully. From Figure 9.2(c), the slope of the blue line representing a cross section through the top waveguide, for $z > 5$, indicates that attenuation of this guided mode is about -0.6 dB (amplitude) per μm, i.e., -1.2 dB (power) per μm.

On the other hand, those waves which are launched to the left soon encounter the "via" at $(x,z) = (0,2)$ which connects the top and bottom waveguides. In this context, the juction formed by a horizontal waveguide layer and a via acts like a three terminal "T"-splitter. The reflection amplitude $\sqrt{R} = r$ (square root of reflected power) from this junction can be inferred from the standing wave ratio (SWR) observed in the "cavity," the waveguide region between the via and input slit:

[1]This discussion of simulated multilayer MIM structures will appear in a forthcoming book chapter Pacifici, Lezec, Sweatlock et al. Reference [101]. In that manuscript we also discuss preliminary experimental realization of interferometric all-optical switching functionality in buried MIM networks.

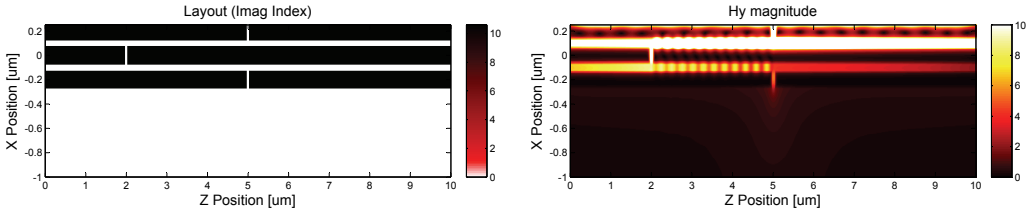

(a) Schematic

(b) Hy field magnitude

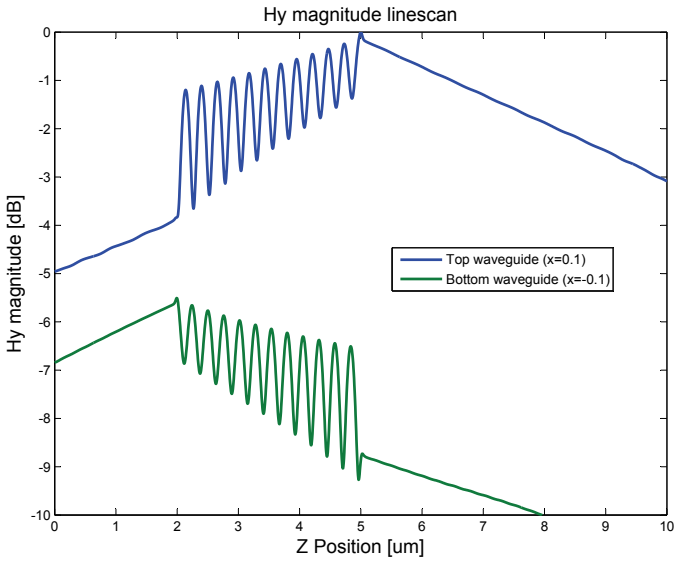

(c) Hy field magnitude, linescans

Figure 9.2: Stack of two buried metal-insulator-metal (MIM) waveguides connected by single via. **(a)**: Color scale represents the materials' imaginary optical index in all space, materials Ag (black), and transparent $n_c = (2.02 + 0i)$ (white) are visible. **(b)**: Simulated magnitude of H_y field when the device is illuminated through the slit in the top metal surface. **(c)**: Cross sections of the H_y magnitude along the center axis of the top and bottom waveguide layers.

$$\sqrt{R} = r = \frac{\mathrm{SWR} - 1}{\mathrm{SWR} + 1}. \tag{9.1}$$

We can determine the other transfer coefficients from Figure 9.2(c), as well. The ratio of the blue line (top waveguide) to that of the green line (bottom waveguide) at positions $z < 2$ show that the ratio between the transmitted amplitude ($\sqrt{T} = t$) and one-half the amplitude split off by the via ($\sqrt{S} = s$) is 2 dB; the power ratio is then $\frac{T}{0.5S} = 4$ dB. Together with $T + R + S = 1$ we find that for mode incident from the waveguide on the junction about 18% is reflected, 46% transmitted, and 36% tapped by the via. On the other hand when the SPP is incident from the via, the junction acts as a 50/50 splitter, with very small back reflection.

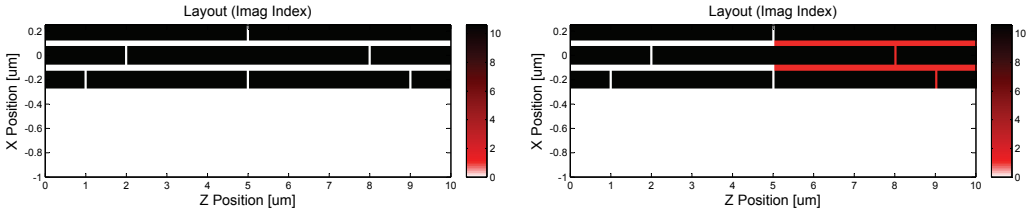

(a) Control structure (no absorption).

(b) Schematic of multilayer MIM structure with absorbing waveguide core

Figure 9.3: Schematic view of multi-layer plasmonic interferometer simulation. **(a)** Control device, in which the waveguide core is everywhere non-absorbing. **(b)** The waveguide core is given non-zero absorption at positions $z > 5$.

Having established the concept of slit "vias" in multilayer MIM structures, we hypothesize the construction of a buried waveguide interferometer. To construct the interferometer we add one more via between top and bottom waveguides, forming another "arm," or equivalent path between the input slit and the output slit at $(x,z) = (-0.2,5)$. We additionally add two more "secondary" output slits in the back surface at $(x,z) = (-0.2,1)$ and $(x,z) = (-0.2,9)$, as in Figure 9.3(a). Here, we envision applications where a single optical input signal is split multiple times, or "fanned out," to a number of output sites. To add extra interest to the simulation we additionally consider filling the waveguide cores with an medium with nonzero absorption, $n_2 = 2.02 + \mathrm{i}k$ in the half-space $z > 5$, as in Figure 9.3(b). This investigation is inspired by experimental demonstration of optically pumped absorption in ultrathin quantum dot layers in Pacifici et al. [100], and the values of imaginary index k used here are chosen in order to acheive attenuation per unit length comparable to the experiment. However, in the current simulation we make two key simplifying assumptions. First, we

do not explicitly simulate the propagation of a "pump" beam which activates the optical absorption in the buried layer, and second, we assume that the real part of the index stays constant even as k varies.

The simulated performance of a multilayer plasmonic interferometer is illustrated in Figure 9.4. In the left column is shown the magnetic field H_y magnitude, providing a clear view of propagation and standing wave patterns within the waveguide stack. In the right column we display the real part of the E_z field under the same conditions, which illustrate more clearly the "beams" of light which emanate from the output slits. One arm of the interferometer ($z < 5$) is always filled with a non-absorbing medium ($n = 2.02$), while the other arm ($z > 5$) is filled with an absorber (a) $n = 2.02 + 0.025\text{i}$, (b) $n = 2.02 + 0.1\text{i}$, (c) $n = 2.02 + 1\text{i}$. The device is illuminated by a plane wave incident on the top input slit and produces three output beams through slits in the bottom metal surface. As absorption is increased: the right output beam is entirely suppressed, the center output beam is diminished, and the left output beam is unchanged.

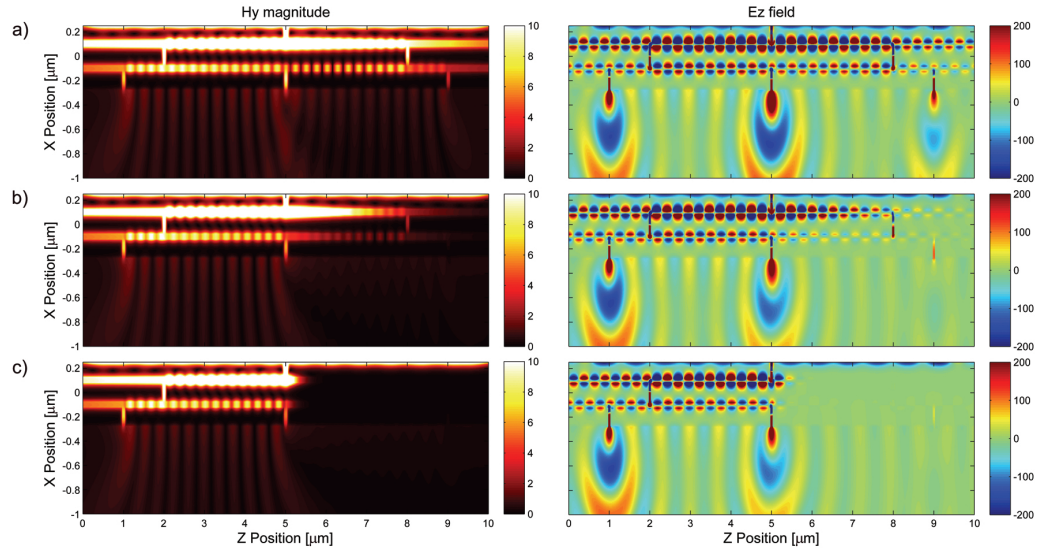

Figure 9.4: Simulated performance (left column Hy magnitude; right column Ez field) of multilayer plasmonic interferometer. One arm of the interferometer ($z < 5$) is always filled with a nonabsorbing medium ($n = 2.02$), while the other arm ($z > 5$) is filled with an absorber **(a)** $n = 2.02 + 0.025\text{i}$, **(b)** $n = 2.02 + 0.1\text{i}$, **(c)** $n = 2.02 + 1\text{i}$. The device is illuminated by a plane wave incident on the top input slit and produces three output beams through slits in the bottom metal surface. As absorption is increased: the right output beam is entirely suppressed, the center output beam is diminished, and the left output beam is unchanged.

9.3 Conclusion

Here in this chapter, we employed finite-difference time domain (FDTD) simulations to evaluate plasmonic waveguide structures which are not readily tractable by analytic methods, specifically structures such as in-couplers and junctions. Simultaneously we have illustrated two phases of the intimate relationship between experiment and numerical analysis. In the first section, we employ numerical methods to characterize the performance of an existing device, the plasmostor. We find that a relatively simple change in the incoupling geometry could result in a 8 dB improvement in incoupling efficiency, providing quantitative feedback for optimizing the next design cycle. In the second section, we instead are using FDTD to pre-screen a hypothetical device, synthesizing several concepts into a "virtual prototype" of a multilayer active plasmonic interferometer.

Part IV

Appendices

Appendix A

Microwave Antenna-Waveguide Subwavelength Interferometer

A.1 Abstract

We construct and characterize a three terminal modulator, which operates in the microwave band at 8.0 GHz (λ = 3.7 cm) via interference of electromagnetic waves confined to a subwavelength structure[1]. On/off ratios of more than 20 dB have been observed.

The modulator consists of intersecting linear arrays of closely spaced metal rods, similar to Yagi antenna aerials, that act as waveguides. The experimental results compare favorably with modeled modulation characteristics determined by full-field electromagnetic simulation. Analogies to potential optical frequency plasmonic devices, consisting of arrays of nanometer-scale metal particles, are discussed.

A.2 Introduction

One research direction for development of devices with optical functionality below the diffraction limit of visible light on the scale of several hundreds of nanometers is plasmon waveguide technology. These structures consist of periodic arrays of closely spaced metal nanoparticles, which provide subwavelength confinement and guiding of light via nearfield interactions, specifically the collective dipole plasmon oscillations of electrons in neighboring particles [18, 113]. Theoretical results have documented the existence of guided modes in plasmon waveguides and furthermore have suggested that light can he routed efficiently around

[1]This chapter has been adapted from Sweatlock et al., Reference [130].

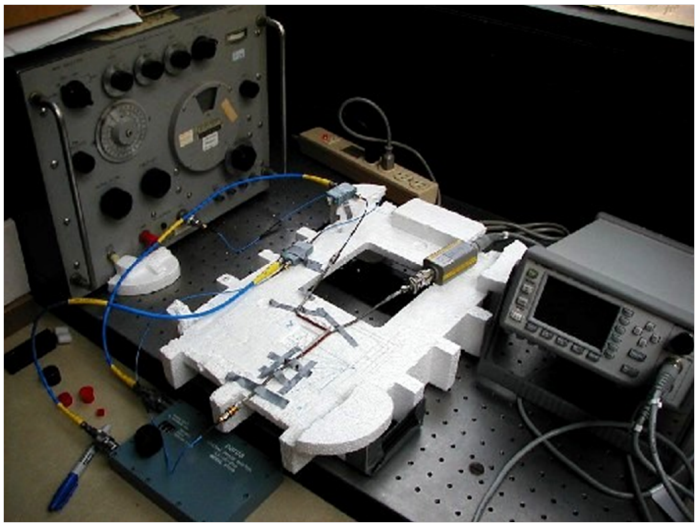

Figure A.1: Microwave antenna waveguide test station.

sharp corners. In recent work our group has provided experimental evidence for energy transport in plasmon waveguides [76, 82]. However, characterization of functional plasmon devices has so far proved elusive, due in part to the experimental challenges of coupling energy into sub-diffraction limit optical size structures.

In a previous publication, we have discussed the analogy between plasmon waveguides and periodic arrays of centimeter-scale copper rods, similar to Yagi antenna aerials [79]. Yagi antenna arrays also confine electromagnetic energy on a subwavelength scale and support coupled dipole propagating modes. This suggests that one can use the radio frequency laboratory as a testing ground for physical principles relevant to plasmon optics.

Here, we present the characterization of a centimeter-sized interferometric modulator that is functionally equivalent to a simple subwavelength all-optical plasmon switch, but operates in the microwave regime at 8.0 GHz ($\lambda = 3.7$ cm).

A.3 Apparatus

The copper rods used to construct our modulator have a diameter of 0.1 cm (0.03 λ) and length 1.4 cm (0.38 λ). They are arranged in linear arrays, spaced equally 0.24 cm (0.06 λ) apart orthogonal to their long axis. The rod arrays are assembled on a platform of Styrofoam that exhibits negligible guiding and small absorption. Our switch design consists of two such linear arrays that meet at right angles to form a T structure. Each of

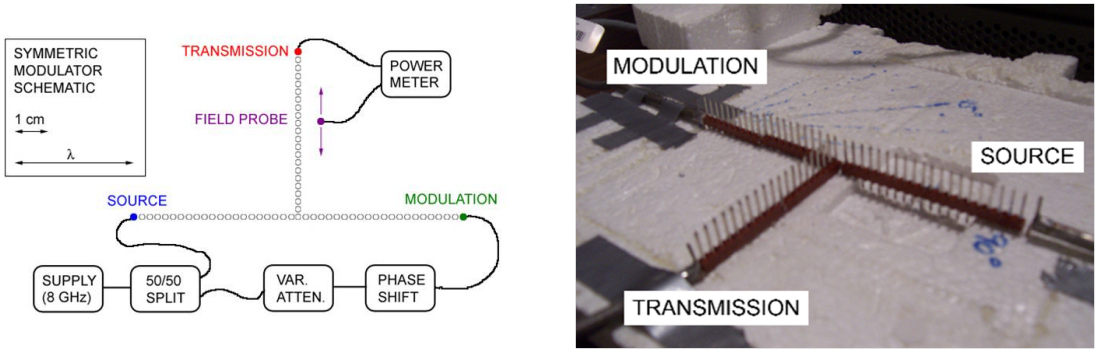

(a) Schematic

(b) Apparatus

Figure A.2: Symmetric Yagi waveguide modulator. Source and modulation signals are generated coherently, but relative attenuation and phase are variable. Power is monitored at the end of the transmission arm, and also can be observed at arbitrary positions via an adjustable probe.

the three arms of the T consists of 20 rods, not including the single rod at the junction point.

One arm is driven at 8.0 GHz by a center-fed dipole antenna, nominally of the same dimension and spacing as any other rod, connected to an Agilent 83711B signal generator. This is referred to as the *source* arm. The gate (or *modulation*) arm is driven by another dipole antenna coherently from the same generator, but with variable attenuation and phase relative to the signal. A third dipole connected to an Agilent E4419B meter is used to monitor the power at the end of the third arm, which we consider to he the *transmission* terminal of the device. Thus, two possible configurations of this T-shaped modulator are possible: If the the signal and gate arms are directly opposite one other at the ends of the "T" crossbar we speak of a symmetric modulator; if instead the gate forms the stem of the "T" we speak of an asymmetric modulator.

When the gate is driven out of phase with the source, the signals combine destructively at the junction and transmitted intensity is expected to lower dramatically. This can be considered the "off" state of the switch. The "on" state can be achieved by changing the gate phase to zero degrees to produce constructive interference, or alternatively by attenuating the gate power.

A.4 Design Considerations

A discussion regarding relative length scales inherent in the microwave waveguide can help to illustrate a key caveat to the analogy with the plasmonic system.

Experimentally [127] it has long been known that periodic rod arrays only guide electromagnetic waves of free-space wavelength λ if the rod length h is less than $\lambda/2$. It has been shown analytically, using transmission line theory, that this fact is related to the idea that such arrays can be represented as a purely reactive load [122]. From an optical viewpoint, a capacitive load ($h < \lambda/2$) leads to a phase velocity less than the speed of free space propagation c. Correspondingly confinement is observed, much like a region of transparent high-index material in a conventional waveguide system. However an inductive load ($h > \lambda/2$) leads to phase velocity greater than c and lack of confinement.

The antenna engineering literature contains further detailed information on the relationship between rod shape parameters and phase velocity in the slow-wave or capacitive regime [122, 123, 127]. To summarize key results, phase velocity decreases as rod spacing decreases, and decreases as rod length increases. Our waveguide arrays consist of relatively long, closely spaced rods. Such a design provides tight confinement in the lateral direction, which mimics plasmon waveguides and helps minimize radiation loss at sharp corners. Typical Yagi aerials that may be a familiar sight on rooftops or transmission towers are aimed at radiating out electromagnetic energy into the far field and have much wider spacing between elements of typically $\lambda/3$.

Plasmon waveguides, on the other hand, represent a resistive rather than purely reactive load. They operate at the frequency corresponding to the surface plasmon resonance in the constituent nanoparticles. The resonantly enhanced absorption and scattering cross sections of the particles allow for efficient excitation, and strong coupling between particles [63]. Coupling strength is high even for particle sizes that are small compared to the interparticle spacing and very small relative to the wavelength. In this regime nearest-neighbor coupling interactions can dominate and therefore plasmon waveguides allow for propagation around sharp corners with essentially zero radiation loss in the point-dipole limit. However, their resistive impedance also contributes attenuation to the transmission line. Whereas a reactive load can support in principle an infinitely propagating wave, the high attenuation in plasmon waveguides limits device geometries to the order of a few free space wavelengths.

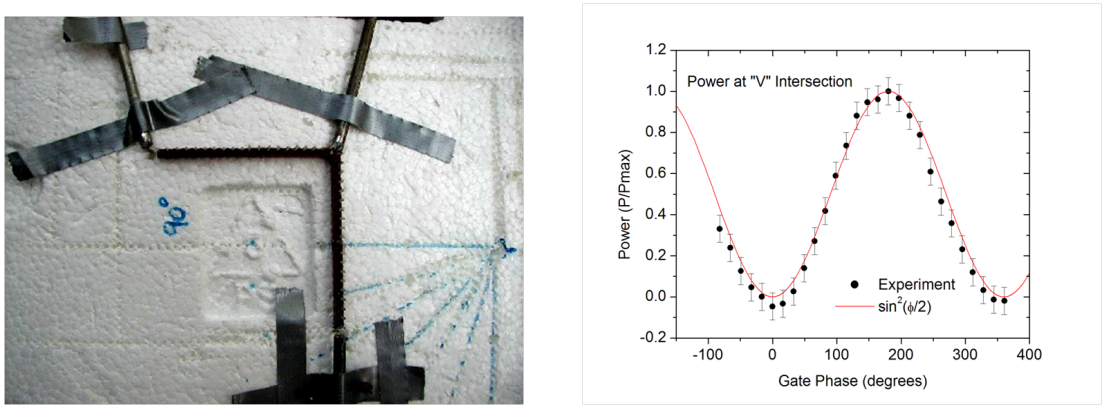

(a) Topdown photo

(b) Power modulation

Figure A.3: Interference observed at the right-angle intersection of two 20-rod Yagi waveguides, in normalized received power versus the relative phase of signal input to the two arms. The solid line indicates the expected functional form.

A.5 Demonstration of Concept

A preliminary experiment demonstrates the feasibility of observing interference effects in Yagi waveguides. Here, the transmission arm is removed and power is monitored at a simple right-angle intersection of the gate and source arm. The same amount of power is applied to both gate and source while varying the phase.

The solid line in Figure A.3 represents the anticipated functional form for destructive interference of two sinusoidal signals of equal amplitude normalized to the maximum power. The experimentally measured phase has been adjusted with an additive constant to secure an out-of-phase nulling at zero degrees. Experimental data and theoretical predictions are in good agreement.

A.6 Experimental Results

We now consider the three-terminal device, with output power monitored at the transmission port. The effect of varying the gate power as well as phase is recorded.

Figure A.4 contains the detailed parametric data on the operation of the modulator, in symmetric and asymmetric configurations. At gate/source power ratio of 1 in an ideal interferometer, perfect destructive interference would produce nulls with zero power while perfect constructive interference would produce peaks with normalized power of 4. The performance of our symmetric modulator is within the instrumental

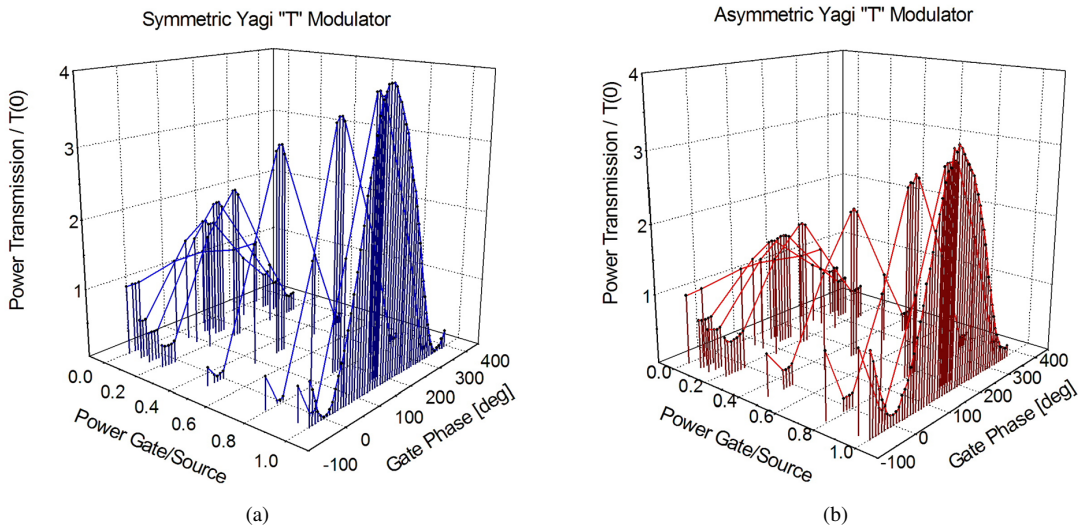

Figure A.4: Transmitted power as a function of gate/source power ratio and of gate phase for the symmetric **(a)** and asymmetric **(b)** configuration of the "T" modulator. An arbitrary phase is added so that the minimum occurs at zero degrees.

error tolerance of this ideal behavior. A typical single measurement yields an on/off ratio of 22 dB, limited by the noise floor at the null or "off" state.

If the interaction between rods were confimed exclusively to first-nearest neighbors, the asymmetric tee would be expected to exhibit nulls and peaks of similar quality to the symmetric case. The experimental result therefore suggests that longer-range interactions play an important role.

A.7 Simulation Results

Full-field electromagnetic calculations were performed on the modulator structure using commercial antenna simulation software [70]. Previously we have found excellent agreement between experimental results and simulations of passive Yagi waveguide structures [79].

Figure A.5 illustrates the field intensity in region surrounding a simulated T modulator. In the on state, the source and modulation signals add constructively at the waveguide intersection, and a relatively large amount of power is transmitted. In the off state, out-of-phase source and modulation signals produce a minimum at the junction and a decrease in transmitted power. Note that only in the symmetric configuration does the off state correspond to a true null in the symmetry plane. As anticipated, energy is strongly confined to the

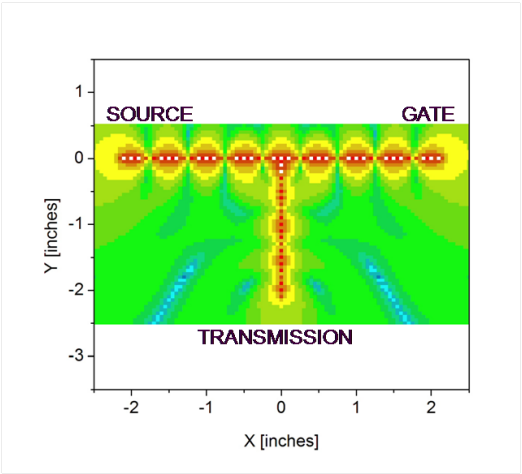

(a) Symmetric: On

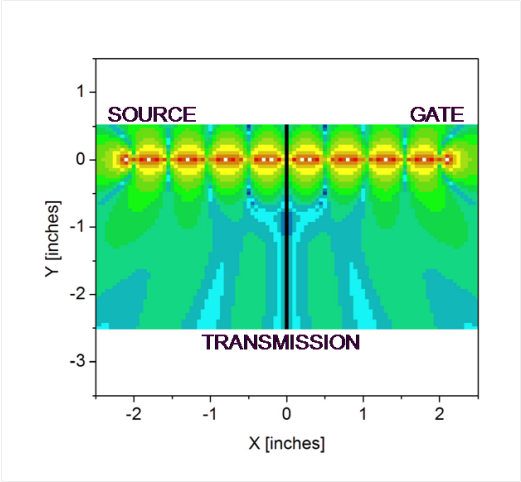

(b) Symmetric: Off

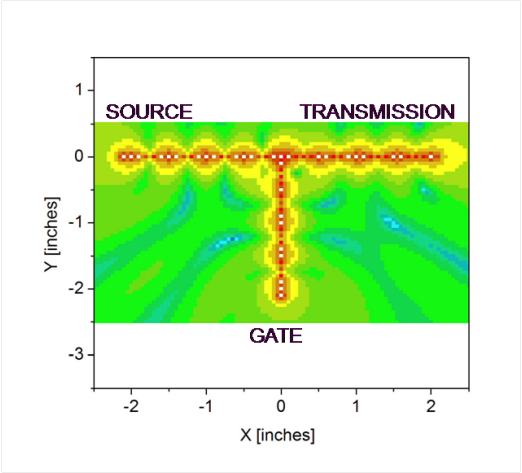

(c) Asymmetric: On

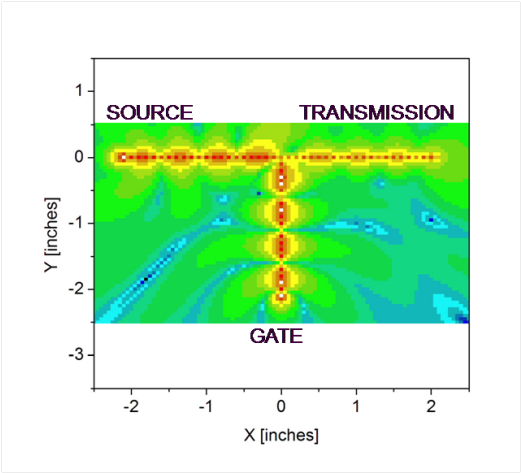

(d) Asymmetric: Off

Figure A.5: Simulated field intensity in the vicinity of a Yagi T modulator for various source and gate configurations.

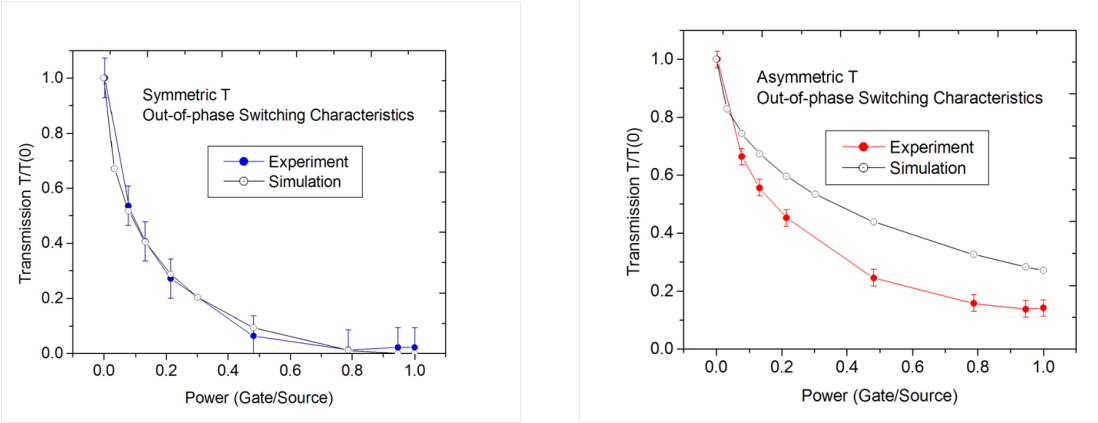

(a) Symmetric

(b) Asymmetric

Figure A.6: Comparison of experimental and simulated transmission of the T interferometer versus gate power, with gate fixed out of phase for optimum modulation depth. Symmetric **(a)** and asymmetric **(b)** configuration.

waveguide, and power is lost to far-field radiation predominantly at the waveguide corners and terminations.

In Figure A.6, we compare quantitatively the transmission characteristics of a simulated modulator to the experimental data presented in the previous section. For the symmetric interferometer, the two results are in excellent agreement. The discrepancy, especially in the asymmetric case, is attributed to imperfect modeling of power which is radiated from source to detector through free space rather than through the waveguide channel.

A.8 Conclusions

A microwave interferometric modulator consisting of subwavelength antenna waveguides was demonstrated. On/off ratios of over 20 dB can he achieved. When operated in the symmetric configuration, the observed characteristics agree quite well with simulated results.

Appendix B

Optical Properties of Materials

The following tabulated data represent the complex dielectric function parameterizations of common dielectrics and plamonic metals which are used most often for numerical work in this thesis.

Table B.1: Optical permittivity of transparent dielectrics

Material	ε_1	Wavelength	Ref.
Air	1.0006	@ 589 nm	
Water	1.77	@ 589 nm	
Ethanol	1.85	@ 589 nm	
Benzene	2.25	@ 589 nm	
Typical biomolecules	1.9 - 2.3		
SiO_2	2.13	@ 589 nm	[75]
Crown Glass (borosilicate)	≈ 2.3		
Flint Glass (leaded)	≈ 2.6		
MGO	3.02	@ 589 nm	[75]
Al_2O_3 (sapphire)	3.13	@ 580 nm	[75]
ITO	3.43	@ 590 nm	[75]
TiO_2	3.61	@ 590 nm	[75]
Si_3N_4	4.08	@ 620 nm	[75]
HfO_2	4.24	@ 580 nm	[75]
Diamond	5.84	@ 589 nm	[75]
$SrTiO_3$	6.03	@ 590 nm	[75]
$LiNbO_3$: o oriented	5.291	@ 588 nm	[75]
$LiNbO_3$: e oriented	4.905	@ 588 nm	[75]
$BaTiO_3$: o oriented	5.905	@ 600 nm	[75]
$BaTiO_3$: e oriented	5.626	@ 600 nm	[75]

B.1 Drude Model Au and Ag

The parameters reported in the following table are for several fits which we perform by non-linear least squares fit to the Palik handbook data for Au and Ag, using the Drude model extended to a four-parameter fit by inclusion of ε_{high} and ε_{static} as fit parameters.

$$\varepsilon_{\text{ExtendedDrude}}(\omega) = \varepsilon_{\text{high}} - \frac{(\varepsilon_{\text{static}} - \varepsilon_{\text{high}})\omega_p^2}{\omega^2 + i\Gamma\omega}.$$

Table B.2: Extended (four-parameter) Drude model permittivity of metals, fit to data from the Palik Handbook [75]. Parameterizations are optimized for use at 1550 nm (infrared) or near 700 nm (visible).

Material	ε_{high}	ε_{static}	ω_p [rad/s]	Γ [rad/s]
Silver, IR Model	6.79	7.14	19.98×10^{15}	0.100×10^{15}
Silver, Vis Model	3.95	60.64	1.77×10^{15}	0.100×10^{15}
Gold, IR Model	9.25	10.74	10.29×10^{15}	0.125×10^{15}
Gold, Vis Model	10.21	47.31	2.33×10^{15}	0.125×10^{15}
Gold, Compromise Model	9.54	10.54	13.5×10^{15}	0.125×10^{15}

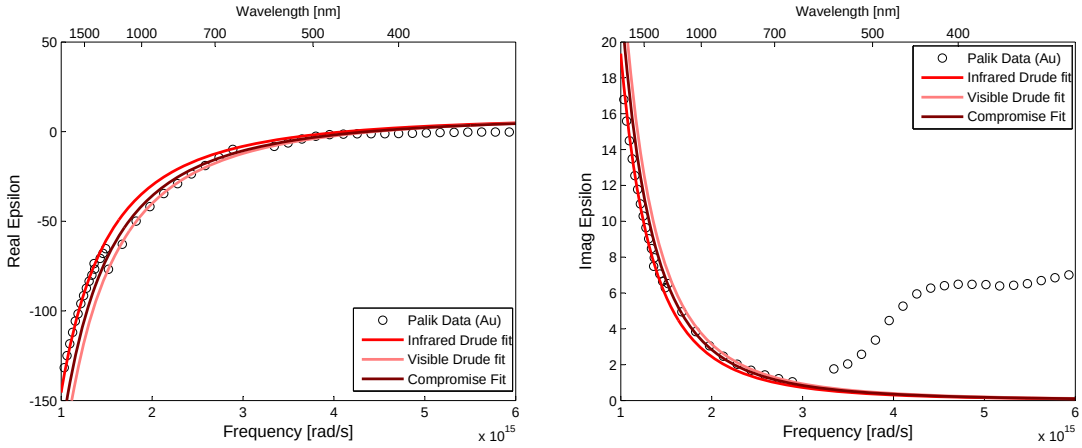

(a) Au Drude $\Re(\varepsilon)$

(b) Au Drude $\Im(\varepsilon)$

Figure B.1: Drude model permittivity of gold (Au); comparison between the Palik Handbook data and the various parameterizations from Table B.2.

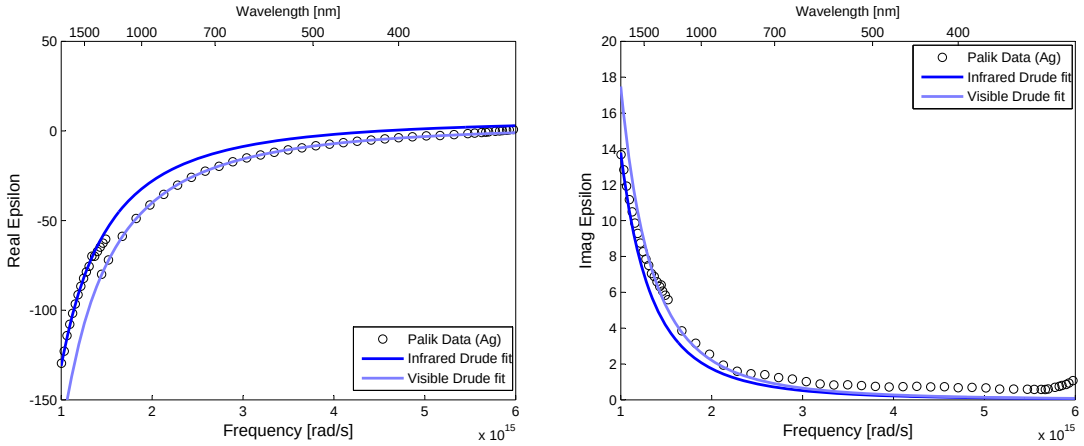

(a) Ag Drude $\Re(\varepsilon)$

(b) Ag Drude $\Im(\varepsilon)$

Figure B.2: Drude model permittivity of silver (Ag); comparison between the Palik Handbook data and the various parameterizations from Table B.2.

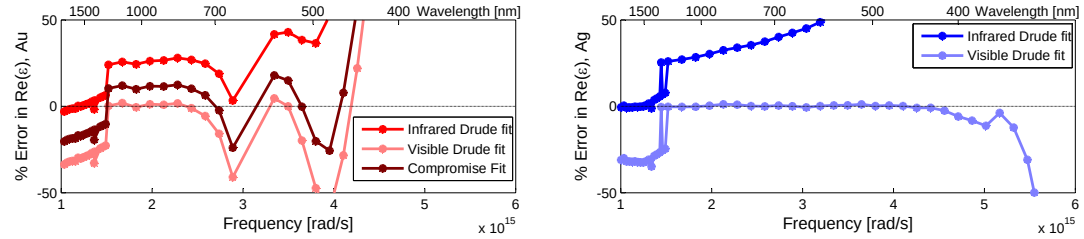

(a) Au Drude % Error in $\Re(\varepsilon)$

(b) Ag Drude % Error in $\Re(\varepsilon)$

Figure B.3: Percent error in the real part of the Drude permittivity of gold (Au) and silver (Ag) relative to the Palik Handbook data, for the various parameterizations from Table B.2.

B.2 Lorentz-Drude Model Metals

The following tables represent data from simulated annealing fits performed by Rakic et al. [115] of the Palik handbook data for metals including Au, Ag, Al, and Cu, which are all free electron metals with potential utility in plasmonics, and Cr which is sometimes used in both simulation and experiment as a specifically plasmon-suppressing media. Compared to the source reference [115], the notation has been translated and the units converted.

$$\varepsilon_{\text{Lorentz-Drude}}(\omega) = 1 - \frac{f_0\omega_{p,0}^2}{\omega^2 + i\Gamma_0\omega} + \sum_{j=1}^{j_{\max}} \frac{f_j\omega_{p,j}^2}{\omega_j^2 - \omega^2 - i\Gamma_j\omega}.$$

Table B.3: Gold (Au) Lorentz-Drude model parameters

Term	f	ω_p [rad/s]	ω_j [rad/s]	Γ_j [rad/s]
j=0	0.760	13.72×10^{15}	0.0000	0.08052×10^{15}
j=1	0.024	13.72×10^{15}	0.6305×10^{15}	0.3661×10^{15}
j=2	0.010	13.72×10^{15}	1.261×10^{15}	0.5241×10^{15}
j=3	0.071	13.72×10^{15}	4.511×10^{15}	1.322×10^{15}
j=4	0.601	13.72×10^{15}	6.538×10^{15}	3.789×10^{15}
j=5	4.384	13.72×10^{15}	20.24×10^{15}	3.364×10^{15}

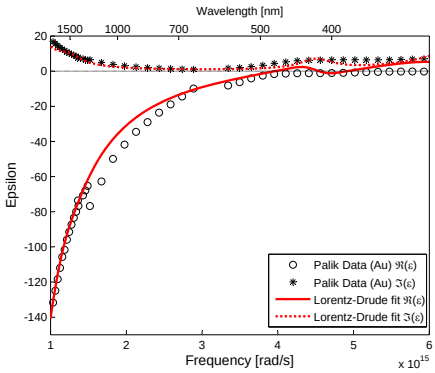

Table B.4: Silver (Ag) Lorentz-Drude model parameters

Term	f	ω_p [rad/s]	ω_j [rad/s]	Γ_j [rad/s]
j=0	0.845	13.69×10^{15}	0.0000	0.07292×10^{15}
j=1	0.065	13.69×10^{15}	1.240×10^{15}	5.904×10^{15}
j=2	0.124	13.69×10^{15}	6.808×10^{15}	0.6867×10^{15}
j=3	0.011	13.69×10^{15}	12.44×10^{15}	0.09875×10^{15}
j=4	0.840	13.69×10^{15}	13.80×10^{15}	1.392×10^{15}
j=5	5.646	13.69×10^{15}	30.83×10^{15}	3.675×10^{15}

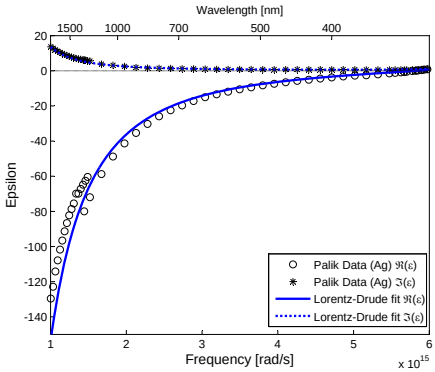

Table B.5: Copper (Cu) Lorentz-Drude model parameters

Term	f	ω_p [rad/s]	ω_j [rad/s]	Γ_j [rad/s]
j=0	0.575	16.45×10^{15}	0.0000	0.04558×10^{15}
j=1	0.061	16.45×10^{15}	0.4421×10^{15}	0.5743×10^{15}
j=2	0.104	16.45×10^{15}	4.492×10^{15}	1.604×10^{15}
j=3	0.723	16.45×10^{15}	8.052×10^{15}	4.881×10^{15}
j=4	0.638	16.45×10^{15}	16.99×10^{15}	6.540×10^{15}

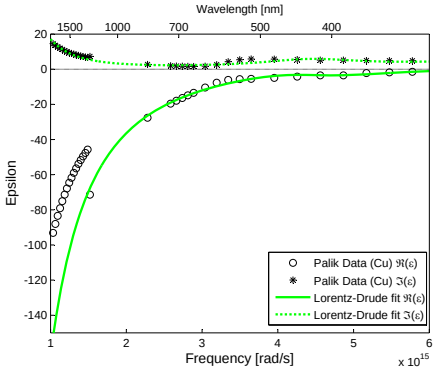

Table B.6: Aluminum (Al) Lorentz-Drude model parameters

Term	f	ω_p [rad/s]	ω_j [rad/s]	Γ_j [rad/s]
j=0	0.523	22.76×10^{15}	0.0000	0.07140×10^{15}
j=1	0.227	22.76×10^{15}	0.2461×10^{15}	0.5059×10^{15}
j=2	0.050	22.76×10^{15}	2.346×10^{15}	0.4740×10^{15}
j=3	0.166	22.76×10^{15}	2.747×10^{15}	2.053×10^{15}
j=4	0.030	22.76×10^{15}	5.276×10^{15}	5.138×10^{15}

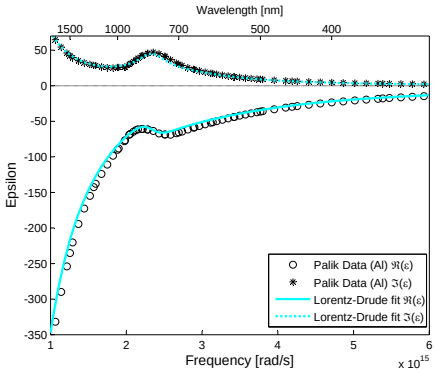

Table B.7: Chromium (Cr) Lorentz-Drude model parameters

Term	f	ω_p [rad/s]	ω_j [rad/s]	Γ_j [rad/s]
j=0	0.168	16.33×10^{15}	0.0000	0.07140×10^{15}
j=1	0.151	16.33×10^{15}	0.1838×10^{15}	4.824×10^{15}
j=2	0.150	16.33×10^{15}	0.8250×10^{15}	1.983×10^{15}
j=3	1.149	16.33×10^{15}	2.993×10^{15}	4.066×10^{15}
j=4	0.825	16.33×10^{15}	13.33×10^{15}	2.028×10^{15}

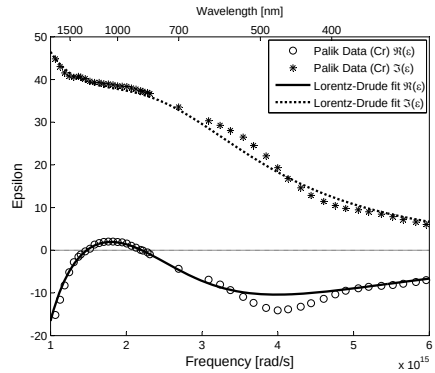

Bibliography

[1] A. L. Aden and M. Kerker. Scattering of electromagnetic waves from 2 concentric spheres. *Journal of Applied Physics*, 22(10):1242–1246, 1951.

[2] V. R. Almeida, Q. F. Xu, C. A. Barrios, and M. Lipson. Guiding and confining light in void nanostructure. *Optics Letters*, 29(11):1209–1211, 2004.

[3] P. Anger, P. Bharadwaj, and L. Novotny. Enhancement and quenching of single-molecule fluorescence. *Physical Review Letters*, 96(11), 2006.

[4] T. Atay, J. H. Song, and A. V. Nurmikko. Strongly interacting plasmon nanoparticle pairs: From dipole-dipole interaction to conductively coupled regime. *Nano Letters*, 4(9):1627–1631, 2004.

[5] S. Baher and M. G. Cottam. Theory of nonlinear guided and surface plasmon-polaritons in dielectric films. *Surface Review and Letters*, 10(1):13–22, 2003.

[6] W. L. Barnes, A. Dereux, and T. W. Ebbesen. Surface plasmon subwavelength optics. *Nature*, 424(6950):824–830, 2003.

[7] M. V. Bashevoy, F. Jonsson, A. V. Krasavin, N. I. Zheludev, Y. Chen, and M. I. Stockman. Generation of traveling surface plasmon waves by free-electron impact. *Nano Letters*, 6(6):1113–1115, 2006.

[8] D. J. Bergman and M. I. Stockman. Surface plasmon amplification by stimulated emission of radiation: Quantum generation of coherent surface plasmons in nanosystems. *Physical Review Letters*, 90(2), 2003.

[9] P. Berini. Plasmon-polariton waves guided by thin lossy metal films of finite width: Bound modes of symmetric structures. *Physical Review B*, 61(15):10484–10503, 2000.

[10] P. Berini. Plasmon-polariton waves guided by thin lossy metal films of finite width: Bound modes of asymmetric structures. *Physical Review B*, 63(12):125417, 2001.

[11] J. S. Biteen, N. S. Lewis, H. A. Atwater, H. Mertens, and A. Polman. Spectral tuning of plasmon-enhanced silicon quantum dot luminescence. *Applied Physics Letters*, 88(13), 2006.

[12] J. S. Biteen, D. Pacifici, N. S. Lewis, and H. A. Atwater. Enhanced radiative emission rate and quantum efficiency in coupled silicon nanocrystal-nanostructured gold emitters. *Nano Letters*, 5(9):1768–1773, 2005.

[13] J. S. Biteen, L. A. Sweatlock, H. Mertens, N. S. Lewis, A. Polman, and H. A. Atwater. Plasmon-enhanced photoluminescence of silicon quantum dots: Simulation and experiment. *Journal of Physical Chemistry C*, 111(36):13372–13377, 2007.

[14] Craig F. Bohren and Donald R. Huffman. *Absorption and Scattering of Light by Small Particles*. Wiley, New York, 1983.

[15] M. Bosman, V. J. Keast, M. Watanabe, A. I. Maaroof, and M. B. Cortie. Mapping surface plasmons at the nanometre scale with an electron beam. *Nanotechnology*, 18(16), 2007.

[16] S. I. Bozhevolnyi and V. Z. Lozovski. Second-harmonic scanning optical microscopy of individual nanostructures. *Physical Review B*, 65(23), 2002.

[17] S. I. Bozhevolnyi, V. S. Volkov, E. Devaux, J. Y. Laluet, and T. W. Ebbesen. Channel plasmon subwavelength waveguide components including interferometers and ring resonators. *Nature*, 440(7083):508–511, 2006.

[18] M. L. Brongersma, J. W. Hartman, and H. A. Atwater. Electromagnetic energy transfer and switching in nanoparticle chain arrays below the diffraction limit. *Physical Review B*, 62(24):16356–16359, 2000.

[19] M. L. Brongersma and P. G. Kik, editors. *Surface Plasmon Nanophotonics*. Springer, Dordrecht, NL, 2007.

[20] M. L. Brongersma, A. Polman, K. S. Min, E. Boer, T. Tambo, and H. A. Atwater. Tuning the emission wavelength of si nanocrystals in sio2 by oxidation. *Applied Physics Letters*, 72(20):2577–2579, 1998.

[21] M. L. Brongersma, E. Snoeks, T. van Dillen, and A. Polman. Origin of mev ion irradiation-induced stress changes in sio2. *Journal of Applied Physics*, 88(1):59–64, 2000.

[22] J. J. Burke, G. I. Stegeman, and T. Tamir. Surface-polariton-like waves guided by thin, lossy metal-films. *Physical Review B*, 33(8):5186–5201, 1986.

[23] F. Caccavale, G. Demarchi, F. Gonella, P. Mazzoldi, C. Meneghini, A. Quaranta, G. W. Arnold, G. Battaglin, and G. Mattei. Irradiation-induced ag-colloid formation in ion-exchanged soda-lime glass. *Nuclear Instruments & Methods in Physics Research Section B-Beam Interactions with Materials and Atoms*, 96(1-2):382–386, 1995.

[24] C. K. Chang, D. Z. Lin, C. S. Yeh, C. K. Lee, Y. C. Chang, M. W. Lin, J. T. Yeh, and J. M. Liu. Experimental analysis of surface plasmon behavior in metallic circular slits. *Applied Physics Letters*, 90(6), 2007.

[25] R. Charbonneau, P. Berini, E. Berolo, and E. Lisicka-Shrzek. Experimental observation of plasmon-polariton waves supported by a thin metal film of finite width. *Optics Letters*, 25(11):844–846, 2000.

[26] A. E. Craig, G. A. Olson, and D. Sarid. Experimental-observation of the long-range surface-plasmon polariton. *Optics Letters*, 8(7):380–382, 1983.

[27] F. J. G. de Abajo and A. Howie. Relativistic electron energy loss and electron-induced photon emission in lymphogenous dielectrics. *Physical Review Letters*, 80(23):5180–5183, 1998.

[28] F. J. G. de Abajo and A. Howie. Retarded field calculation of electron energy loss in inhomogeneous dielectrics. *Physical Review B*, 65(11), 2002.

[29] J. A. Dionne, K. A. Diest, L.A. Sweatlock, and H. A. Atwater. Plasmostor: a metal-oxide-silicon field effect plasmonic modulator. 2008. (Submitted).

[30] J. A. Dionne, H. J. Lezec, and H. A. Atwater. Highly confined photon transport in subwavelength metallic slot waveguides. *Nano Letters*, 6(9):1928–1932, 2006.

[31] J. A. Dionne, L. A. Sweatlock, H. A. Atwater, and A. Polman. Planar metal plasmon waveguides: frequency-dependent dispersion, propagation, localization, and loss beyond the free electron model. *Physical Review B*, 72(7), 2005.

[32] J. A. Dionne, L. A. Sweatlock, H. A. Atwater, and A. Polman. Plasmon slot waveguides: Towards chip-scale propagation with subwavelength-scale localization. *Physical Review B*, 73(3), 2006.

[33] R.W. Ditchburn. *Light*. Dover, New York, 1961.

[34] D. Drouin. Monte carlo simulation of electron trajectory in solids (Casino), 2001. Software Package.

[35] P. Drude. Optical properties and the electron theory. *Annalen Der Physik*, 14(10):936–961, 1904.

[36] E. N. Economou. Surface plasmons in thin films. *Physical Review*, 182(2):539, 1969.

[37] T. Fischer, V. PetrovaKoch, K. Shcheglov, M. S. Brandt, and F. Koch. Continuously tunable photoluminescence from si+-implanted and thermally annealed sio2 films. *Thin Solid Films*, 276(1-2):100–103, 1996.

[38] M Fleischmann, P.J. Hendra, and A.J. McQuillan. Raman spectra of pyridine adsorbed at a silver electrode. *Chemical Physics Letters*, 26, 1974.

[39] G. Fuster, J. M. Tyler, N. E. Brener, J. Callaway, and D. Bagayoko. Electronic-structure and related properties of silver. *Physical Review B*, 42(12):7322–7329, 1990.

[40] S.A. Galloway, P. Miller, P. Thomas, and R. Harmon. *Phys. Status Solidi C*, pages 1028–1032, 2003.

[41] F. J. Garcia-Vidal and J. B. Pendry. Collective theory for surface enhanced raman scattering. *Physical Review Letters*, 77(6):1163–1166, 1996.

[42] R. J. Gehr and R. W. Boyd. Optical properties of nanostructured optical materials. *Chemistry of Materials*, 8(8):1807–1819, 1996.

[43] D. A. Genov, A. K. Sarychev, V. M. Shalaev, and A. Wei. Resonant field enhancements from metal nanoparticle arrays. *Nano Letters*, 4(1):153–158, 2004.

[44] J. M. Gerardy and M. Ausloos. Absorption-spectrum of clusters of spheres from the general-solution of maxwell equations .2. optical-properties of aggregated metal spheres. *Physical Review B*, 25(6):4204–4229, 1982.

[45] J. M. Gerardy and M. Ausloos. Statistically correlated polarization-fields and optical-properties of a composite medium. *Physical Review B*, 26(8):4703–4706, 1982.

[46] J. Gersten and A. Nitzan. Electromagnetic theory of enhanced raman-scattering by molecules adsorbed on rough surfaces. *Journal of Chemical Physics*, 73(7):3023–3037, 1980.

[47] J. Gersten and A. Nitzan. Spectroscopic properties of molecules interacting with small dielectric particles. *Journal of Chemical Physics*, 75(3):1139–1152, 1981.

[48] Gesellschaft für Computer-Simulationstechnik (CST). Maxwell's equations by finite integration algorithm (Mafia), 2000. Software Package.

[49] F. Hache, D. Ricard, and C. Flytzanis. Optical nonlinearities of small metal particles — surface-mediated resonance and quantum size effects. *Journal of the Optical Society of America B — Optical Physics*, 3(12):1647–1655, 1986.

[50] A. J. Haes and R. P. Van Duyne. A unified view of propagating and localized surface plasmon resonance biosensors. *Analytical and Bioanalytical Chemistry*, 379(7–8):920–930, 2004.

[51] Y. Hamanaka, K. Fukuta, A. Nakamura, L. M. Liz-Marzan, and P. Mulvaney. Enhancement of third-order nonlinear optical susceptibilities in silica-capped au nanoparticle films with very high concentrations. *Applied Physics Letters*, 84(24):4938–4940, 2004.

[52] C. L. Haynes, A. D. McFarland, L. L. Zhao, R. P. Van Duyne, G. C. Schatz, L. Gunnarsson, J. Prikulis, B. Kasemo, and M. Kall. Nanoparticle optics: The importance of radiative dipole coupling in two-dimensional nanoparticle arrays. *Journal of Physical Chemistry B*, 107(30):7337–7342, 2003.

[53] S. C. Hill, G. Videen, and J. D. Pendleton. Reciprocity method for obtaining the far fields generated by a source inside or near a microparticle. *Journal of the Optical Society of America B — Optical Physics*, 14(10):2522–2529, 1997.

[54] L. R. Hirsch, J. B. Jackson, A. Lee, N. J. Halas, and J. West. A whole blood immunoassay using gold nanoshells. *Analytical Chemistry*, 75(10):2377–2381, 2003.

[55] C. E. Hofmann, E. J. R. Vesseur, L. A. Sweatlock, H. J. Lezec, F. J. Garcia de Abajo, A. Polman, and H. A. Atwater. Plasmonic modes of annular nanoresonators imaged by spectrally resolved cathodoluminescence. *Nano Letters*, 7(12):3612–3617, 2007.

[56] J. Homola, S. S. Yee, and G. Gauglitz. Surface plasmon resonance sensors: review. *Sensors and Actuators B — Chemical*, 54(1–2):3–15, 1999.

[57] Jackson.

[58] P. B. Johnson and R. W. Christy. Optical-constants of noble-metals. *Physical Review B*, 6(12):4370–4379, 1972.

[59] M. Kaempfe, H. Graener, A. Kiesow, and A. Heilmann. Formation of metal particle nanowires induced by ultrashort laser pulses. *Applied Physics Letters*, 79(12):1876–1878, 2001.

[60] K. L. Kelly, E. Coronado, L. L. Zhao, and G. C. Schatz. The optical properties of metal nanoparticles: The influence of size, shape, and dielectric environment. *Journal of Physical Chemistry B*, 107(3):668–677, 2003.

[61] B. Khlebtsov, A. Melnikov, V. Zharov, and N. Khlebtsov. Absorption and scattering of light by a dimer of metal nanospheres: comparison of dipole and multipole approaches. *Nanotechnology*, 17(5):1437–1445, 2006.

[62] J. P. Kottmann and O. J. F. Martin. Plasmon resonant coupling in metallic nanowires. *Optics Express*, 8(12):655–663, 2001.

[63] U. Kreibig and M. Vollmer. *Optical Properties of Metal Clusters*. Springer-Verlag, Berlin, 1994.

[64] J. R. Krenn, A. Dereux, J. C. Weeber, E. Bourillot, Y. Lacroute, J. P. Goudonnet, G. Schider, W. Gotschy, A. Leitner, F. R. Aussenegg, and C. Girard. Squeezing the optical near-field zone by plasmon coupling of metallic nanoparticles. *Physical Review Letters*, 82(12):2590–2593, 1999.

[65] J. R. Krenn, B. Lamprecht, H. Ditlbacher, G. Schider, M. Salerno, A. Leitner, and F. R. Aussenegg. Non diffraction-limited light transport by gold nanowires. *Europhysics Letters*, 60(5):663–669, 2002.

[66] E. Kretschmann and H. Raether. Radiative decay of non-radiative surface plasmons excited by light. *Zeitschrift fur Naturforschung*, 23A, 1968.

[67] S. Kuhn, U. Hakanson, L. Rogobete, and V. Sandoghdar. Enhancement of single-molecule fluorescence using a gold nanoparticle as an optical nanoantenna. *Physical Review Letters*, 97(1), 2006.

[68] O. Kulakovich, N. Strekal, A. Yaroshevich, S. Maskevich, S. Gaponenko, I. Nabiev, U. Woggon, and M. Artemyev. Enhanced luminescence of cdse quantum dots on gold colloids. *Nano Letters*, 2(12):1449–1452, 2002.

[69] J. Kummerlen, A. Leitner, H. Brunner, F. R. Aussenegg, and A. Wokaun. Enhanced dye fluorescence over silver island films — analysis of the distance dependence. *Molecular Physics*, 80(5):1031–1046, 1993.

[70] R.W. Lewallen. Eznec v2.0, 1999.

[71] H. J. Lezec, A. Degiron, E. Devaux, R. A. Linke, L. Martin-Moreno, F. J. Garcia-Vidal, and T. W. Ebbesen. Beaming light from a subwavelength aperture. *Science*, 297(5582):820–822, 2002.

[72] H. J. Lezec, J. A. Dionne, and H. A. Atwater. Negative refraction at visible frequencies. *Science*, 316(5823):430–432, 2007.

[73] Z. W. Liu, J. M. Steele, W. Srituravanich, Y. Pikus, C. Sun, and X. Zhang. Focusing surface plasmons with a plasmonic lens. *Nano Letters*, 5(9):1726–1729, 2005.

[74] F. Lopez-Tejeira, S. G. Rodrigo, L. Martin-Moreno, F. J. Garcia-Vidal, E. Devaux, T. W. Ebbesen, J. R. Krenn, I. P. Radko, S. I. Bozhevolnyi, M. U. Gonzalez, J. C. Weeber, and A. Dereux. Efficient unidirectional nanoslit couplers for surface plasmons. *Nature Physics*, 3(5):324–328, 2007.

[75] D. W. Lynch and W. R. Hunter. Comments on the optical constants of metals and an introduction to the data for several metals. In E. D. Palik, editor, *Handbook of Optical Constants of Solids*, pages 275–367. Academic, Orlando, FL, 1985.

[76] S. A. Maier. *Guiding of electromagnetic energy in subwavelength periodic metal structures*. PhD thesis, Caltech, 2003.

[77] S. A. Maier. Plasmonics — towards subwavelength optical devices. *Current Nanoscience*, 1(1):17–23, 2005.

[78] S. A. Maier. Plasmonic field enhancement and sers in the effective mode volume picture. *Optics Express*, 14(5):1957–1964, 2006.

[79] S. A. Maier, M. L. Brongersma, and H. A. Atwater. Electromagnetic energy transport along arrays of closely spaced metal rods as an analogue to plasmonic devices. *Applied Physics Letters*, 78(1):16–18, 2001.

[80] S. A. Maier, P. G. Kik, and H. A. Atwater. Observation of coupled plasmon-polariton modes in au nanoparticle chain waveguides of different lengths: Estimation of waveguide loss. *Applied Physics Letters*, 81(9):1714–1716, 2002.

[81] S. A. Maier, P. G. Kik, and H. A. Atwater. Optical pulse propagation in metal nanoparticle chain waveguides. *Physical Review B*, 67(20), 2003.

[82] S. A. Maier, P. G. Kik, H. A. Atwater, S. Meltzer, E. Harel, B. E. Koel, and A. A. G. Requicha. Local detection of electromagnetic energy transport below the diffraction limit in metal nanoparticle plasmon waveguides. *Nature Materials*, 2(4):229–232, 2003.

[83] J. C. Maxwell Garnett. Colours in metal glasses and in metallic films. *Philosophical Transactions of the Royal Society of London*, 203, 1904.

[84] A. D. McFarland and R. P. Van Duyne. Single silver nanoparticles as real-time optical sensors with zeptomole sensitivity. *Nano Letters*, 3(8):1057–1062, 2003.

[85] R. A. McMillan, C. D. Paavola, J. Howard, S. L. Chan, N. J. Zaluzec, and J. D. Trent. Ordered nanoparticle arrays formed on engineered chaperonin protein templates. *Nature Materials*, 1(4):247–252, 2002.

[86] H. Mertens, J. S. Biteen, H. A. Atwater, and A. Polman. Polarization-selective plasmon-enhanced silicon quantum-dot luminescence. *Nano Letters*, 6(11):2622–2625, 2006.

[87] H. Mertens, A. F. Koenderink, and A. Polman. Plasmon-enhanced luminescence near noble-metal nanospheres: Comparison of exact theory and an improved gersten and nitzan model. *Physical Review B*, 76(11), 2007.

[88] H. Mertens and A. Polman. Depth-resolved nanostructure and refractive index of borosilicate glass doped with ag nanocrystals. *Optical Materials*, 29(2–3):326–331, 2006.

[89] G. Mie. Beiträge zur optik trüber medien, speziell kolloidaler metallösungen. *Annalen Der Physik*, 25(3):377–445, 1908.

[90] K. S. Min, K. V. Shcheglov, C. M. Yang, H. A. Atwater, M. L. Brongersma, and A. Polman. Defect-related versus excitonic visible light emission from ion beam synthesized si nanocrystals in sio2. *Applied Physics Letters*, 69(14):2033–2035, 1996.

[91] A. E. Neeves and M. H. Birnboim. Composite structures for the enhancement of nonlinear-optical susceptibility. *Journal of the Optical Society of America B — Optical Physics*, 6(4):787–796, 1989.

[92] J. Nelayah, M. Kociak, O. Stephan, F. J. G. de Abajo, M. Tence, L. Henrard, D. Taverna, I. Pastoriza-Santos, L. M. Liz-Marzan, and C. Colliex. Mapping surface plasmons on a single metallic nanoparticle. *Nature Physics*, 3(5):348–353, 2007.

[93] S. M. Nie and S. R. Emery. Probing single molecules and single nanoparticles by surface-enhanced raman scattering. *Science*, 275(5303):1102–1106, 1997.

[94] T. Nikolajsen, K. Leosson, I. Salakhutdinov, and S. I. Bozhevolnyi. Polymer-based surface-plasmon-polariton stripe waveguides at telecommunication wavelengths. *Applied Physics Letters*, 82(5):668–670, 2003.

[95] P. Nordlander, C. Oubre, E. Prodan, K. Li, and M. I. Stockman. Plasmon hybridizaton in nanoparticle dimers. *Nano Letters*, 4(5):899–903, 2004.

[96] S. J. Oldenburg, R. D. Averitt, S. L. Westcott, and N. J. Halas. Nanoengineering of optical resonances. *Chemical Physics Letters*, 288(2–4):243–247, 1998.

[97] A. Otto. Excitation of nonradiative surface plasma waves in silver by the method of frustrated total reflection. *Zeitschrift fur Physik*, 1968.

[98] A. Otto, I. Mrozek, H. Grabhorn, and W. Akemann. Surface-enhanced raman-scattering. *Journal of Physics — Condensed Matter*, 4(5):1143–1212, 1992.

[99] E. Ozbay. Plasmonics: Merging photonics and electronics at nanoscale dimensions. *Science*, 311(5758):189–193, 2006.

[100] D. Pacifici, H. J. Lezec, and H. A. Atwater. All-optical modulation by plasmonic excitation of cdse quantum dots. *Nature Photonics*, 1(7):402–406, 2007.

[101] D. Pacifici, H. J. Lezec, L. A. Sweatlock, C. de Ruiter, V. Ferry, and H. A. Atwater. All-optical plasmonic modulators and interconnects. In S. I. Bozhevolnyi, editor, *Plasmonic Nanoguides and Circuits*. In press.

[102] S. Y. Park and D. Stroud. Surface-plasmon dispersion relations in chains of metallic nanoparticles: An exact quasistatic calculation. *Physical Review B*, 69(12), 2004.

[103] J. Penninkhof, C. Graf, T. van Dillen, A. M. Vredenberg, A. van Blaaderen, and A. Polman. Angle-dependent extinction of anisotropic silica/au core/shell colloids made via ion irradiation. *Advanced Materials*, 17(12):1484–1488, 2005.

[104] J. J. Penninkhof, A. Moroz, A. van Blaaderen, and A. Polman. Optical properties of spherical and oblate spheroidal gold shell colloids. *Journal of Physical Chemistry C*, 112(11):4146–4150, 2008.

[105] J. J. Penninkhof, A. Polman, L. A. Sweatlock, S. A. Maier, H. A. Atwater, A. M. Vredenberg, and B. J. Kooi. Mega-electron-volt ion beam induced anisotropic plasmon resonance of silver nanocrystals in glass. *Applied Physics Letters*, 83(20):4137–4139, 2003.

[106] J. J. Penninkhof, T. van Dillen, S. Roorda, C. Graf, A. van Blaaderen, A. M. Vredenberg, and A. Polman. Anisotropic deformation of metallo-dielectric core-shell colloids under mev ion irradiation. *Nuclear Instruments & Methods in Physics Research Section B-Beam Interactions with Materials and Atoms*, 242(1-2):523–529, 2006.

[107] J.J. Penninkhof, A. Polman, L.A. Sweatlock, H. A. Atwater, A. Moroz, and A. van Blaaderen. Optical cavity modes in gold shell colloids. *Journal of Applied Physics*, (In press).

[108] D. P. Peters, C. Strohhofer, M. L. Brongersma, J. van der Elsken, and A. Polman. Formation mechanism of silver nanocrystals made by ion irradiation of Na+ to Ag+ ion-exchanged sodalime silicate glass. *Nuclear Instruments & Methods in Physics Research Section B — Beam Interactions with Materials and Atoms*, 168(2):237–244, 2000.

[109] E. Prodan, C. Radloff, N. J. Halas, and P. Nordlander. A hybridization model for the plasmon response of complex nanostructures. *Science*, 302(5644):419–422, 2003.

[110] D. Prot, D. B. Stout, J. Lafait, N. Pincon, B. Palpant, and S. Debrus. Local electric field enhancements and large third-order optical nonlinearity in nanocomposite materials. *Journal of Optics A — Pure and Applied Optics*, 4(5):S99–S102, 2002.

[111] E. M. Purcell, H. C. Torrey, and R. V. Pound. Resonance absorption by nuclear magnetic moments in a solid. *Physical Review*, 69(1–2):37–38, 1946.

[112] M. Quinten and U. Kreibig. Absorption and elastic-scattering of light by particle aggregates. *Applied Optics*, 32(30):6173–6182, 1993.

[113] M. Quinten, A. Leitner, J. R. Krenn, and F. R. Aussenegg. Electromagnetic energy transport via linear chains of silver nanoparticles. *Optics Letters*, 23(17):1331–1333, 1998.

[114] H. Raether. *Surface Plasmons on Smooth and Rough Surfaces and on Gratings*. Springer-Verlag, Berlin, 1988.

[115] A. D. Rakic, A. B. Djurisic, J. M. Elazar, and M. L. Majewski. Optical properties of metallic films for vertical-cavity optoelectronic devices. *Applied Optics*, 37(22):5271–5283, 1998.

[116] L. Rayleigh. *Phil. Mag.*, 47, 1899.

[117] R. H. Ritchie. Plasma losses by fast electrons in thin films. *Physical Review*, 106, 1957.

[118] S. Roorda, T. van Dillen, A. Polman, C. Graf, A. van Blaaderen, and B. J. Kooi. Aligned gold nanorods in silica made by ion irradiation of core-shell colloidal particles. *Advanced Materials*, 16(3):235, 2004.

[119] R. Ruppin. Decay of an excited molecule near a small metal sphere. *Journal of Chemical Physics*, 76(4):1681–1684, 1982.

[120] B. E. Saleh and M. C. Teich. *Fundimentals of Photonics*. Wiley, New York, 1991.

[121] D. Sarid. Long-range surface-plasma waves on very thin metal-films. *Physical Review Letters*, 47(26):1927–1930, 1981.

[122] D. L. Sengupta. On the phase velocity of wave propagation along an infinite yagi structure. *Inst. of Radio Engineers Trans. Antennas Propag.*, AP-7:234, 1959.

[123] F. Serracchioli and C.A. Levis. The calculated phase velocity of long end-fire uniform dipole arrays. *Inst. of Radio Engineers Trans. Antennas Propag.*, AP-7:424, 1959.

[124] Y. Shen and P. N. Prasad. Nanophotonics: a new multidisciplinary frontier. *Applied Physics B — Lasers and Optics*, 74(7–8):641–645, 2002.

[125] K. T. Shimizu, W. K. Woo, B. R. Fisher, H. J. Eisler, and M. G. Bawendi. Surface-enhanced emission from single semiconductor nanocrystals. *Physical Review Letters*, 89(11), 2002.

[126] E. Snoeks, A. van Blaaderen, T. van Dillen, C. M. van Kats, M. L. Brongersma, and A. Polman. Colloidal ellipsoids with continuously variable shape. *Advanced Materials*, 12(20):1511–1514, 2000.

[127] J. O. Spector. An investigation of periodic rod structures for yagi aerials. *J. Inst. of Electrical Engineers*, 105:38, 1958.

[128] J. M. Steele, Z. W. Liu, Y. Wang, and X. Zhang. Resonant and non-resonant generation and focusing of surface plasmons with circular gratings. *Optics Express*, 14(12):5664–5670, 2006.

[129] G. I. Stegeman, J. J. Burke, and D. G. Hall. Non-linear optics of long-range surface-plasmons. *Applied Physics Letters*, 41(10):906–908, 1982.

[130] L. A. Sweatlock, S. A. Maier, and H. A. Atwater. Microwave analogue to a subwavelength plasmon switch. In *Electronic Components and Technology Conference*, page 1648. IEEE, 2003.

[131] L. A. Sweatlock, S. A. Maier, H. A. Atwater, J. J. Penninkhof, and A. Polman. Highly confined electromagnetic fields in arrays of strongly coupled ag nanoparticles. *Physical Review B*, 71(23), 2005.

[132] A. Taflove and S. C. Hagness. *Computational Electrodynamics: the finite-difference time domain method*. Artech House, Norwood MA, 2000.

[133] E. A. Taft and H. R. Philipp. Optical constants of silver. *Physical Review*, 121(4):1100, 1961.

[134] M. Tanaka. Description of a wave packet propagating in anomalous dispersion media — a new expression of propagation velocity. *Plasma Phys. Controlled Fusion*, 31(7):1049, 1989.

[135] H. Tuovinen, M. Kauranen, K. Jefimovs, P. Vahimaa, T. Vallius, J. Turunen, N. V. Tkachenko, and H. Lemmetyinen. Linear and second-order nonlinear optical properties of arrays of noncentrosymmetric gold nanoparticles. *Journal of Nonlinear Optical Physics & Materials*, 11(4):421–432, 2002.

[136] J. T. van Wijngaarden, E. Verhagen, A. Polman, C. E. Ross, H. J. Lezec, and H. A. Atwater. Direct imaging of propagation and damping of near-resonance surface plasmon polaritons using cathodoluminescence spectroscopy. *Applied Physics Letters*, 88(22), 2006.

[137] G. Veronis and S. H. Fan. Theoretical investigation of compact couplers between dielectric slab waveguides and two-dimensional metal-dielectric-metal plasmonic waveguides. *Optics Express*, 15(3):1211–1221, 2007.

[138] E. J. R. Vesseur, R. de Waele, M. Kuttge, and A. Polman. Direct observation of plasmonic modes in au nanowires using high-resolution cathodoluminescence spectroscopy. *Nano Letters*, 7(9):2843–2846, 2007.

[139] H. Wang, D. W. Brandl, F. Le, P. Nordlander, and N. J. Halas. Nanorice: A hybrid plasmonic nanostructure. *Nano Letters*, 6(4):827–832, 2006.

[140] Q. H. Wei, K. H. Su, S. Durant, and X. Zhang. Plasmon resonance of finite one-dimensional au nanoparticle chains. *Nano Letters*, 4(6):1067–1071, 2004.

[141] A. Wokaun, J. P. Gordon, and P. F. Liao. Radiation damping in surface-enhanced raman-scattering. *Physical Review Letters*, 48(14):957–960, 1982.

[142] A. Wokaun, H. P. Lutz, A. P. King, U. P. Wild, and R. R. Ernst. Energy-transfer in surface enhanced luminescence. *Journal of Chemical Physics*, 79(1):509–514, 1983.

[143] H. X. Xu, J. Aizpurua, M. Kall, and P. Apell. Electromagnetic contributions to single-molecule sensitivity in surface-enhanced raman scattering. *Physical Review E*, 62(3):4318–4324, 2000.

[144] N. Yamamoto, K. Araya, and F. J. G. de Abajo. Photon emission from silver particles induced by a high-energy electron beam. *Physical review B — Condensed matter and materials physics*, 64:205419, 2001.

[145] N. Yamamoto, M. Nakano, and T. Suzuki. Light emission by surface plasmons on nanostructures of metal surfaces induced by high-energy electron beams. *Surface and Interface Analysis*, 38:1725–1730, 2006.

[146] L. L. Zhao, K. L. Kelly, and G. C. Schatz. The extinction spectra of silver nanoparticle arrays: Influence of array structure on plasmon resonance wavelength and width. *Journal of Physical Chemistry B*, 107(30):7343–7350, 2003.

[147] R. Zia, M. D. Selker, P. B. Catrysse, and M. L. Brongersma. Geometries and materials for subwavelength surface plasmon modes. *Journal of the Optical Society of America A*, 21(12):2442–2446, 2004.

[148] J. F. Ziegler, J. P. Biersack, and U. Littmark. *The Stopping and Range of Ions in Solids*. Pergamon, New York, 1985.

[149] S. L. Zou and G. C. Schatz. Silver nanoparticle array structures that produce giant enhancements in electromagnetic fields. *Chemical Physics Letters*, 403(1–3):62–67, 2005.